NASA CONTRACTOR REPORT

NASA CR-735

EXPERIMENTAL INVESTIGATION OF ADVANCED CONCEPTS TO INCREASE TURBINE BLADE LOADING

I. ANALYSIS AND DESIGN

by H. G. Lueders

Prepared by
ALLISON DIVISION, GENERAL MOTORS
Indianapolis, Ind.
for Lewis Research Center

NATIONAL AERONAUTICS AND SPACE ADMINISTRATION • WASHINGTON, D. C. • JUNE 1967

NASA CR-735

EXPERIMENTAL INVESTIGATION OF ADVANCED CONCEPTS TO INCREASE TURBINE BLADE LOADING

I. ANALYSIS AND DESIGN

By H. G. Lueders

Prepared under Contract No. NAS 3-7902 by
ALLISON DIVISION, GENERAL MOTORS
Indianapolis, Ind.

for Lewis Research Center

NATIONAL AERONAUTICS AND SPACE ADMINISTRATION

For sale by the Clearinghouse for Federal Scientific and Technical Information
Springfield, Virginia 22151 – CFSTI price $3.00

FOREWORD

The research described herein, which was conducted by the Allison Division, General Motors, was performed under NASA Contract NAS 3-7902. The work was done under the technical management of Mr. Edward L. Warren Airbreathing Engines Division, NASA-Lewis Research Center, with Mr. Richard J. Roelke, Fluid Systems Component Division, NASA-Lewis Research Center, as research consultant. The report was originally issued as Allison, General Motors Report ERD 4909, October 1966.

ABSTRACT

A program was initiated to experimentally investigate advanced concepts to increase turbine rotor-blade loading. Four different concepts were investigated: vortex generators, tangential slot blowing, tandem airfoil, and jet-flap. The analysis and design of the required hardware was made, including a stator-blade to be used with each of the four rotor-blades. The rotor-blades were designed to a suction-surface diffusion factor of 0.3.

TABLE OF CONTENTS

EXPERIMENTAL INVESTIGATION OF ADVANCED CONCEPTS TO INCREASE TURBINE BLADE LOADING

I. ANALYSIS AND DESIGN

by H. G. Lueders

Allison Division, General Motors

SUMMARY

This report presents the design and analysis of a single-stage cold air test rig turbine to investigate advanced concepts to increase turbine blade loading without significant loss in performance. The design and analysis of a plain rotor blade with high suction surface loading are presented. This rotor blade forms the program base line from which concepts are investigated to permit highly loaded aerodynamic designs without the predicted flow separation and high loss of the plain airfoil. The advanced concepts of this program include the use of vortex generators, tangential slot blowing, tandem airfoil, and jet flap. The aerodynamic design and analysis of all concepts are included in this report. The associated mechanical design, stress analysis, and instrumentation of the test rig are also presented.

INTRODUCTION

The analysis and optimization of propulsion systems have always involved a balance or trade between (1) turbine efficiency and (2) turbine size and weight reduction. Generally, the reduction of turbine diameter, solidity, and/or stage reaction results in a smaller and/or lighter turbine but at some sacrifice in efficiency due to losses associated with increased blade loading. If the size and weight reduction can be accomplished without a loss in efficiency, considerable gains are available to the overall propulsion system.

The purpose of this program is to investigate and test advanced concepts to increase turbine blade loading without the associated losses currently encountered. Four concepts are being investigated; they utilize many of the boundary layer control principles associated with high lift devices for aircraft. An advantage of using these control devices in a turbine application rather than aircraft is that the control device is used at all times. This permits the design to be optimized for the specific application rather than being compromised by being useful at one condition and a hindrance at another.

The different concepts being investigated are:

- Vortex generators, often called boundary layer trip devices
- Tangential injection of secondary air
- Tandem airfoil
- Jet flap

A plain rotor blade which has high suction surface diffusion forms the program base line. Following the test of the rotor with plain blades, two different vortex generators are attached to the plain blades in subsequent tests. Tangential injection of secondary air is accomplished by using an airfoil which is identical to the plain rotor blade except for modifications to accommodate the injection slot. Three different slot heights covering the blade span will be tested. The slotted airfoil and the jet flap require entirely different shaped airfoils. Three different jet slot widths will be tested. In all configurations, the blades are designed to the same aerodynamic requirements; the same stator is used for all tests.

This report covers the analysis and design phase of the overall program. The aerodynamic design of the stator and rotor blades is described, plus the analysis and design of the four boundary layer control devices. Also included is the instrumentation plan and the mechanical design and stress analysis of the test rig.

SYMBOLS

A area, $in.^2$

B trailing edge blockage defined as $\frac{s}{s - b}$

b projected trailing edge thickness defined as $\frac{2te}{\sin \alpha_2}$ or $\frac{2te}{\sin \beta_5}$

Cv velocity coefficient

Cj jet momentum coefficient defined as ratio of jet to free stream momentum at point of jet injection

c actual chord, in.

cx axial chord, in.

D spacing or pitch between sets of vortex generators, in.

Ds suction surface diffusion parametric defined as (maximum blade suction - surface relative velocity - blade outlet relative velocity) divided by (maximum blade suction - surface relative velocity)

d spacing or pitch between vortex generators making up one set, in.

$d\beta 1$ stator leading edge fattening factor, degrees

$d\beta 2$ stator trailing edge fattening factor, degrees

E specific work output, Btu/lb

Fx axial component of aerodynamic force on blade, lb

Fy tangential component of aerodynamic force on blade, lb

g acceleration due to gravity, ft/sec^2

Hi boundary layer incompressible form factor defined as $\frac{\delta^*}{\Theta s}$

h vortex generator height, in.

hb injection slot height, in.

Ku stator turning rate control factor defined as the ratio of suction surface radius of curvature at trailing edge orthogonal to radius of curvature at leading edge tangency

J	mechanical equivalent of work, ft-lb/Btu
ℓ	blade height, in.
$\dot{m}$	mass flow rate, lb/sec
N	rotational speed, rpm
n	number of blades
no	length of potential line, in.
P	pressure, psia
R	reaction defined as $\frac{\text{rotor exit relative velocity - rotor inlet relative velocity}}{\text{rotor inlet relative velocity}}$
Rc	radius of curvature, in.
Rg	gas constant, ft-lb/lb_m-°R
r	radius, in.
s	blade spacing or pitch, in.
T	temperature, °R
t	maximum thickness of blade or vane, in.
te	trailing edge radius, in.
tl	leading edge radius, in.
tr	trailing edge flow orthogonal length, in.
u	jet velocity, ft/sec
ur	blade tangential velocity, ft/sec
V	absolute gas velocity, ft/sec
W	relative gas velocity, ft/sec
X	surface length or axial coordinate, in.

y	transverse jet stream coordinate normal to blade surface, in.
Y	tangential coordinate, in.
α	absolute gas angle measured from tangential, degrees
β	relative gas angle measured from tangential, degrees
βa	stator-blade suction surface slope at the trailing edge orthogonal, degrees
βb	stator-blade suction surface slope at the trailing edge, degrees
γ	ratio of specific heats
Δ	incremental change of a variable
δ	boundary layer thickness, in.
δo	ratio of inlet air total pressure to standard sea level conditions
δ^*	boundary layer displacement thickness, in.
ζ	slot angle relative to engine centerline, degrees
ϵ	function of γ defined as $\frac{\gamma^*}{\gamma} \frac{\left(\frac{\gamma+1}{2}\right)^{\gamma/(\gamma-1)}}{\left(\frac{\gamma^*+1}{2}\right)^{\gamma^*/(\gamma^*-1)}}$
Θ	jet deflection, degrees
Θcr	squared ratio of critical velocity at turbine inlet to critical velocity at standard sea level temperature
Θs	boundary layer momentum thickness, in.
ρ	density of gas, lb/ft^3
τ	jet efflux angle, degrees
ϕ	turning downstream of trailing edge orthogonal on suction surface, degrees

ψ	midchannel streamline angle, degrees
ω	angular velocity, radians per second

Subscripts

0	station at stator inlet (all stations shown in Figure 1)
1	station at throat of stator passage
2	station at outlet of stator just upstream of trailing edge
3	station at free-stream conditions between stator and rotor
4	station at throat of rotor passage
5	station at outlet of rotor just upstream of trailing edge
6	station downstream from turbine
a	actual
cr	conditions at Mach number of unity
e	exit plane of nozzle
h	hub radius
I	secondary air inlet station (see Figure 1a)
i	inside of blade cavity
j	jet
m	mean radius and/or midchannel
mj	maximum in jet downstream of injection point
p	primary air stream
ps	pressure surface
rel	relative condition
s	secondary air stream

ss	suction surface
st	static condition
T	stagnation or total conditions
t	tip radius
u	tangential component
x	axial
Y	along radial potential line
∞	free stream at edge of boundary layer
wo/j	without jet-flap
w/j	with jet-flap

Superscripts

	ideal or isentropic condition

TURBINE AERODYNAMIC DESIGN

The design objective of this program is a turbine having high rotor-blade suction surface diffusion and utilizing advanced concepts to achieve this high loading without flow separation.

A single-stage cold air turbine was designed for this investigation. The test unit had a 30-inch tip diameter and a constant hub-tip radius ratio of 0.7. The overall design point characteristics were:

Equivalent specific work output, $E/\theta cr$, Btu/lb	20.0
Equivalent weight flow, $\frac{m_p\sqrt{\theta cr\,\epsilon}}{\delta o}$, lb/sec	45.51
Equivalent blade tip speed, $\frac{(ur)_t}{\sqrt{\theta cr}}$, ft/sec.	610.0

VELOCITY DIAGRAMS

The design velocity triangles at the free stream stations at the stator inlet, stator exit or rotor inlet, and rotor exit were determined on the following assumptions: free-vortex flow, simplified radial equilibrium, and overall total-to-total adiabatic efficiency of 0.84. The stage reaction was adjusted to provide zero exit turbine whirl and negative rotor hub section reaction (R) of -0.25. The station nomenclature and a schematic of the flow path are shown in Figure 1. The free-stream diagrams and the diagrams calculated for stations in the planes of the trailing edge for the stator and rotor are presented in Figure 1c. The diagrams calculated for stations in the planes of the stator and rotor trailing edge were determined by the steps listed in the following text. The example described is for a stator, but the same process is used for a rotor using relative conditions.

1. At a given radius assume that the same total pressure, total temperature, and wheel velocity are the same at stations 2 and 3.

2. Guess a gas angle (α_2) and calculate blockage (B).

3. Calculate $(\rho V_x)_2 = (\rho V_x)_3$ (B).

4. Knowing $(\rho V_x)_2$, V_{u_2}, P_{T_2}, and T_{T_2} at each radial station, calculate total weight flow and compare with design.

5. Iterate on α_2 until continuity is satisfied.

The blade row losses associated with these diagrams are representative of several similar turbines investigated at the Lewis Laboratory. A 3 percent loss in total pressure was assumed across the stator.

The diagrams show a rather large radial variation in flow conditions at the rotor inlet resulting from the low stage reaction at the free vortex whirl distribution. This is evidenced by the variation of stator exit critical velocity ratio V/V_{cr_3} of 1.213 at the hub section to 0.894 at the tip section. Also, the reaction (R) varies for -0.25 at the hub section to 0.71 at the tip section.

Table I is a summary of the temperatures and pressures at various axial stations plus the axial and tangential aerodynamic loads distributed at four radial stations for the stator and rotor.

STATOR DESIGN

The choice of stator solidity and number of blades is based primarily on the work of reference 1 and the use of a trailing edge thickness of 0.030 inches. This results in the use of 40 stator-blades with axial solidities (cx/s) of 0.988 at the hub, 0.923 at the mean, and 0.891 at the tip. The throat dimension (tr) at each station was obtained by the relation

$$tr = (s)(\sin \alpha_2) - 2\,te$$

for subsonic conditions at station 2. If the flow at station was supersonic, the throat dimension was sized to that associated with a flow Mach number of one.

The stator profiles are composed of a series of arcs of circles, involutes, and ellipses. A schematic of the profile is shown in Figure 2. It describes the relative combination of these arcs and the variables required to geometrically describe the profile by Cartesian coordinates. The variables of leading edge radius (tl), fattening factors ($d\beta 1$ and $d\beta 2$), downstream turning (ϕ), and turning rate factor (Ku) are chosen at the discretion of the designer to produce an acceptable airfoil while all other variables are defined by previously discussed aerodynamic considerations. The resulting hub, mean, and tip profile sections (including the tabulated input parameters) are shown in Figures 3 through 5.

Table II is a tabulation of the section profile coordinates. These sections were stacked to obtain a three-dimensional blade shape by orienting the profiles so that the midpoints of the normal across the channel throat lie on a radial line. The sections described on the detailed drawing for fabrication were obtained by interpolating the stacked cylindrical coordinates along flat planes normal to the stacking axis.

The stator surface velocity distributions were obtained by using the calculation procedure described in Appendix A. The resulting velocity distributions are shown in Figure 6. They exhibit very little diffusion on the suction surface downstream of the throat. The velocity distribution in the leading and trailing edge portions (shown by the dashed lines) was estimated because of limitations of channel flow analysis techniques.

PLAIN ROTOR-BLADE

Design

The rotor-blade was designed to a suction surface diffusion parameter (Ds) of 0.3. Preliminary blade profiles were laid out using a combination of solidity, number of blades and trailing edge thickness which are compatible with the recommendations of references 2 and 3. The resulting choice of 76 blades and solidity requirements produce an aspect ratio of 2.0. The final axial chord, or solidity, is the result of several preliminary designs directed toward minimizing solidity while maintaining an acceptable blade thickness and the 0.3 suction surface diffusion parameter.

At the hub, mean, and tip sections, the blade channels were designed in the following manner.

1. The leading edge of the suction surface was laid out parallel to the inlet relative gas angle (β_3). This operation defines the location of points a and c and the midchannel point b as described in the schematic blade layout of Figure 7a.

2. The axial location of the throat midchannel, point d, and the flow angle at the throat are obtained from the geometry illustrated in Figure 7a. The axial distance between points b and d equals the covered turning axial distance; the difference between the inlet and throat angles determines the covered turning angle. A blade midchannel line is developed from the nondimensional turning distribution of Figure 7b. The tangential position of point d with respect to point b is established by generation of the midchannel line.

3. A sinusoidal variation of half-passage width as a function of covered turning is drawn as illustrated in Figure 7a. A series of circles, whose radii are the half-passage width, are drawn with their centers appropriately located at the proper axial station on the midchannel line.

4. A channel shape is drawn by a spline fitting tangent to the circles drawn in Step 3. Exact tangencies are not always possible to obtain. Therefore, the circles are used only as a guide for drawing the channel.

5. The pressure surface of the channel is translated down an amount equal to the spacing to generate the blade section.

6. A leading edge circle is drawn tangent to the pressure and suction surfaces approximately at the inlet straight line tangency point.

7. The blade surface velocity distribution was calculated using the procedure described in Appendix A, and the blade surface contour was modified to obtain the required blade suction surface diffusion parameter.

8. The resulting cylindrical blade profiles were stacked so that the center of gravity of each section lies in the meridional plane and that the extreme leading edge point of the blade also lies in a plane normal to the axis of rotation. The blade section coordinates accompanying the detailed drawing for fabrication were obtained by interpolating between the design cylindrical profiles along flat planes normal to the stack axis. The section coordinates are presented in Table III.

The cylindrical developments of the rotor-blade profiles are shown in Figure 8. The blade surface velocity distribution was obtained by the calculation procedure described in Appendix A. The resulting surface velocity distribution is shown in Figure 9 as a function of axial chord. The variation of blade section surface length is presented as a function of axial position in Figure 10, and the suction surface equivalent static pressure distribution is shown as a function of suction surface length in Figure 11.

Boundary Layer Characteristics

An analysis of the boundary layer characteristics on the plain rotor-blade suction surface was conducted to evaluate the boundary layer thickness, momentum thickness, and the incompressible form factor. These variables were obtained by the use of Truckenbrodt's method (reference 4) as applied to a two-dimensional, compressible, turbulent boundary layer using the transformations of Culick and Hill (reference 5). Knowledge of the boundary layer characteristics is required to predict and locate flow separation and aid in the design and location of various boundary layer control devices to prevent incipient separation.

The calculated incompressible form factor (Hi) is shown in Figure 12. Separation is predicted to occur when the magnitude of Hi exceeds 1.8. Examination of Figure 12 indicates that separation occurs at axial stations of 1.45 inches at the hub, 1.36 at the mean, and 1.36 at the tip. Using Figure 10, these values translate into blade surface distances from the leading edge

of 1.88 inches at the hub, 1.63 at the mean, and 1.48 at the tip. The momentum thickness (θ_s) (also obtained from Truckenbrodt's method, reference 4) at the point of incipient separation is 0.006 inches at the hub, 0.004 at the mean, and 0.0034 at the tip. Using these values in conjunction with information from an unpublished paper by H. H. Korst, the magnitude of the boundary layer thickness was obtained. These data are illustrated in Figure 13 with values of δ at incipient separation of 0.048 inches at the hub, 0.032 at the mean, and 0.028 at the tip.

BOUNDARY LAYER CONTROL DEVICES

The analysis of the turbulent boundary layer on the plain rotor-blade indicates flow separation on the suction surface at all radial sections. Four different concepts were investigated to forestall or prevent this flow separation. The concepts investigated were vortex generators, tangential slot blowing, tandem airfoils, and the jet-flap. The first two concepts are directly applied to the plain airfoil whereas the latter two concepts required entirely new airfoil designs to employ the specific concepts.

VORTEX GENERATORS

The principle of boundary layer control with vortex generators relies primarily on mixing between the free stream and the boundary layer. Vortices trailing over the surface downstream from the generator sweep high momentum air from the free stream into the boundary layer, replacing the low momentum boundary layer fluid generated by surface friction and adverse pressure gradients. This reenergization of the boundary layer occurs over an appreciable distance downstream of the vortex generator, permitting the flow to negotiate considerably larger pressure gradients without separation.

An investigation of the various types of vortex generators was initially conducted. Two basic types were selected and are categorized as vane-type and three-dimensional bodies.

Schematics of the various vane-type generators are shown in Figure 14. These generators find wide acceptance in high free-stream Mach number applications and are particularly suited for prevention of shock-induced separation. Of the various types illustrated in Figure 14, the reference material (reference 6) indicates that the effectiveness of the co-rotating system is good over a wide range of design variables. Both the counter-rotating and the biplane systems have slightly better performance but require considerably more care in design to realize their full potential. The wing-type generators also give good performance and are very insensitive to incidence but would present extreme mechanical problems when mounted in the presence of a high centrifugal field.

Schematics of the three-dimensional vortex generators are shown in Figure 15. These systems proved attractive since the finite minimum thickness of the vane-type generators often forced the two-dimensional surfaces to degenerate into three-dimensional bodies when reduced to the size of this project. Although little high speed data are available for three-dimensional generators, they appear rather attractive from both mechanical and aerodynamic considerations.

Design Considerations

The vortex generators chosen for this application and their physical characteristics and location are the result of an integrated balance between aerodynamic and mechanical scale considerations. The local free-stream flow conditions presented in Figure 9 contributed to the placement and physical characteristics of the generators. From a mechanical point of view, a number of compromises had to be made to the optimum aerodynamic design. For example, a thickness of 0.015 inch represents a mechanical limitation for vane-type generators. Therefore, when design rules call for a generator height of 0.030 inch, the design must be invalidated since the system has degenerated from a "thin-vane" to a "block" whose width is half the height. Other considerations include fabrication problems and associated braze fillet radius. A minimum radius of 0.010 inch also detracts from the "two-dimensional vane" and leads to the "three-dimensional body" concept. The presence of the high centrifugal field combined with the potential application to high temperature environment has also contributed to the design considerations.

Co-Rotating Vortex Generators

This vane-type vortex generator was chosen for its high performance without the need of excessive development to "fine tune" the system. It is a simple mechanical arrangement and easily fabricated. In view of the complex nature of the flow within a turbine, it is also attractive because of its relative insensitivity to local flow distortions. The system produces a component of flow normal to the main stream in the direction which the trailing edge points. By orienting the vanes such that this flow component is radially inward, high energy air is forced into the high loss area of the hub platform.

The vane height designed for this application is 0.050 inch and is located at an axial chord of 0.64 inch at all sections. The choice of 0.050 inch height, in conjunction with a vane thickness of 0.015 inch, represents a balance between aerodynamic and mechanical considerations. Most successful vortex generator designs have a generator height equal to or greater than the boundary layer thickness at the location of the vortex generator. The further aft the location on the suction surface, the thicker the boundary layer and, therefore, the larger the requirement of generator height. Data indicate increasing (h) tends to increase vortex strength with some increase in drag. However, the magnitude of the drag increase is not well documented, and large increases in generator drag still represent a relatively small percentage of increase in drag of the overall airfoil. The work of the National Physical Laboratory (reference 6) was conducted at an (h) equal to one percent of the chord. Considering the chord equal to 2.8 inch results in an (h)

of 0.028 inch. Although this height could be fabricated, it would result in a 0.015-inch wide "block" rather than a thin vane. The ratio of generator height to the boundary layer thickness at the location of the generator (h/δ) are 2.0 at the hub, 3.8 at the mean, and 5.5 at the tip. The hub and mean values are similar to the (h/δ) ratios of reference 6. The parameter (h/δ) is a good index of the strength of the vortex produced and, therefore, the range or effectiveness of the generator. Comparison of the (h/δ) ratios of this design to the data of reference 6 indicates sufficient effectiveness based on this index.

The choice of axial surface location of the vortex generator is strongly related to the generator height, boundary layer thickness, surface length, and point of incipient separation. The axial location must be a sufficient distance upstream of the uncontrolled separation point to permit adequate mixing of the vortex flow and the boundary layer. The predicted location of uncontrolled separation for the plain blade is illustrated in Figure 10. A comparison of the plain airfoil characteristics can be made to the test model of the National Physical Laboratory (reference 6). Consider the ratio of the plain airfoil maximum thickness to the camber line length as analogous to the (t/c) ratio of a symmetrical airfoil distributed on a camber line. The test airfoil of reference 6 was a symmetrical airfoil with zero camber and had a (t/c) ratio of 0.16. The plain airfoil has (t/c) ratio from 0.15 at the hub to 0.11 at the tip. The vortex generators of the NPL test airfoil were placed at approximately 30 percent of the chord. Applying this rule to the 2.8-inch suction surface length (which approximates the camber line length) results in the choice of axial location of 0.64 inch. Approximately 0.08 inch of surface length exists between the generators and the point of uncontrolled separation. The data of reference 6 indicate that co-rotating generators are effective for at least 100 generator heights downstream at a free-stream Mach number similar to those on the plain airfoil. Effectiveness of this magnitude will extend beyond the plain rotor trailing edge. The effectiveness, or range, of the data of reference 7 is illustrated in Figure 16. These data also indicate that sufficient range exists for this design when examined on the basis of range per unit generator height. Another important consideration is the local free-stream Mach number at the location of the generators. The potential presence of bow shocks from adjacent blades must also be considered when locating the vortex generator. The free-stream critical velocity ratios at the vortex generators are 0.93 at the hub, 0.96 at the mean, and 1.01 at the tip. Therefore, local shock losses can be neglected.

The prime variable affecting the performance of co-rotating generators is the ratio of vane spacing to vane height. This value should always be larger than three with recommended values of four to eight. The remaining vane geometry is well documented in reference 6 with recommended spacing equal to six generator heights and vane chords equal to four heights. Recommended incidence is 20°. A schematic of the generator placement on the plain airfoil is shown in Figure 17.

Triangular Plow

The triangular plow overcomes many of the mechanical scale problems associated with the relatively small physical size of this application. The performance, based on both static pressure rise and drag, of this type vortex generator at low free-stream velocities is comparable to that of vane-type vortex generators. There is evidence that vane-type generators are superior to the plow. However, because the plow is truly a three-dimensional body, it should not suffer the potential performance problem of a two-dimensional system degenerating to a three-dimensional body. It also offers a very rugged configuration, making it somewhat more attractive for application in high temperature and/or an erosive atmosphere.

A triangular plow geometrically similar to the plow described in reference 7 was used as a model. The location, height, and performance of these vortex generators are illustrated in Figure 16. Defining the distance between generator location and uncontrolled separation as (X) results in (X/h) ratios of 164 for generator E1, 12 for E2, and 0.5 for E3. Between E1 and E3 there is little gain in range for the large latitude in this design parameter. The subject generator was designed with a height of 0.060 inch which represents a 0.010-inch increase above the co-rotating vane. This was done because the reference data indicate that a plow requires somewhat greater height than the vane for equal vortex range and strength. Since both the vane and plow extend considerably above the boundary layer, it is questionable that the plow need be significantly higher. With this design, (X) is approximately equal to 0.8 inches for all sections, resulting in an (X/h) ratio of 13.3.

Consideration was also given to the effect of generator spacing or pitch on the performance of configurations E1, E2, and E3. Defining the pitch equal to (D) results in (D/h) ratios of 8, 4, and 2. In view of the fact that the published spacing and placement of reference 7 produces maximum static pressure rise for minimum drag, it is possible this is far from being synonymous with maximum range. It is felt that generators E2 and E3 suffer from the same deficiency as vane-type generators with insufficient spacing. Under these circumstances, the vortices of adjacent generators tend to damp out each other, resulting in only a slight increase in range at a large increase in drag. Considering the height of the proposed triangular plow relative to the boundary layer thickness, it should be possible to generate sufficient vortex strength and range and also use the large (D/h) ratio equal to 8.

The physical dimensions of the plow are shown in Figure 18, and the detailed spacing and placement of the generators on the suction surface of the plain blade are illustrated in Figure 19.

TANGENTIAL SLOT BLOWING

The prevention of flow separation by tangential slot blowing functions on the principle of "reenergizing" the boundary layer. This is also the same principle on which the vortex generator operates. Tangential slot blowing uses a secondary air source to supply energy to the low momentum fluid of the boundary layer, whereas the vortex generator sweeps the high energy fluid from the mainstream into the boundary layer. The secondary air is injected as parallel to the mainstream flow as possible. However, in many applications angle differences between the jet and mainstream of as much as 30 degrees have been used quite successfully. Tangential slot injection is often categorized as a "high-lift device" because it is often used on flapped aircraft wings to prevent separation from the highly cambered trailing edge portion of the wing. This is essentially the same flow phenomenon associated with highly loaded turbine blades. In view of the successful application of slot blowing to aircraft applications, it seems the principle is also well suited for application to the plain rotor-blade.

The analysis and design of the tangential slot blowing blade was the first system investigated to use secondary air. Therefore, the design also includes the analysis of the secondary air induction system. The system was designed to be capable of passing at a low pressure loss at least 10 percent of the primary flow rate with the maximum total pressure of the secondary flow equal to the turbine inlet pressure. In all cases, the secondary air total temperature is equal to the turbine inlet total temperature.

Figure 20 is a schematic of the wheel assembly and shows each wheel passage feeding two blades. The calculated velocity distribution in these passages is presented in Figure 21. The radial variation of secondary air total temperature and pressure inside the blade cavity is listed in Table IV.

Slot Sizing and Location

The results of reference 8 were used in the design of the injection slot. The author of reference 8 recommends locating the slot a distance of six boundary layer thicknesses upstream of the point of separation. It is also recommended that the secondary mass flow rate should be such that the momentum excess of the jet is equal to the momentum deficiency of the boundary layer at separation, i.e.,

$$(\rho_{ss})\,(W_{ss}^2)\,(\theta s) = (\rho_j)\,(u_a)\,(y)\,(u_a - W_{ss}) \qquad (1)$$

Further, the results of reference 8 imply that an optimum velocity ratio, $u_a/W_{ss} = 1.2$, should be used.

The jet velocity was determined by considering the secondary flow relative total conditions inside the blade with the mainstream flow conditions at a point equal to $(6\delta)'_s$ upstream of the point of incipient separation. The ratio of total pressure inside the blade to mainstream static pressure indicated that the jet velocity would be supersonic; therefore, the tangential slot should be of a converging-diverging configuration. Because of manufacturing difficulties in fabricating a small converging-diverging slot in a turbine blade, it was decided to make the nozzle a straight-walled passage. Sonic conditions will exist at the nozzle throat, and it was assumed that the jet stream would expand isentropically to supersonic conditions just downstream of the nozzle exit. The deviation of the actual jet expansion from the isentropic expansion was corrected for by a velocity coefficient given by Higgins and Wainwright (reference 9). The velocity coefficient was defined as $Cv = u_a/u'$ and was nearly independent of the nozzle expansion pressure ratio $\left(P_{T_{i(rel)}}/P_{st_{ss}}\right)$. A conservative value of Cv = 0.97 was selected for the present analysis. The height of the secondary stream (y) at the location where the secondary stream had expanded to the supersonic conditions was determined by rearranging and solving equation (1):

$$y = \frac{\rho_{ss}}{\rho_j} \frac{\left(\frac{W_{ss}}{u_a}\right)^2 \Theta s}{\left(1 - \frac{W_{ss}}{u_a}\right)}$$

The slot height (hb) was then obtained from

$$hb = \frac{A_{cr}\, y}{A}$$

The suction surface static pressure at the point of injection, hub, mean, and tip is shown in Figure 11. The secondary air total relative temperatures at the hub, mean, and tip are shown in Table IV. These two variables, when combined with various chosen values of secondary air total relative pressure, yield corresponding values of jet to free-stream velocity ratio and slot height as functions of the ratio of blade cavity to free-stream total pressure. These functions are illustrated in Figures 22 and 23, respectively. These curves show that for a given pressure ratio the slot height should vary in the radial direction, being larger at the blade hub than at the tip. However, because of manufacturing considerations, it was decided to make the slot height constant in the radial direction. The calculation also shows that the blade mean and tip sections required nearly the same slot height; most of the slot height variation occurred between the mean and hub sections. The static pressure distribution presented in Figure 11 indicates that the most severe

adverse pressure gradient, and hence critical operating condition, occurs at the blade tip. Therefore, as far as prevention of flow separation by tangential blowing was concerned, it was decided to size the slot according to blade mean and tip section calculations and accept the momentum deficiency which would result at the blade hub.

The radial variation of the total conditions is the same both inside the secondary flow cavity and outside the blade in the mainstream flow. Therefore, a given total pressure ratio $(P_{T_i}/P_{T_{SS}})$ is constant for the hub, mean, and tip blade sections. The variation of total pressure ratio $(P_{T_i}/P_{T_{SS}})$ with inlet region total pressure $(P_{T_i}/\delta o)$ is shown in Figure 24. The secondary mass flow per unit length $(\dot{m}_S/\ell)$ was calculated at several different total pressure ratios $(P_{T_i}/P_{T_{SS}})$, and a corresponding radially constant slot height was selected from Figure 23. An expression describing the radial variation of secondary mass flow per unit length as a function of section radius was derived for each total pressure ratio. This expression was then integrated from the blade hub to tip:

$$\dot{m}_S = \int_{r = 10.5 \text{ in.}}^{r = 15 \text{ in.}} \frac{\dot{m}_S (r)}{\ell} \, dr$$

The percent mainstream flow was then obtained by dividing the calculated secondary mass rate of flow by the mainstream mass rate of flow $(\dot{m}_p)$ where $\dot{m}_p = 45.51$ lb/sec. The variation of $\dot{m}_S/\dot{m}_p$ with total pressure ratio $\left(P_{T_i}/P_{T_{SS}}\right)$ is shown in Figure 25.

Based on the results of these calculations and the optimum velocity ratio $(u_a/W_{SS}) = 1.2$, the following slot design parameters were selected:

- Design total pressure ratio $(P_{T_i}/P_{T_{SS}}) = 1.3$
- Radially constant slot height of 0.016 inches cut at an axial chord of 1.25 inches
- A secondary mass flow rate of 3 percent based on secondary air total conditions at Station I (Figure 1a) of 518.7°R and 10 psia. The resulting radial velocity distribution leaving the slot is as follows:

	u_a/W_{SS}	u_a (ft/sec)
Hub	1.24	1150
Mean	1.21	1225
Tip	1.19	1270

The range or effectiveness of the design can be obtained by comparison of required adverse rise of static pressure ratio for a given total pressure ratio ($P_{T_i}/P_{T_{SS}}$). The most severe adverse pressure gradient to be negotiated exists at the tip section of the plain rotor-blade. These data are shown in Figure 11 and indicate that 1.6 is the maximum ratio of trailing edge static pressure to suction surface static pressure at the point of injection. The results of reference 8 show an adverse static pressure ratio of 2.0 was negotiated with a total pressure ratio ($P_{T_i}/P_{T_{SS}}$) = 1.3. Based upon these results, one slot should be sufficient to prevent flow separation from re-occurring.

Alternate Slot Heights

It was cited earlier that the optimum secondary flow conditions were considered to be a total pressure ratio ($P_{T_i}/P_{T_{SS}}$) of 1.3 operating across a uniform, straight-walled nozzle with a height equal to 0.016 inches. It is desirable to design the slot configuration such that additional slot heights could be tested. The initial blade test would be run with the minimum slot height. This minimum height would then be opened up for the subsequent tests. It is felt that the maximum information can be obtained from the experimental program if both larger and smaller slot heights than the optimum are tested.

It was shown earlier on Figure 23 that for a given total pressure ratio ($P_{T_i}/P_{T_{SS}}$) the slot height should vary in the radial direction. For a pressure ratio of 1.3, the mean and tip slot heights were 0.016 inches; the hub required a slot height of 0.022 inches. This means that since the slot is undersized at the hub, there will be a deficiency in momentum at the hub as far as prevention of flow separation by tangential injection is concerned. Therefore, it is planned to test a slot height of 0.022 inches. This slot height, used in conjunction with a total pressure ratio ($P_{T_i}/P_{T_{SS}}$) of 1.3, should provide the correct momentum at the hub. There will be an excess of momentum at the mean and tip sections.

The minimum slot height that can be economically manufactured is 0.010 inches. With reference to Figure 23, it can be seen that the smaller slot heights are accompanied by large total pressure ratios ($P_{T_i}/P_{T_{SS}}$) which, in turn, mean large velocity ratios (u_a/W_{SS}). Thus, the momentum deficit of the boundary layer is made up by injecting a relatively small quantity of high velocity fluid into the boundary layer. The implication is that this procedure may be the most economical way to prevent flow separation, provided that secondary flow at the higher pressure level is available. The reason for this is that a certain amount of energy must be supplied to the boundary layer

flow if flow separation is to be prevented, and this energy must be charged to the whole engine system. Thus, if a smaller quantity of secondary flow would be required to prevent separation, then less energy would be extracted from the whole engine system. Therefore, it was decided that the third alternate slot height should be 0.010 inches. In summary, the three recommended slot heights are 0.010, 0.016, and 0.022 inches.

Blade Geometry Downstream of Slot

It was desired to keep the primary flow channel exit velocity diagrams identical with those of the plain blade. Therefore, it was necessary to increase the channel cross-sectional area to accommodate the additional secondary mass flux. It was assumed that a fluid particle which was associated with the secondary jet stream at the slot location would retain its jet identity all the way to the blade trailing edge. That is, it was assumed that no mixing would take place between the jet stream and the mainstream between the slot location and the blade trailing edge. Thus, the amount and location of metal removed from the blade suction surface depended on the transverse growth of the secondary jet stream as it proceeded from the slot location to the blade trailing edge. The transverse growth of the jet was obtained from the continuity equation at the hub, mean, and tip blade sections:

$$\dot{m}_s = (\rho_j)\,(y)\,(u_a)\,(n)\,(\ell)$$

and

$$\frac{\dot{m}_s}{\ell} = (\rho_j)\,(y)\,(u_a)\,(n)$$

A schematic of the blade geometry downstream of the slot is shown in Figure 26. At the slot location X = 0 and y = hb. Therefore,

$$X/hb = 0$$

and

$$\frac{\dot{m}_s}{\ell} = (n)\,(\rho_j\ hb\ u_a)_{X/hb\,=\,0}$$

At the trailing edge flow othogonal

$$\frac{X}{hb} = 37.5$$

and it is assumed that

$$\left(\frac{\dot{m}_s}{\ell}\right)_{(X/hb = 37.5)} = \left(\frac{\dot{m}_s}{\ell}\right)_{(X/hb = 0)} = \left(n\right)\left(\rho_j \; y \; u\right)_{(X/hb = 37.5)}$$

A measure of the deterioration of the jet velocity is shown in Figure 27. This figure presents the ratio of the jet velocity at any (X/hb) value to the jet velocity at (X/hb) = 0 as a function of the (X/hb) ratio and the ratio of the free-stream velocity to the jet velocity at the slot. For this design, the ratio of free-stream to jet velocity at the slot $(W_{ss}/u_a)_{(X/hb = 0)}$ is equal to 0.83. Therefore, the ratio of jet velocity at (X/hb) = 37.5 to the jet velocity at the slot (X/hb) = 0 is equal to 0.425. It is now possible to calculate the jet velocity at the trailing edge flow octogonal (X/hb) = 37.5. It was also assumed that the jet relative total temperature at any radial section was constant at any location (X) and that the static pressure in the jet was equal to the suction surface static pressure of the plain blade as shown in Figure 11. These functions describe the local jet static density from which the jet thickness (y) may be calculated. The results of these calculations are tabulated in Table V.

The new blade suction surface was formed by first passing a smooth curve through the surface dimension (y) at the slot location (X/hb) = 0. Then the curve was passed through the calculated (y) dimension at the throat (X/hb) = 37.5 and finally made tangent to the trailing edge circle. The modified profiles of the plain rotor blade illustrating the blade interior shape and the slot configuration are shown in Figure 28.

TANDEM ROTOR-BLADE

This rotor is designed to meet the same velocity diagram requirements as the plain rotor-blade. The philosophy of design is to distribute the overall turning between two airfoils. This allows each airfoil to start its part of the turning process with a new, thin boundary layer preventing boundary layer buildup and eventual separation if all the turning is performed on one surface. The forward airfoil is referred to in this report as the primary airfoil, and the aft airfoil is referred to as the secondary airfoil.

Airfoil Design

The aft portion of the secondary airfoil was maintained as identical to that of the plain airfoil as possible. The axial location of the overlap of the two airfoils was chosen in the region of predicted separation of the plain airfoil. The additional blade surface area available because of the overlap permits a reduction in the axial chord of approximately 10 percent without increasing the blade loading above that of the plain blade. The position of the secondary airfoil relative to the primary airfoil is the result of several preliminary designs beginning with the secondary airfoil halfway between the

primary airfoil. Successive designs brought the secondary airfoil suction surface closer to the primary pressure surface in an attempt to reduce pronounced discontinuities of surface velocities on the airfoils. The procedure used to establish the mass flow distribution between the "slot" and "main channel" is as follows:

1. The suction surface critical velocity ratio at the trailing edge of the primary airfoil, hub, mean, and tip was calculated based on an assumed mass flow rate across potential line (1) of Figure 29.

2. The pressure surface critical velocity ratio at the trailing edge of the primary airfoil, hub, mean, and tip was calculated based on a flow rate across potential line (2) of Figure 29 which is equal to the total flow rate minus the flow rate assumed in step 1.

3. Steps 1 and 2 were repeated until the suction and pressure surface critical velocity ratios of the primary airfoil are essentially equal to establish the mass flow distribution.

The distribution of this design resulted in 25.7 percent of the total flow rate passing through the slot. The calculation procedure used to predict the blade surface velocity distribution was the same as that used for the plain blade and is described in Appendix A. The "slot" and "main channel" are treated separately using their respective flow rates. The portions from the primary to secondary leading edges and from the primary to secondary trailing edges are also treated separately using the total mass flow rate. Since the blade has a variable axial chord, the potential lines at each section were not taken at common axial stations. Instead, the normals were taken at common percentages of the axial distance in the "covered" turning portion of each airfoil. The total relative pressure was assumed to vary linearly in the axial direction. The final position of the two blades reduced the rapid decelerations in the calculated suction surface velocities. The resulting critical velocity ratio distributions are illustrated in Figure 30, and a summary of the diffusion parameters is given in Table VI. The airfoil profiles are shown in their relative positions at the hub, mean, and tip sections in Figure 31, and the section coordinates are presented in Table VII.

Boundary Layer Analysis

The boundary layer characteristics of the primary and secondary airfoil suction surfaces were evaluated by the same method as used on the plain airfoil. The suction surface length of the tandem blade as a function of axial position is presented in Figure 32. The boundary layer incompressible form factor (Hi) is presented for the primary and secondary airfoils as a function of surface length in Figure 33. Examination of these plots reveals no separation at the tip nor on the mean section primary airfoil. Both airfoils at the

hub section and the secondary airfoil at the mean have form factors of 1.8 very near the trailing edge of each foil. The resulting disturbance is very close to the trailing edge, and it is believed that it will be lost in the trailing edge wake and can therefore be neglected.

JET-FLAP

The jet-flap principle uses a jet sheet of air effluxing from an airfoil at an angle to the pressure surface along the trailing edge. The interaction of the stream and jet causes both streams to deflect resulting in an altered velocity and static pressure distribution on the airfoil. The additional turning of the mainstream by the jet generates a greater lift, thereby increasing the work capacity of the airfoil. The application of this high lift device to a turbine blade would result in a blade designed for a smaller work requirement than the plain blade. The additional work required would be supplied by the deflection of the mainstream by the jet. The jet-flap reduces or "unloads" the basic work requirement of the airfoil from that of the plain blade by approximately 10 percent. The jet-flap blade was designed to have approximately the same maximum suction surface velocities as the plain blade. Without the flap, the analysis indicates separation on the suction surface. With the jet-flap, the design analysis indicates no separation at design equivalent work.

Design Considerations

Several interrelated variables were investigated to establish a relationship with the design requirements. The related variables are:

1. The downstream, after mixing, velocity diagrams as a function of the percent of secondary flow

2. The deflection characteristics of the jet and mainstream as a function of the jet efflux angle (τ), the jet momentum, and the mainstream momentum

3. The selection of the percentage of secondary flow and its energy or pressure level as it affects the design (It is recognized that freedom of this design variable will not exist in all designs.)

After complete mixing of the jet and primary streams, the downstream velocity triangles were examined as a function of the percentage of secondary flow. No mixing losses were charged to the system; therefore, the total temperature and pressure of the mixed streams were assumed to be equal to those of the plain airfoil velocity diagram. The total mass flow of the system was the only function varied by assuming various percent additions of secondary flow. The resulting variation of mean-line relative exit gas angle $(\beta_6)_m$

with the percent of secondary flow is shown in Figure 34a, and the nomenclature of the jet-flap design variable is depicted in Figure 34b.

The jet deflection characteristics used are a correlation of data presented in references 6, 10, and 11. This correlation is presented in Figure 35 and shows the mainstream deflection (θ) as a function of the jet efflux angle and the jet momentum coefficient. The jet momentum coefficient is defined as the ratio of jet stream momentum to the mainstream momentum. Examination of these data readily indicates that for a given jet momentum coefficient the maximum effectiveness or deflection is obtained when the efflux angle (τ) is 90°.

The amount of secondary air and the pressure or energy level at which it would be supplied at the rotor inlet was selected from a study of the relation of the jet momentum, its deflection characteristics, and the slot width required to pass this flow. This study was based on calculations using a jet velocity coefficient of 0.97 based on the data of reference 9. The jet was assumed to expand from the blade cavity total relative pressure to the static pressure downstream after mixing based on the percent secondary flow under investigation. The total absolute and relative temperatures of the secondary air are the same as the tangential slot blade design. A design value of five percent secondary flow at a system inlet pressure (P_{0_I}) of 10 psia was selected. This combination gave deflections which sufficiently "unloaded" the airfoil and required a slot width which was reasonable for the size blade under consideration. This combination also allows margin to investigate larger slot widths and the effects of various secondary air supply pressures. The results of this study relating mean jet momentum with slot width and secondary air supply pressure are illustrated in Figure 36. The downstream velocity diagram based on five percent secondary air is shown in Figure 37. A summary of the jet flow properties is presented in Table VIII.

Airfoil Design

Manufacturing considerations require that the slot angle relative to the axis of rotation (ζ) be maintained constant at all radial stations. Therefore, to obtain maximum effectiveness from the jet momentum, taking into consideration manufacturing requirements and the variation from hub to tip of the midchannel streamline angle at station 4, requires the jet efflux angle at the hub (τ_h) to be 90°. Also, it is required that the mainstream and jet flow satisfy simple radial equilibrium, continuity, and the jet deflection characteristics between the trailing edge flow orthogonal and the downstream mixed conditions. The number of blades was chosen equal to that of the plain blade. The solidity was reduced approximately 10 percent from that of the plain blade. This reduction was chosen to maintain nearly the same blade surface loading as the plain blade.

The design of the jet-flap blade is initiated at the blade mean-line trailing edge orthogonal. The sequence of design steps follows:

1. Assume a design work for the mean-line airfoil section without the jet. Calculate the whirl requirements at station 6 knowing the flow conditions at station 3. The design assumes that:

$$\left(V_{u_6}\right)_{wo/j} = \left(V_{u_4}\right)_{wo/j} = \left(V_{u_4}\right)_{w/j}$$

2. Assume a mean-line jet efflux angle (τ_m).

3. Assume a mean section trailing edge flow orthogonal dimension $(tr)_m$.

4. Assume a mean-line midchannel streamline angle at the trailing edge flow orthogonal (ψ_4). Knowing (ψ_4), (V_{u_4}), and (W_{u_4}), calculate (W_4) from the trigometric relation of the velocity triangle. The assumed (ψ_4) and $(\beta_{6_m})_{W/j}$ define the required jet deflection, or

$$\Theta\,(\text{required}) = (\psi_4) - \left(\beta_{6_m}\right)_{w/j}$$

5. Calculate the jet momentum coefficient $(Cj)_m$ as a function of (W_4) from step 4 and $(tr)_m$ of step 3. Obtain Θ from Figure 35 as a function of $(Cj)_m$ and the assumed (τ_m) of step 2. Iterate on (ψ_4) of step 4 until (Θ) of step 4 equals (Θ) of step 5.

6. Calculate the mean-line trailing edge flow orthogonal $(tr)_m$ based on one-dimensional flow, or

$$(tr)_m = \mathcal{f}(\dot{m},\ T_{T_{4(rel)}},\ P_{T_{4(rel)}},\ \ell,\ n)$$

The relative total pressure at station 4 is assumed equal to that for the plain blade. If the calculated $(tr)_m$ is not equal to that assumed in step 3, the assumed value is adjusted and steps 3 through 6 are repeated.

7. Define the hub and tip trailing edge flow orthogonal dimensions, $(tr)_h$ and $(tr)_t$. The characteristics of $\cos^{-1}(tr/s) = \mathcal{f}(r)$ was adjusted to parallel the characteristic of $(\beta_6)_{w/j} = g(r)$.

8. Establish the relationship of $(W_4)_h$, $(W_4)_t$, and $(\psi_4)_t$ with $(\psi_4)_h$ for constant values of $(\psi_4)_m$ and $(W_4)_m$, assuming simple radial equilibrium. These characteristics are depicted in Figure 38 for constant magnitudes of $(W_4)_m$ = 700 ft/sec and $(\psi_4)_m$ = 36.8 degrees. The values of $(W_4)_h$ and $(W_4)_t$ shown in the figure are almost invariant with $(\psi_4)_h$ and $(\psi_4)_t$.

9. Calculate the jet momentum coefficients at the hub and tip based on the defined flow orthogonals of step 7 and the assumed mainstream velocities of step 8. Recall also that

$$\tau = 90 - (\psi_4) + \zeta$$

$$\Theta = 90 - (\beta_6)_{w/j} - (\psi_4)$$

but ζ is constant, hub to tip, and is known. The $(\beta_6)_{w/j}$ term is known from the velocity diagrams, therefore, τ = constant + Θ. Knowing Cj, the preceding relation, and the characteristics of Figure 35, calculate (Θ), (τ), and (ψ_4) at the hub and tip. Simultaneously, adjust $(W_4)_h$ and $(W_4)_t$ until the calculated $(\psi_4)_h$ and $(\psi_4)_t$ satisfy simple radial equilibrium as defined in step 8. Note that relative small changes in $(W_4)_h$ and $(W_4)_t$ produce significant changes in $(\psi_4)_h$ and $(\psi_4)_t$, aiding to rapidly close the iteration.

10. If the jet efflux angle at the hub (τ_h) is not equal to 90 degrees, the assumed value at the mean line of step 2 is readjusted and the process repeated from steps 2 through 10.

11. Test for continuity using the relation

$$\dot{m}_p = n \int_{r_h}^{r_t} (\rho)\,(tr)\,(W_4)\,dr$$

If continuity is not satisfied, it is necessary to adjust the assumed work capacity of the mean-line airfoil section of step 1 and repeat steps 1 through 11. If continuity is satisfied, the radial variation of trailing edge flow orthogonal and midchannel flow angle is defined.

The blade trailing edge thickness chosen is compatible with slot width, minimum blade wall thickness requirements, and the secondary flow aerodynamic requirements inside of the blade. Blade section shapes are then drawn in the same manner as the plain blade. The blade surface curvatures and passage widths are adjusted to produce suction surface velocities approximately equal to those of the plain blade. The analysis of the blade surface velocities without the jet was obtained using the procedure described in Appendix A. The resulting blade sections are shown in Figures 39, 40, and 41 for the hub, mean, and tip, respectively; the section coordinates are listed in Table IX. The associated surface critical velocity ratio distributions are shown in Figures 42, 43, and 44 for the blade without the jet.

A jet contour was added to the section profiles at the trailing edge to analyze the effect of the jet-flap on the blade surface velocity distribution and work capacity. The contour was established from the linearized airfoil technique described in Appendix B. The jet contour was maintained constant, and the only portion of the jet contour that was used was the initial portion which matched the required deflection. The blade sections were analyzed using an incompressible, two-dimensional relaxation solution of the Laplace equation. The analysis was performed with and without the jet-flap contour. The resulting static pressure distributions are shown in Figures 45, 46, and 47 at the hub, mean, and tip, respectively. For a basis of comparison and evaluation, this analysis was also performed on the plain blade which also was designed for an equivalent work of 20.0 Btu/lb. These data are shown in Figures 48, 49, and 50 for the plain blade hub, mean, and tip, respectively. It was possible to evaluate the effect of the jet-flap on the blade section work capacity by two methods:

1. The first method is obtained by proportioning the integrals.

$$(E)_{w/j} = \left[\frac{ur_3V_{u_3} - ur_4V_{u_4}}{gJ}\right]_{wo/j} \frac{\left(\int_0^{cx} \Delta P\, dx\right)_{w/j}}{\left(\int_0^{cx} \Delta P\, dx\right)_{wo/j}}$$

   This method assumes no change in tangential momentum from the trailing edge flow orthogonal to the downstream station.

2. The second method was to proportion the static pressure integrals of the jet-flap and plain blade to the design equivalent work of the plain blade, or

$$(E)_{w/j} = (20.0) \frac{\left(\int_0^{cx} \Delta P \, dx \right)_{w/j}}{\left(\int_0^{cx} \Delta P \, dx \right)_{\text{plain blade}}}$$

The resulting comparisons of blade section work capacities presented in Table X indicate reasonable agreement of work capacity using the deflection data of Figure 35 and the relative ratios of work from a two-dimensional incompressible analysis.

Boundary Layer Analysis

The boundary layer characteristics of the blade without the jet were analyzed from the compressible solution velocity distribution of Figures 42, 43, and 44. The analysis procedure used to evaluate the boundary layer characteristics was the same procedure as used for the plain blade. The resulting boundary layer incompressible shape factor (Hi) is presented for the hub, mean, and tip in Figure 51. Although a value of 1.8 has not been reached up to the trailing edge flow orthogonal, any reasonable velocity extrapolation would indicate almost immediate separation without the jet-flap.

The quasi-three-dimensional stream filament procedure used to analyze the blade without the jet-flap is only applicable up to the trailing edge flow orthogonal and is not satisfactory for analysis of the jet-flap effects. In order to examine the effects of the jet-flap on preventing flow separation, it was necessary to develop a method of estimating the suction surface compressible velocity distribution downstream of the trailing edge flow orthogonal. The velocity distribution for the blade with and without the jet-flap was developed using the incompressible, two-dimensional relaxation procedure which satisfies Laplace's equation. These data for the hub, mean, and tip are shown in Figures 52, 53, and 54, respectively. In the region of the flow channel where compressible and incompressible solutions were available, a velocity correction factor equal to the ratio of incompressible to compressible surface velocity was constructed as a function of the corresponding compressible critical velocity ratio (W/W_{cr}) at the hub, mean, and tip. At a given position downstream of the trailing edge flow orthogonal, the incompressible velocity was multiplied by the correction factor to produce a pseudocompressible critical velocity ratio. This compressible velocity distribution was then used to analyze the boundary layer characteristics in the presence of the jet-flap. The compressible velocity distribution is shown in Figures 55, 56, and 57. The resulting incompressible boundary layer shape factor (Hi) at the hub, mean, and tip for the blade with the jet-flap is shown in Figure 58. No separation up to the trailing edge was indicated.

Alternate Slot Widths

The internal configurations and the external airfoil shapes of the jet-flap rotor-blade are shown in Figures 39, 40, and 41. The trailing edge thickness is 0.100 inches, and the blade wall thickness is 0.030 inches in the trailing edge portion. This geometry results in a minimum passage width of 0.040 inches at the extreme trailing edge. To prevent choking within the blade passage, the maximum jet slot width is limited to 0.040 inches.

An examination of Figure 36 illustrates that if the jet momentum is maintained constant and the slot width varied from 0.015 inches to 0.040 inches, the range of secondary flow varies from four percent to six percent. This range spans the design value of five percent at a slot width of 0.026 inches and will permit an evaluation of the losses associated with mixing the jet and main streams at various energy levels. The design and alternate slot widths are:

	Alternate No. 1	Design	Alternate No. 2
Slot width, inches	0.015	0.026	0.040
Flow, percent	4	5	6

MECHANICAL DESIGN AND STRESS ANALYSIS

The mechanical design, general arrangement, and overall layout of the test rig is shown in Figure 59. The inner and outer cases were formed from heavy wall forgings which also serve as suitable mounting surfaces for instrumentation. The outer case was in two pieces, forming the front and rear bearing supports. The front bearing support consisted of four struts to which the inner flow path forging was attached. These inner and outer flow path structures also served as the mounting structure for the stators. The stators were mounted with the stacking axis passing through pivots to allow for adjustment in vane setting angle. The rear support consisted of a six-strut structure mounting the inner flow path and bearing housing. The front support was mounted to an adapter section which connected the turbine rig flow path to the existing test stand plenum. This adapter section included six large hollow struts, five of which fed the secondary air to the rig. The secondary air passed down through the struts to an annular duct which separated the primary air supply and the coupling drive shaft. The secondary air passed through this annular duct and through the eleven large holes in the front support shown in section EE of Figure 59, Sheet 2. From this point, the secondary air passed into the area between the front support inner flow path and the rotor shaft where it was finally picked up by the rotor at a low diameter. The rotor was of split wheel construction to facilitate easy changing of the rotor-blades and still permit the efficient induction of the secondary air. The splitline in the outer case just forward of section line BB of Figure 59, Sheet 1, permitted the removal of the rear support and rotor assembly on the test stand without removal of the front support and its associated instrumentation. The rig incorporated a monorail roller system whereby the entire rear support and rotor assembly could be rolled aft, free of the front support. Both bearing supports had vibrational pickups mounted on the bearing housings. A whip pickup was mounted over the rotor-blade tip.

The stress analysis of the test rig was based on nominal rig inlet conditions of 700°R and three atmospheres of pressure. These inlet conditions were not the maximum available from the test facility, but they do represent the general level at which most testing was conducted. Inlet pressures much greater than three atmospheres can cause excessive bearing thrust loads if the secondary air pressure also approaches turbine inlet pressure. This is discussed in more detail under Rotor Assembly Thrust Loading. Design rotational speed at the 700°R inlet temperature was approximately 5400 rpm. The stresses in all rotating parts were examined at rotative speeds up to 140 percent of design speed.

STATOR

The stator vanes were individual castings of Inco 713LC material. The calculated maximum bending stress in the airfoil section at design operation

was 1619 psi. The maximum bending and shear stresses in the mounting pivots were 7275 and 2040 psi, respectively. The distribution of bending stress in the vane is illustrated in Figure 60a, and the calculated stress characteristics are summarized in Table XI. Figure 60b also shows the calculated natural frequency of the vane at 1075 cps which corresponds to 12th rig rotational order at the design rotational speed.

PLAIN ROTOR-BLADE

The summary of the plain rotor-blade calculated stress characteristics is presented in Table XII. Plots of the blade bending and centrifugal stress at 100 and 110 percent design rotational speed are shown in Figures 61 and 62. The calculated natural frequency of the blade was 993 cps which approximately matches the 11th rotational rig order at design speed. These data are shown in Figure 63. The blade was investment cast in Inco 713LC material.

VORTEX GENERATORS

The triangular plow vortex generator will be applied to the plain rotor-blade on completion of the plain blade testing. The plows will be cast from Epon 828 plastic and will be fastened to the plain rotor-blade by Dow Epoxy plastic glue. This plastic cement has a shear bond strength of 2000 psi while the shear stress in the joint due to the centrifugal field is only 13 psi.

The plows will be burned off of the plain blade following their test by placement in a 600°F oven. The co-rotating vane type vortex generator will be applied to the plain airfoil by low temperature brazing of 0.015-inch stock into slots which are gang eloxed into the blade. Vane height is trimmed by a fixture bolting operation. The cantilever of the vane from the blade surface produces an 1800-psi bending stress in the tip vane due to the centrifugal field.

TANGENTIAL SLOT BLOWING BLADE

A summary of the calculated stress characteristics of the tangential slot blowing blade at design condition is shown in Table XIII. The radial distribution of centrifugal and bending stress is shown in Figure 64 at design rotational speed. Figure 65 illustrates the calculated natural frequency as a function of rotational speed, indicating approximately 12th order operation at design speed.

TANDEM BLADE

The relative position of the primary and secondary airfoil sections for the tandem blade was dictated by aerodynamic requirements. Therefore, it was virtually impossible to maintain the relative section positions at all radii

and simultaneously maintain the center of gravity of each airfoil section on a radial line. Therefore, the airfoils were stacked as shown in Figure 66. It is obvious from Figure 66 that the two airfoil tips will tend to close from centrifugal force. Therefore, mechanical spacers or "bumpers" were incorporated at the tip. The bumper was cut to eliminate an excessively high shear stress which would develop due to differential radial growth in the two airfoils in the centrifugal field. The bumpers, integrally cast with the airfoil, will have an initial gap of 0.010 in. This gap closes at 40 percent of design speed due to the centrifugal field. The bumper force developed at design speed is 30 pounds which results in a compressor stress in the bumper of 4000 psi. The bumper centrifugal bending stress is 34,000 psi, and the maximum combined tensile stress is 30,000 psi. A summary of the stresses at the hub section and the radial station where the combined stresses are a maximum is given in Table XIV. The first bending mode natural frequencies of the airfoils are shown in Figure 67.

JET-FLAP BLADE

The airfoil sections of the jet-flap blades were stacked on the center of the trailing edge circle rather than the center of gravity of each airfoil section. This procedure was followed to permit ease of cutting the jet-flap slot with only a small increase in blade bending stress due to the offset of the center of gravity. A summary of the calculated blade stress characteristics is shown in Table XV. The fundamental frequency of the airfoil was calculated to be above 9th engine order at the design speed of 5400 rpm. The natural frequency characteristics are shown in Figure 68.

RIG ASSEMBLY WEIGHT AND CENTER OF GRAVITY

The weight of the entire rig was broken into three components.

	Weight—pounds
Front support	1086
Rear support	514
Rotor	977
Total	2577

A schematic of the rig with the associated locations of center of gravity is shown in Figure 69.

WHEEL ASSEMBLY

The wheel assembly was of split-ring construction and was fabricated from forgings of AMS-5621 material. The stress characteristics of the rotor wheel, the blade attachment ring, and the blade attachment lugs in the

wheel rim are presented in Table XVI. These data illustrate that at all speeds investigated, stress margins were well within acceptable limits. The radial variation of the tangential and radial stresses in the ring and wheel is shown in Figures 70 and 71, respectively.

The calculated critical frequency of the rotor system is presented as a function of the rotor speed and the spring rate of the bearing supports in Figure 72. It was assumed in this calculation that both front and rear spring rates were the same. The calculated spring rate of the rear support was 9.95×10^5 pounds/inch. It is estimated that the front support spring rate will also be of this magnitude resulting in a rotor critical speed of 10,000 rpm or 185 percent of design speed. It also should be noted that the magnitude of the front support spring rate, within reasonable values, has a relatively small effect on the rotor critical speed because of its large relative distance from the rotor CG when compared to the close proximity of the rear support bearing to the rotor CG.

ROTOR ASSEMBLY THRUST LOADING

The thrust loads of the rotor assembly are primarily a function of the turbine inlet pressure, secondary air inlet pressure, and the rotor equivalent speed. The rotor inlet and exit hub static pressures and the thrust loading of the blades were calculated from a turbine off-design performance prediction calculation. The thrust load resulting from the pressure differential across the wheel was calculated for a range of secondary air inlet pressures. The variation of total rotor thrust with turbine expansion ratio (P_{T_0}/P_{T_6}) was calculated for a range of equivalent speeds. These calculations were made for constant values of turbine inlet and secondary air pressures. The results of these calculations for the case when the turbine inlet and secondary air pressures both equal 3.36 atmospheres are illustrated in Figure 73. A test restraint is that the secondary air pressure cannot exceed the turbine inlet pressure. Therefore, the results presented in Figure 73 should represent the maximum thrust loading condition to be expected using secondary air at 3.36 atmospheres pressure.

Thrust loads were also calculated for the configurations using no secondary air. In these applications, the secondary air cavity pressure is expected to equal stator hub static pressure. The results of this calculation are presented in Figure 74 for 70 and 110 percent equivalent speed.

Basing the thrust capacity of the bearing on 1000 hours of SKF L10 life results in a 3750-pound capacity at 6000 rpm. Restricting the thrust loading of this magnitude permits construction of permissible operating envelopes in terms of turbine inlet pressure and secondary air pressure. The turbine

total to static expansion ratio (P_{T_0}/P_{st_6}) required to achieve limiting loading is expected to be approximately 3.36. If a secondary air pressure equal to turbine inlet is also required, the data of Figure 73 indicate excessive thrust loading. Therefore, the turbine inlet pressure will be reduced to maintain the thrust limit, and the exhaust system will be reduced below ambient pressure by the vacuum facility to achieve the required expansion ratio.

INSTRUMENTATION

The overall turbine performance instrumentation plan consists of the details of measuring the following:

Turbine inlet	Turbine exit
Total temperature	Total temperature
Total pressure	Total pressure
Static pressure—hub and tip	Static pressure—hub and tip
	Gas flow angle

Overall

Airflow rate—primary and secondary
Dynamometer torque
Rotational speed

By measuring these variables, all aspects of overall performance may be obtained.

AIRFLOW MEASURING SYSTEM

The schematic of the air supply system and the associated measurement equipment are shown in Figure 75. The primary airflow (turbine stator inlet airflow) is the measured airflow at the Bailey adjustable orifice minus the secondary airflow measured by the thin-plate orifice in the 8-inch diameter line.

Primary Airflow

The Bailey adjustable orifice (Bailey Meter Co. JA6 Series OFAS) is mounted in a 42-inch diameter pipe. The orifice upstream static pressure is measured by two separate taps and recorded manually from vertical mercury manometers and automatically on the Fischer-Porter data acquisition system. The differential pressure across the variable orifice is manually recorded from a vertical water manometer. Three thermocouples upstream of the orifice are recorded manually from Brown Indicators and by the SEL (Systems Engineering Laboratories) data acquisition system. The Bailey instrument is calibrated with a series of ASME flow nozzles installed on the exhaust end of an airflow calibration section which attaches to the inlet plenum. The flow nozzle discharges into the test cell. The Bailey instrument is normally calibrated with air at 300°F. The effect of air temperature on the orifice calibration is established experimentally and is applied to the calibration curve.

Prior to calibration, an inlet air piping leakage rate is determined as stated in the following text. Experience has shown this to be negligible (0.04 percent of design flow). Leakage check procedure is as follows:

1. Install blank-off plate on either the inlet plenum or calibration rig discharge

2. Install a shop air supply through a flow measuring tube to the permanent secondary air supply line discharge port

3. Increase piping internal pressure to 60 inches Hg absolute by supply from air facilities

4. Close facility air valves upstream of Bailey meter and maintain pressure on both sides of these valves approximately equal

5. Supply and measure shop air to regulate the piping internal pressure at the desired level

Secondary Airflow

The secondary air thin-plate orifice is fabricated and installed to meet ASME requirements. The orifice is located approximately 20 diameters downstream of the 90° turn and 13 diameters upstream of the control valve. The flow is measured using flange taps by recording upstream reference pressure, differential pressure, and upstream temperature. These parameters are recorded as stated for the Bailey meter except that the differential pressure is normally recorded using a vertical mercury manometer.

TORQUE MEASUREMENT SYSTEM

The turbine power is absorbed by two Dynamatic dry-gap eddy current brakes. These dynamometers can be coupled in series as required by load. The maximum load is limited by the cooling water skin temperature. For continuous, longtime operation, this limitation is approximately 4000 horsepower. The turbine maximum output is estimated to be 6360 horsepower with inlet pressure of 45 psia and temperature of 700°R. Thus, it is necessary to utilize both dynamometers for the higher power levels. One dynamometer operation will be used for the lower torque and horsepower levels, thus maintaining accuracy well within the required limits. However, this precludes running continuous speed lines over the complete pressure ratio range.

The torque is measured separately for each dynamometer by a Baldwin dual output strain gage load cell (0 to 1000 pounds) connected in tension to a torque arm attached to the cradled dynamometer stators. The effective

lever arm from the dynamometer centerline is 4 feet. One output of each load cell is displayed on a visual meter. The other output is recorded by the SEL data acquisition system. The load cell system is calibrated as-installed utilizing a torque arm-basket attached to the opposite side of the dynamometer. These items remain in place during testing and serve as a portion of the tare load on the load cells. The load cells are zeroed and calibrated while rotating the dynamometer rotor by hand at a low speed. This is considered necessary to remove the effects of bearing friction between the dynamometer rotor and stators. The dynamometers are calibrated with the dynamometer in the "test" configuration. That is, the dynamometer(s) is coupled to the gearbox (and together, if more than one is required). The oil and cooling water systems are maintained at near operating conditions. Both the visual meter and SEL system torque load cell output values are calibrated. Previously demonstrated manual reading repeatability of the static calibrations over a longtime period has been ± 2.5 foot-pounds. This is approximately 0.05 percent of design torque.

The SEL system accuracy (± 4 pounds) previously submitted was for the worst situation based on specified instrument accuracies without a static calibration. Periodic calibration will decrease this value.

In addition to the preceding, the gearbox loss affects the turbine torque reading. The bearing loss for the configuration to be used during testing is approximately 42 horsepower at 5250 rpm. This loss is measured during testing by measuring gearbox heat rejection rate. The scatter of heat rejection measurements is approximately ± 3 horsepower at 5250 rpm which is 0.065 percent of the design power.

ROTATIONAL SPEED MEASUREMENT

Turbine speed indication is accomplished through the use of a Beckman-Berkeley electronic tachometer system and is designed to give a digital presentation of turbine speed, in rpm, at the operator control panel. Basic accuracy of the system is ± one count of indicated rpm.

TURBINE INLET INSTRUMENTATION

The axial and circumferential location of the turbine inlet instrumentation is shown in the side view and section EE of Figure 59, Sheet 2. Figure 76 shows the inlet total pressure probe and Figure 77, the inlet temperature rake. Inlet total pressure is measured by four Kiel-type total pressure probes located 90° apart. The sensing element is located radially at the midarea point of the annulus. These probes are used to check on the inlet uniformity of the flow. The inlet total pressure is calculated based on continuity using the measured flow rate, annulus area, measured total temperature, and the average of the inlet hub and tip static pressures. Four static

taps are installed at the hub and tip, 90° removed, and out of range of the inlet total temperature rakes or pressure probes. Inlet total temperature is measured independent of the fixed rakes with five iron-constantine thermocouples per rake. Each element is located on the area center of five equal annular areas.

The secondary air inlet total temperature and pressure probe is shown in Figure 77 for measurements at station I.

TURBINE EXIT INSTRUMENTATION

The axial and circumferential location of the exit instrumentation is shown in the side view and section BB of Figure 59, Sheet 1. The turbine outlet instrumentation consisted of hub and tip static pressure taps and five combination total temperature, pressure, and absolute flow angle self-aligning probes. A picture of one of these combination probes is shown in Figure 78. The sensing elements of the five combination probes were located at the centers of five equal annular areas. The four hub and tip static taps were circumferentially positioned to minimize interference effects from the combination probes and also to investigate the possible effect of interference from the six struts downstream. Therefore, one pair of taps is located directly in line with the struts; one pair, directly between their upstream projections; and the other two pairs, equally spaced to either side of the midstream and strut projections.

INNER-STAGE INSTRUMENTATION

The axial and circumferential position of this instrumentation is shown in the side view and section HH of Figure 59, Sheet 3. Provisions are included for a radial and circumferential survey at the static exit. The hub and tip each have four static pressure taps located in the free-stream area downstream of the stator. Each tap is located on an extension of the hub and tip stator section midchannel streamline. The stator exit survey will be conducted with the rotor assembly removed. A "dummy" rotor forms a smooth hub flow path from the stator exit to the rotor exit station. The survey probe only measures total pressure and is aligned to the stator exit mean-line design absolute flow angle.

ROTOR EXIT SURVEY

The location of this instrumentation is shown in the side view and section JJ of Figure 59, Sheet 3. Provisions are included for radial and circumferential surveys at the rotor exit. These surveys use either a total temperature, total pressure, flow angle probe or hot-wire anemometry equipment. Four pairs of static pressure taps are also included very near the plane of the survey. The sensing elements of the survey probes will be 1/8 in. downstream of the rotor trailing edge. The circumferential movement of the probe is 22 degrees. Figure 79 shows the probe used for the rotor exit surveys.

ROTATING STATIC PRESSURE MEASUREMENTS

Surface static pressures at the mean line of the rotating blades are measured by means of a Scanavalve Co. Model 24D3-1 rotating pressure switch located in the aft center position of the rotor-wheel. Pressure measurements are transmitted from the rotating pressure switch to a stationary transducer through a rotating-to-stationary seal. The electrical signal for indexing the rotating pressure switch is transmitted through a slip ring assembly mounted on the downstream end of the rotor-wheel shaft. The location of the instrumented blades on the wheel and the distribution of the pressure taps on the plain, tangential blowing, and jet-flap blades is shown in Figures 80, 81, and 82, respectively. The tandem airfoil rotor-blade is not instrumented.

REFERENCES

1. Miser, J. W., Stewart, W. L., and Whitney, W. J. Analysis of Turbomachine Viscous Losses Affected by Changes in Blade Geometry. NACA. RME56F21, 2 October 1956.

2. Zweifel, O. "Optimum Blade Pitch for Turbomachines with Special Reference to Blades of Great Curvature." The Engineering Digest, Vol 7, No. 11 (November 1946) pp. 358-360. Continued Vol 7, No. 12 (December 1946) pp. 381-383.

3. Wong, R. Y., Monroe, D. E., and Wentucky, W. T. Investigation of Effect of Increased Diffusion of Rotor-Blade Suction-Surface Velocity on Performance of Transonic Turbine. NACA. RME54F03, 24 August 1954.

4. Truckenbrodt, E. A Method of Quadrature for Calculation of the Laminar and Turbulent Boundary Layer in Case of Plane and Rotationally Symmetric Flow. NACA. TM-1379, 1955.

5. Culick, F. E., and Hill, J. A. F. "A Turbulent Analogue of the Stewartson-Illingworth Transformation." Journal of Aeronautical Sciences. Vol 25, pp. 259-262.

6. Lachmann, G. V. Boundary Layer and Flow Control. Great Britain: Pergamon Press, 1961. Part IV, Vol II, pp. 1260-1332.

7. Schubauer, G. B., and Spangenburg, W. G. "Forced Mixing in Boundary Layer." Journal of Fluid Mechanics. Vol 8, pp. 10-32.

8. Peake, D. J. The Use of Air Injection to Prevent Separation of the Turbulent Boundary Layer in Supersonic Flow. NGTE Report No. R256. National Gas Turbine Establishment, November 1963.

9. Higgins, C. C., and Wainwright, T. W. Dynamic Pressure and Thrust Characteristics of Cold Jets Discharging from Several Exhaust Nozzles Designed for VTOL Downwash Supression. NASA.TN D-2263, April 1964.

10. Clark, E. L., and Ordway, D. E. "An Experimental Study of Jet-Flap Compressor Blades." Journal of the Aero/Spaces Sciences. November 1959, pp. 698-702.

11. Kruger, R. A., Marsh, H., and Horlock, J. H. The Performance of a Cascade Fitted with Blown Flap. Ministry of Aviation, Aeronautical Research Council. C.P. No. 526, London: Her Majesty's Stationery Office, 1961.

12. Huppert, M. C., and MacGregor, C. Comparison Between Predicted and Observed Performance of Gas-Turbine Stator Blade Designed for Free Vortex Flow. NACA. TN 1810. Washington: April 1949.

13. Spence, D. A. The Two-Dimensional Jet Flap--An Exact Solution in Closed Form for Small C_J, and an Interpolation Formula up to C_J = 10.0. Royal Aircraft Establishment. Great Britain Report No. AERO 2568, 1956.

APPENDIX A
BLADE SURFACE VELOCITY CALCULATION PROCEDURE

This procedure calculates the blade surface velocity of inviscid flow through both a rotating and nonrotating axial blade row. The procedure satisfies radial equilibrium at the blade midchannel, assuming all radial section midchannel points lie on a radial line. A schematic of the flow model is illustrated in Figure 83. Channel flow theory is used to determine the velocity distribution across the channel at each radial section. Mass flow rate is obtained by numerical integration across the flow orthogonal surface at each axial station. The calculation procedure, as programmed for a digital computer, can be run in either of two modes. Mode 1 iterates on an estimated hub section midchannel velocity to satisfy continuity. Mode 2 calculates what mass flow rate satisfies continuity for a specified hub midchannel velocity. The latter mode is most useful to gain a good insight into the blade shape modifications necessary to obtain a desired velocity distribution. The calculation procedure is restricted to a given axial station and is independent of conditions upstream or downstream of the given axial stations.

METHOD OF CALCULATION

The calculation procedure begins by determining the value of midchannel velocities relative to the blade at the mean and tip $(W_m)_m$ and $(W_m)_t$ which satisfy radial equilibrium for a specified $(W_m)_h$. (Unless otherwise specified, all velocities will be relative to the blade row.) The following equation expresses the relationship between the midchannel velocity at the hub (which has been estimated and is input data) and the midchannel velocity at any other point (Y) along the potential line from hub to tip.

$$(W_m)_Y = \left\{ \exp\left[\int_h^Y a \, dY \right] \right\} \times \left\{ (W_m)_h - \int_h^Y b \exp\left[- \int_h^Y a \, dY \right] dY \right\}$$

where:

$$a = -\frac{1}{r} \sin^2 \psi$$

$$b = 2 \omega \sin \psi$$

The preceding equation assumes isentropic flows, and constant absolute total (or stagnation) enthalpy, neglects the (Y) component of force exerted by the blade on the gas, and assumes that the radial potential lines are radial straight lines perpendicular to the axis of rotation. Since straight radial potential lines are assumed, the calculation is limited to flow paths of little or no divergence.

Next, the velocity at evenly spaced increments across the hub, mean, and tip circumferential potential lines is calculated using the method presented in reference 12. The following equation is used to calculate the velocity at various points across the circumferential potential lines.

$$W = (W_m)_Y \left\{ \exp - \left[\frac{no}{2\ \Delta Rc} \left(Rc^2 - Rc_m^2 \right) \right] \right\}$$

The streamline curvature (Rc) is assumed to vary linearly with (no). The (ΔRc) is the change in (Rc) from the reference point (midchannel) to the point where the velocity (W) is to be calculated. Also,

$$Rc_m = \frac{1}{2} \left(Rc_{ps} + Rc_{ss} \right)$$

By assuming (P_{rel}) and (T_{rel}) constant across a given circumferential potential line, the flow rate per unit area (ρW) can be calculated. The flow rate is determined by integrating (ρW) over the plane defined by the hub, mean, and tip circumferential potential lines. For Mode 1 operation, the calculated flow rate is compared to the desired flow rate. If these two values do not agree within a certain iteration tolerance, $(W_m)_h$ is adjusted and the entire calculation is repeated. For Mode 2, the flow rate check is not made. The calculation is completed at this point; therefore, the resulting output is for the original input estimate of $(W_m)_h$.

APPENDIX B
DETERMINATION OF JET-FLAP CONTOUR

Following the method as given by Spence (reference 13), an expression was derived which describes the geometric characteristics of a jet emanating from the trailing edge of an isolated blade. The analysis is based on thin airfoil theory which replaces the blade with a straight line of one unit chord length. Further, the flow model is restricted to two-dimensional, incompressible, irrotational flow. The downwash of the jet is expressed in terms of the second derivative of the jet vertical coordinate. This expression, which is put in terms of the jet momentum coefficient (Cj) and the jet efflux angle (τ), is then integrated twice to determine the jet stream contour. The result is

$$y(x) = \tau \left[2\left(1 - \frac{1}{\sqrt{x}}\right) + 2 A_0 \left\{ \frac{1 + \tan\left(\frac{1}{2}\cos^{-1}\frac{1}{\sqrt{x}}\right)}{1 - \tan\left(\frac{1}{2}\cos^{-1}\frac{1}{\sqrt{x}}\right)} - \sin\left(\cos^{-1}\frac{1}{\sqrt{x}}\right) \right\} \right.$$

$$+ \sum_{n=1}^{N-1} \frac{A_n}{(4_n^2 - 1)} \left\{ \frac{2}{\sqrt{x}} \sin n\left(2\cos^{-1}\frac{1}{\sqrt{x}}\right) \right.$$

$$\left. \left. - 4_n \sin\left(\cos^{-1}\frac{1}{\sqrt{x}}\right) \cos n\left(2\cos^{-1}\frac{1}{\sqrt{x}}\right) \right\} \right]$$

where

y is the jet deflection at a given value of x

A_n (n = 0, 1, ... N-1) are Fourier coefficients and are functions of the jet momentum coefficient (Cj)

n is the number of terms retained in the truncated Fourier series

An example of the resulting jet contours at various jet momentum coefficients for a jet efflux angle of 60° is shown in Figure 84. The unit of chord length used in Figure 84 was arbitrarily chosen as 1.0 inch. For the analysis of a jet-flap blade, the unit chord length was taken as the straight-line distance from the intersection of the suction surface and trailing edge flow orthogonal to the suction surface trailing edge. The orientation of the linear airfoil was taken as parallel to $(\psi_4)_m$. The jet contour was terminated when the angle of the contour tangency was equal to (β_6).

Table I.
Turbine interstage temperatures and pressures (free-stream) and blade loads.

	Temperatures (°R)			Pressures (psi)		
	T_{st}/θ_{cr}	T_T/θ_{cr}	$T_{T_{(rel)}}/\theta_{cr}$	P_{st}/δ_o	P_T/δ_o	$P_{T_{(rel)}}/\delta_o$
Stator inlet— Station 0						
Hub	513.8	518.7	—	14.213	14.696	—
Mean	513.8	518.7	—	14.213	14.696	—
Tip	513.8	518.7	—	14.213	14.696	—
Stator exit— Station 3						
Hub	391.4	518.7	450.6	5.322	14.255	8.712
Mean	428.2	518.7	457.8	7.286	14.255	9.209
Tip	449.7	518.7	466.4	8.649	14.255	9.828
Rotor exit— Station 7						
Hub	417.1	435.2	450.6	6.020	6.987	7.881
Mean	417.1	435.2	457.8	6.020	6.987	8.330
Tip	417.1	435.2	466.4	6.020	6.987	8.890

	Radians (inches)	F_x (pounds)	F_y (pounds)
Stator— 40 vanes	11.063	15.626	7.313
	12.187	14.771	8.172
	13.313	13.901	8.857
	14.437	13.071	9.408
Rotor— 76 blades	11.063	*-0.696	**-3.849
	12.187	0.520	**-4.301
	13.313	1.744	**-4.662
	14.437	2.946	**-4.952

*Negative in upstream direction
**Negative in direction of rotation

Table II.
Stator-blade section coordinates.

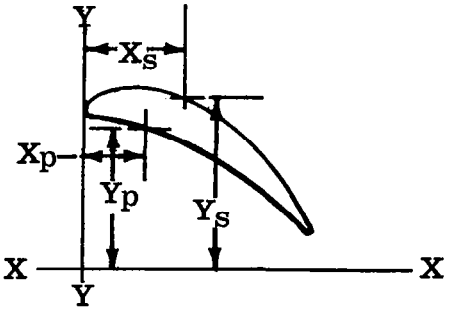

Hub				Mean				Tip			
X_s	Y_s	X_p	Y_p	X_s	Y_s	X_p	Y_p	X_s	Y_s	X_p	Y_p
0	3.000	1.630	0.912	0	3.000	1.848	0.785	0	3.000	2.100	0.638
0.035	3.047	1.605	0.907	0.040	3.053	1.824	0.780	0.045	3.060	2.076	0.632
0.079	3.058	1.563	1.017	0.082	3.063	1.768	0.897	0.088	3.071	2.007	0.757
0.126	3.066	1.518	1.125	0.127	3.071	1.710	1.012	0.134	3.079	1.936	0.881
0.177	3.070	1.472	1.233	0.176	3.076	1.650	1.127	0.183	3.085	1.864	1.003
0.230	3.072	1.424	1.339	0.227	3.078	1.589	1.240	0.234	3.087	1.790	1.124
0.286	3.069	1.374	1.443	0.281	3.076	1.527	1.351	0.289	3.086	1.715	1.243
0.344	3.061	1.322	1.545	0.337	3.071	1.463	1.460	0.345	3.081	1.640	1.359
0.404	3.049	1.270	1.645	0.395	3.060	1.398	1.567	0.404	3.072	1.563	1.473
0.466	3.032	1.215	1.743	0.455	3.046	1.333	1.671	0.465	3.058	1.486	1.584
0.528	3.009	1.160	1.839	0.516	3.026	1.267	1.773	0.527	3.040	1.408	1.692
0.592	2.981	1.103	1.931	0.577	3.001	1.199	1.871	0.590	3.016	1.330	1.798
0.655	2.947	1.046	2.021	0.640	2.971	1.132	1.967	0.653	2.988	1.251	1.899
0.718	2.907	0.987	2.108	0.702	2.935	1.064	2.059	0.717	2.954	1.173	1.997
0.780	2.861	0.928	2.191	0.763	2.894	0.996	2.148	0.781	2.915	1.095	2.092
0.840	2.809	0.868	2.271	0.824	2.847	0.927	2.232	0.844	2.870	1.017	2.182
0.898	2.751	0.808	2.348	0.883	2.794	0.859	2.313	0.905	2.819	0.939	2.268
0.953	2.686	0.747	2.420	0.940	2.735	0.791	2.390	0.966	2.762	0.863	2.350
1.006	2.616	0.687	2.489	0.994	2.671	0.723	2.463	1.024	2.700	0.786	2.427
1.054	2.539	0.625	2.554	1.046	2.601	0.656	2.531	1.079	2.632	0.711	2.500
1.097	2.457	0.564	2.614	1.093	2.525	0.590	2.595	1.131	2.558	0.637	2.568
1.136	2.370	0.503	2.670	1.137	2.444	0.524	2.654	1.180	2.479	0.565	2.630
1.206	2.191	0.443	2.722	1.235	2.241	0.459	2.708	1.305	2.255	0.493	2.688
1.274	2.011	0.382	2.769	1.331	2.037	0.395	2.758	1.427	2.029	0.423	2.740
1.339	1.830	0.322	2.812	1.423	1.832	0.332	2.802	1.547	1.802	0.355	2.787
1.402	1.649	0.263	2.850	1.513	1.626	0.270	2.842	1.663	1.573	0.289	2.829
1.462	1.467	0.205	2.883	1.601	1.418	0.210	2.876	1.776	1.343	0.225	2.865
1.520	1.284	0.147	2.911	1.686	1.210	0.152	2.905	1.887	1.111	0.163	2.895
1.576	1.100	0.091	2.934	1.768	1.000	0.095	2.928	1.994	0.878	0.103	2.920
1.629	0.915	0.035	2.952	1.847	0.789	0.040	2.946	2.099	0.643	0.045	2.939
tl = 0.0490 te = 0.0125				tl = 0.0553 te = 0.0125				tl = 0.0630 te = 0.0125			

Table III.
Plain rotor-blade section coordinates.

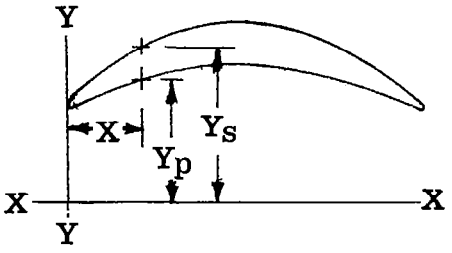

Hub			Mean		Tip	
X	Y_s	Y_p	Y_s	Y_p	Y_s	Y_p
*0.004	0.030	—	—	—	—	—
*0.049	—	-0.006	—	—	—	—
*0.007	—	—	0.594	0.548	—	—
*0.044	—	—	—	—	—	—
*0.014	—	—	—	—	1.084	—
*0.040	—	—	—	—	—	1.030
0.100	0.207	0.043	0.697	0.577	1.136	1.042
0.200	0.366	0.135	0.806	0.623	1.191	1.058
0.300	0.496	0.213	0.904	0.659	1.236	1.069
0.400	0.597	0.280	0.986	0.687	1.268	1.073
0.500	0.684	0.336	1.050	0.710	1.289	1.072
0.600	0.754	0.382	1.099	0.726	1.298	1.065
0.700	0.807	0.418	1.130	0.737	1.300	1.050
0.800	0.845	0.448	1.147	0.742	1.295	1.031
0.900	0.870	0.470	1.148	0.741	1.279	1.005
1.00	0.880	0.487	1.134	0.734	1.251	0.971
1.10	0.873	0.498	1.109	0.723	1.215	0.932
1.20	0.855	0.499	1.074	0.706	1.164	0.887
1.30	0.823	0.493	1.020	0.679	1.098	0.838
1.40	0.774	0.481	0.947	0.644	1.013	0.778
1.50	0.713	0.459	0.865	0.602	0.917	0.704
1.60	0.644	0.433	0.775	0.551	0.810	0.622
1.70	0.568	0.398	0.678	0.494	0.697	0.534
1.80	0.486	0.351	0.578	0.432	0.579	0.440
1.90	0.401	0.297	0.475	0.359	0.456	0.340
2.00	0.316	0.236	0.369	0.281	0.330	0.235
2.10	0.229	0.171	0.261	0.198	0.200	0.129
**2.196	0.144	—	—	—	—	—
**2.175	—	0.120	—	0.134	—	—
**2.197	—	—	0.156	—	0.070	—
**2.174	—	—	—	—	—	0.050

*Points tangent to leading edge radius, leading edge radius = 0.030 inches
**Points tangent to trailing edge radius, trailing edge radius = 0.015 inches

Table IV.
Radial variation of secondary air
total temperature and pressure.

$P_{T_I} = 14.7$ psia $T_{T_I} = 518.7°R$	Hub	Mean	Tip
ur (ft/sec)	427	519	610
$T_{T(rel)_i}$ (°R)	532.43	539.53	548.23
$P_{T(rel)_i}$ (psia)	15.94	16.7	17.69
$\frac{T_{T(rel)_i}}{T_{T_I}}$	1.0265	1.0402	1.0569
$\frac{P_{T(rel)_i}}{P_{T_I}}$	1.084	1.136	1.202

Table V.
Transverse jet growth at throat.

	Hub	Mean	Tip
$\frac{\dot{m}_s}{\ell}\left(\frac{\text{lb}}{\text{sec-in.}}\right)$	0.297	0.305	0.315
y (inches)	0.0303	0.0293	0.0294

Table VI.
Suction surface diffusion factors
for slotted rotor-blade.

	Hub	Mean	Tip
Primary airfoil	0.295	0.157	0.23
Secondary airfoil	0.215	0.305	0.264

Table VII.
Tandem rotor-blade section coordinates.

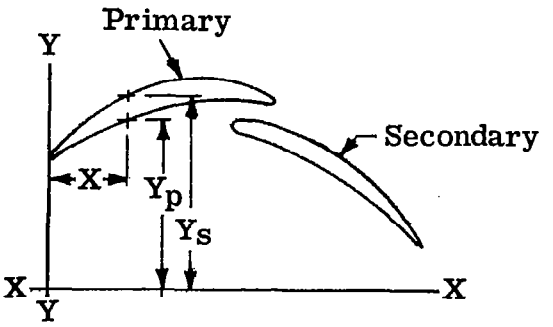

Primary airfoil								
Hub			Mean			Tip		
X	Y_s	Y_p	X	Y_s	Y_p	X	Y_s	Y_p
0	0.196	—	0	0.694	—	0	1.150	—
*0.004	0.212	—	*0.001	*0.703	—	*0.0075	*1.171	—
*0.024	0.244	—	0.026	0.737	—	0.0125	1.177	—
0.047	—	*0.172	*0.038	—	*0.667	*0.0375	1.200	*1.122
0.049	0.282	—	0.051	0.763	0.673	0.0625	1.220	1.128
0.074	0.318	—	0.101	0.812	0.695	0.0875	—	1.133
0.099	0.354	0.217	0.151	0.855	0.718	0.1125	1.252	1.137
0.149	0.423	0.260	0.201	0.896	0.740	0.1375	—	1.141
0.199	0.487	0.303	0.251	0.932	0.763	0.1625	1.278	1.145
0.224	0.517	—	0.301	0.964	0.785	0.1875	—	1.148
0.249	0.545	—	0.351	0.992	0.806	0.2125	1.299	1.152
0.274	—	0.367	0.401	1.016	0.827	0.2625	1.315	1.157
0.299	0.599	—	0.451	1.036	0.847	0.3125	1.327	1.162
0.349	0.647	0.429	0.501	1.053	0.866	0.3625	1.334	1.164
0.374	0.668	—	0.551	1.065	0.885	0.3875	1.336	1.165
0.399	0.689	0.469	0.601	1.075	0.902	0.4125	1.337	1.165
0.449	0.728	0.508	0.626	1.078	0.910	0.4375	1.338	1.165
0.499	0.762	0.546	0.651	1.080	0.918	0.4625	1.337	1.166
0.549	0.793	0.582	0.676	1.082	0.925	0.4875	1.335	1.165
0.599	0.819	0.616	0.701	1.083	0.933	0.5125	1.333	1.163
0.624	0.832	0.633	0.726	1.083	0.938	0.5375	1.330	1.162
0.649	0.842	0.648	0.751	1.082	0.944	0.5625	—	1.160
0.674	—	0.663	0.801	1.079	0.954	0.6125	1.313	1.155
0.699	0.858	0.678	0.851	1.072	0.960	0.6625	1.300	1.148
0.749	0.871	0.703	0.876	—	0.962	0.7125	1.282	1.140
0.774	—	0.715	0.901	1.062	0.963	0.7625	1.260	1.130
0.799	0.880	0.725	0.926	—	0.964	0.8125	1.235	1.117
0.824	0.882	0.734	0.951	1.048	0.963	0.8625	1.206	1.104
0.849	0.883	0.741	0.976	—	0.962	0.9125	1.174	1.090
0.899	0.881	0.754	1.001	1.031	0.961	0.9625	1.139	1.075
0.949	—	0.762	1.051	1.011	0.957	0.9875	—	1.066
0.974	—	0.765	1.101	0.987	0.953	1.0125	1.102	1.058
0.999	0.863	0.767	**1.106	—	**0.952	**1.0305	—	**1.051
1.049	—	0.769	**1.114	**0.978	—	1.0375	1.083	—
1.074	—	0.768	1.121	0.966	—	**1.0465	**1.075	—
1.099	0.827	0.766	—	—	—	1.0505	1.064	—
1.149	0.802	0.758	—	—	—	—	—	—
**1.178	—	**0.751	—	—	—	—	—	—
**1.190	**0.781	—	—	—	—	—	—	—
1.197	0.767	—	—	—	—	—	—	—

*Points tangent to leading edge radius, leading edge radius = 0.030 inches
**Points tangent to trailing edge radius, trailing edge radius = 0.015 inches

Table VII. (cont)

Secondary airfoil								
Hub			Mean			Tip		
X	Y_s	Y_p	X	Y_s	Y_p	X	Y_s	Y_p
0.763	0.480	—	*0.698	0.730	—	0.7265	0.915	—
*0.779	*0.507	—	*0.716	*0.757	—	*0.7405	—	*0.889
0.793	—	*0.450	*0.726	0.760	*0.700	*0.7595	*0.945	—
0.799	0.519	—	0.736	—	0.699	0.7625	0.945	0.878
0.849	0.547	0.453	0.751	—	0.699	0.7875	0.940	0.864
0.899	0.569	0.455	0.776	—	0.697	0.8125	0.934	0.849
0.924	—	0.454	0.801	0.773	—	0.8375	0.928	0.833
0.949	0.586	0.453	0.826	—	0.690	0.8625	0.921	0.817
0.999	0.597	0.450	0.851	0.779	0.685	0.8875	—	0.800
1.024	—	0.448	0.876	—	0.680	0.9125	0.907	0.783
1.049	0.603	0.446	0.901	0.782	0.674	0.9375	—	0.766
1.074	0.604	—	0.926	—	0.667	0.9625	0.891	0.749
1.099	0.603	0.439	0.951	0.784	0.660	1.0125	0.873	0.713
1.124	—	0.434	1.001	0.781	0.642	1.0625	0.850	0.675
1.149	0.599	0.428	1.051	0.775	0.625	1.1125	0.821	0.634
1.199	0.590	0.415	1.101	0.764	0.603	1.1625	0.785	0.593
1.224	—	0.408	1.151	0.748	0.580	1.2125	0.743	0.550
1.249	0.577	0.399	1.201	0.727	0.553	1.2625	0.697	0.505
1.274	0.569	—	1.251	0.701	0.525	1.3125	0.648	0.460
1.299	0.559	0.381	1.301	0.668	0.495	1.3625	0.596	0.415
1.324	—	0.371	1.351	0.630	0.462	1.4125	0.541	0.370
1.349	0.537	0.361	1.401	0.587	0.428	1.4625	0.482	0.323
1.399	0.510	0.338	1.451	0.541	0.393	1.5125	0.422	0.274
1.449	0.479	0.314	1.501	0.492	0.356	1.5625	0.359	0.224
1.499	0.447	0.288	1.551	0.442	0.317	1.6125	0.296	0.173
1.549	0.412	0.261	1.601	0.392	0.277	1.6625	0.232	0.122
1.599	0.375	0.233	1.651	0.340	0.241	1.7125	0.167	0.071
1.649	0.336	0.204	1.701	0.287	0.194	1.7625	0.102	0.018
1.699	0.294	0.175	1.751	0.233	0.151	1.8125	0.035	-0.034
1.749	0.252	0.145	1.801	0.180	0.108	1.8375	—	-0.061
1.799	0.208	0.115	1.851	0.125	0.064	1.8625	-0.032	-0.088
1.849	0.164	0.084	1.901	0.070	0.020	**1.8875	-0.066	**-0.115
1.899	0.117	0.054	**1.926	0.043	**-0.003	**1.9105	**-0.095	—
1.949	0.072	0.023	**1.947	**0.020	—	1.9125	-0.105	—
**1.978	—	**0.005	1.951	0.010	—	—	—	—
**1.994	**0.027	—	—	—	—	—	—	—
1.999	0.015	—	—	—	—	—	—	—

*Points tangent to leading edge radius, leading edge radius = 0.030 inches
**Points tangent to trailing edge radius, trailing edge radius = 0.015 inches

Table VIII.
Jet flow properties resulting from P_{T_I} = 10.0 psia.

	Hub	Mean	Tip
T_{T_i} (°R)	532.43	539.53	548.23
P_{T_i} (psia)	10.84	11.36	12.01
V_j' (ft/sec)	1005	1053	1102
V_{j_a} (ft/sec)	976	1020	1070

Table IX.
Jet-flap rotor-blade section coordinates.

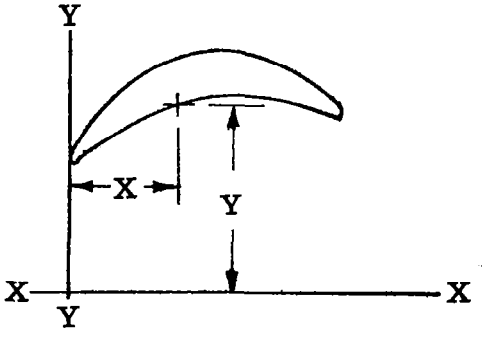

Suction surface				Pressure surface			
	Hub	Mean	Tip		Hub	Mean	Tip
X	Y	Y	Y	X	Y	Y	Y
0	0.0980	0.2818	0.9210	1.9000	0.7093	0.2540	0.3072
*0.0035	0.1132	—	—	**1.8320	0.6628	—	—
*0.0070	—	0.3016	—	**1.8222	—	0.2119	—
*0.0165	—	—	0.9478	**1.8170	—	—	0.2696
0.0500	0.1951	0.3489	0.9641	1.8000	0.6750	0.2267	0.2842
0.1000	0.2798	0.4021	0.9893	1.7500	0.6933	0.2574	0.3257
0.1500	0.3580	0.4532	1.0139	1.7000	0.7097	0.2860	0.3663
0.2000	0.4316	0.5018	1.0375	1.6500	0.7232	0.3120	0.4062
0.3000	0.5634	0.5890	1.0812	1.6000	0.7335	0.3360	0.4453
0.4000	0.6724	0.6618	1.1180	1.5500	0.7412	0.3576	0.4833
0.5000	0.7679	0.7235	1.1476	1.5000	0.7465	0.3770	0.5201
0.6000	0.8466	0.7702	1.1691	1.4500	0.7492	0.3938	0.5560
0.6500	0.8804	0.7891	1.1769	1.4000	0.7499	0.4089	0.5910
0.7000	0.9120	0.8046	1.1820	1.3000	0.7450	0.4343	0.6569
0.7500	0.9407	0.8166	1.1830	1.2000	0.7330	0.4528	0.7152
0.8000	0.9668	0.8260	1.1809	1.1000	0.7157	0.4658	0.7673
0.8500	0.9890	0.8329	1.1761	1.0000	0.6908	0.4737	0.8141
0.9000	1.0079	0.8374	1.1686	0.9000	0.6607	0.4768	0.8540
0.9500	1.0235	0.8387	1.1570	0.8000	0.6239	0.4753	0.8860
1.0000	1.0366	0.8375	1.1421	0.7000	0.5788	0.4660	0.9109
1.0500	1.0478	0.8331	1.1231	0.6000	0.5291	0.4500	0.9287
1.1000	1.0546	0.8257	1.1005	0.5500	0.5008	0.4401	0.9346
1.1500	1.0566	0.8150	1.0746	0.5000	0.4699	0.4290	0.9386
1.2000	1.0559	0.8004	1.0448	0.4500	0.4371	0.4164	0.9403
1.3000	1.0441	0.7582	0.9734	0.4000	0.4023	0.4022	0.9408
1.4000	1.0194	0.7020	0.8870	0.3500	0.3649	0.3859	0.9399
1.5000	0.9817	0.6351	0.7876	0.3000	0.3252	0.3680	0.9369
1.6000	0.9317	0.5524	0.6779	0.2500	0.2822	0.3489	0.9313
1.7000	0.8717	0.4640	0.5632	0.2000	0.2351	0.3281	0.9249
1.8000	0.8063	0.3712	0.4445	0.1500	0.1842	0.3055	0.9173
1.8500	0.7711	0.3235	0.3847	0.1000	0.1303	0.2819	0.9077
**1.8790	0.7503	—	—	*0.0528	0.0779	—	—
**1.8855	—	0.2896	—	*0.0430	—	0.2541	—
**1.8885	—	—	0.3395	*0.0360	—	—	0.8915

*Denotes points of tangency at tl
**Denotes points of tangency at te

Table X.
Comparison of specific work distribution of jet-flap rotor-blade with plain rotor-blade.

Pressure-area (square inches) $\int_0^x \Delta P_{st}\, dx$	Hub	Mean	Tip
Plain blade = A1	14.22	17.64	15.88
Jet-flap blade without jet flap = A2	12.68	16.80	15.90
Jet-flap blade with jet flap = A3	14.34	19.24	18.54
Equivalent specific work between stations 3 and 4 of jet-flap blade without jet-flap from analysis of Appendix A	17.74	17.78	18.22
Equivalent specific work *Method 1	20.10	20.36	21.25
Equivalent specific work **Method 2	20.20	21.82	23.38

$$*\text{Method 1 } (E)_{W/j} = (E)_{\text{Appendix A}} \times \frac{A3}{A2}$$

$$**\text{Method 2 } (E)_{W/j} = 20.0 \times \frac{A3}{A1}$$

Table XI.
Summary of stator-blade stress characteristics.

	Type of stress	Maximum stress (psi)	Allowable stress (psi)	Safety margin
Airfoil	Bending	1619	87,200	58
Mounting pivot	Bending shear	7275 2040	87,200 43,600	11 20.4

Table XII.
Plain rotor-blade stress characteristics
at design point operation.

	Type of stress	Maximum stress (psi)	Allowable stress (psi)	Safety margin
Airfoil	Tensile	12,650	—	—
	Gas bending	4,500	—	—
	Combined	17,150	38.400	2.25
Attachment lug	Tensile	10,300	86,400	7.3
	Shear	11,130	43,200	2.88
	Bending	16,500	86,400	4.23
	Bearing	33,100	86,400	1.6
	Fillet	79,200	—	—
Natural frequency—993 cps Uncoupled torsional frequency—4300 cps				

Table XIII.
Tangential blowing rotor-blade stress characteristics at design point operation.

	Type of stress	Maximum stress (psi)	Allowable stress (psi)	Safety margin
Airfoil	Tensile	13,900	—	—
	Gas bending	6,800	—	—
	Combined	20,700	38,400	1.85
Attachment lug	Tensile	8,700	86,400	8.7
	Shear	9,400	43,200	3.6
	Bending	13,900	86,400	5.2
	Bearing	27,900	86,400	2.1
	Fillet	66,900	—	—

Table XIV.
Tandem airfoil rotor-blade stress characteristics at design point operation.

Airfoil section	Radial station	Centrifugal stress (psi)	Gas bending stress (psi)	Combined bending stress (psi)	Maximum combined bending stress (psi)
Primary	Hub	11,300	10,400 (trailing edge)	4,600 (crown)	15,900 (crown)
Secondary	Hub	13,000	27,300 (leading edge)	4,700 (leading edge)	17,700 (leading edge)
Primary	10.81-inch radius	10,900	9,300 (trailing edge)	6,800 (crown)	17,700 (crown)
Secondary	10.75-inch radius	12,500	25,200 (leading edge)	7,100 (leading edge)	19,600 (leading edge)

Table XV.
Jet-flap rotor-blade stress characteristics at design point operation.

Radial station	Gas bending stress (psi)	Total bending stress (psi)	Hub centrifugal stress (psi)
Hub 10.5-inch radius crown	5700 (compressive)	26,700 (tensile)	13,300 (tensile)
Hub 10.5-inch radius trailing edge	7900 (tensile)	35,900 (compressive)	—

Table XVI.
Summary of wheel assembly stress characteristics.

Type of stress and operating speed		Stress (psi)	Allowable stress (psi)	Safety margin
Wheel	Design point			
	Average Tangential	8,330	80,000	8.7
	Maximum Tangential	11,740	+80,000	5.8
	Radial	14,700	80,000	4.4
	130 percent speed			
	Average Tangential	14,100	100,000	6.1
	Maximum Tangential	19,800	100,000	4.0
	Radial	24,900	100,000	3.0
	140 percent speed			
	Average Tangential	16,300	108,000	5.63
	Maximum Tangential	23,000	108,000	3.7
	Radial	28,000	108,000	2.75
Ring	Design point			
	Average Tangential	31,200	80,000	1.55
	Maximum Tangential	46,150	80,000	0.73
	Radial	13,100	80,000	5.1
	130 percent speed			
	Average Tangential	52,900	100,000	0.9
	Maximum Tangential	77,900	100,000	0.29
	Radial	22,100	100,000	3.5
	140 percent speed			
	Average Tangential	61,000	108,000	0.77
	Maximum Tangential	90,500	108,000	0.20
	Radial	25,700	108,000	3.20
Wheel lug	Design point			
	Bearing	33,150	80,000	1.4
	Shear	12,450	40,000	2.21
	Bending	27,400	80,000	1.93
	Tensile	14,100	80,000	4.7
	130 percent speed			
	Bearing	56,000	100,000	0.79
	Shear	21,000	50,000	1.38
	Bending	46,300	100,000	1.16
	Tensile	23,900	100,000	3.2

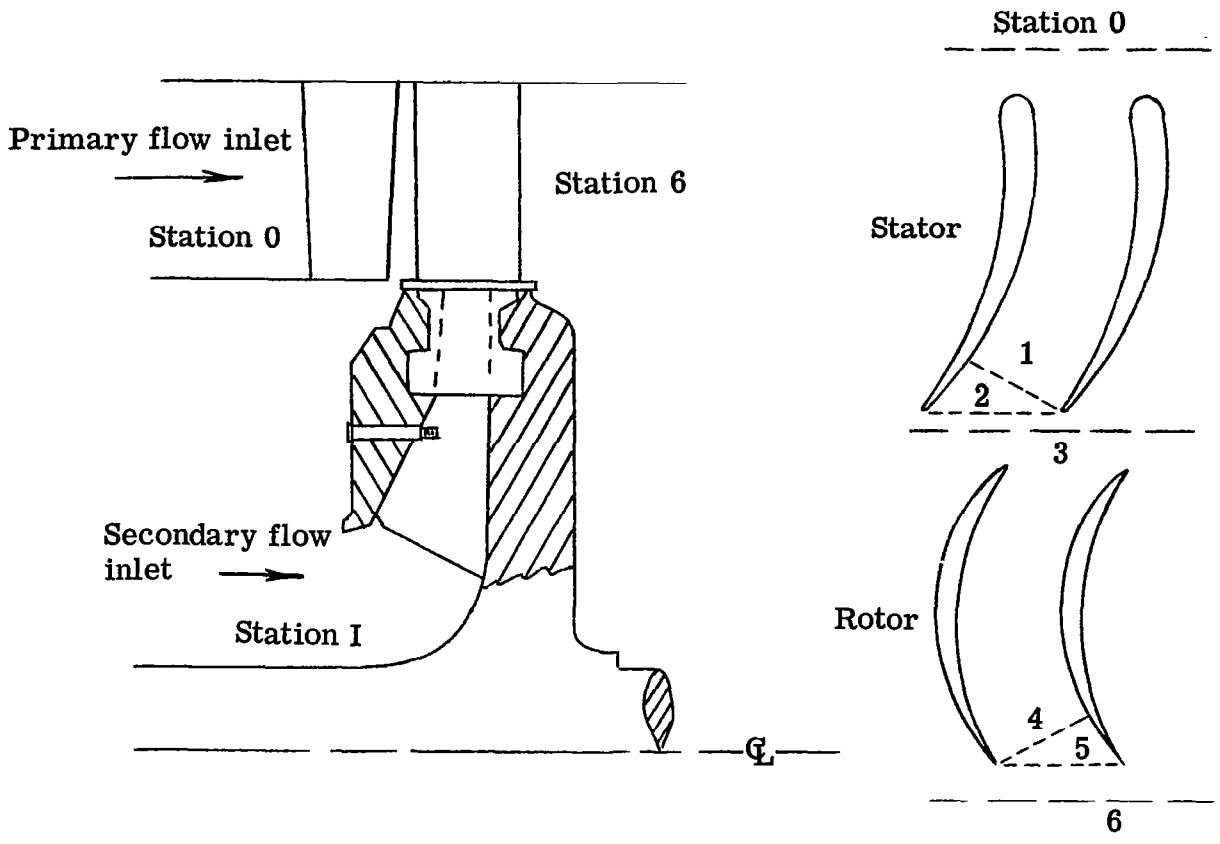

(a) Schematic of flow path

(b) Axial station nomenclature

Figure 1. Station nomenclature and velocity triangles (sheet 1 of 2).

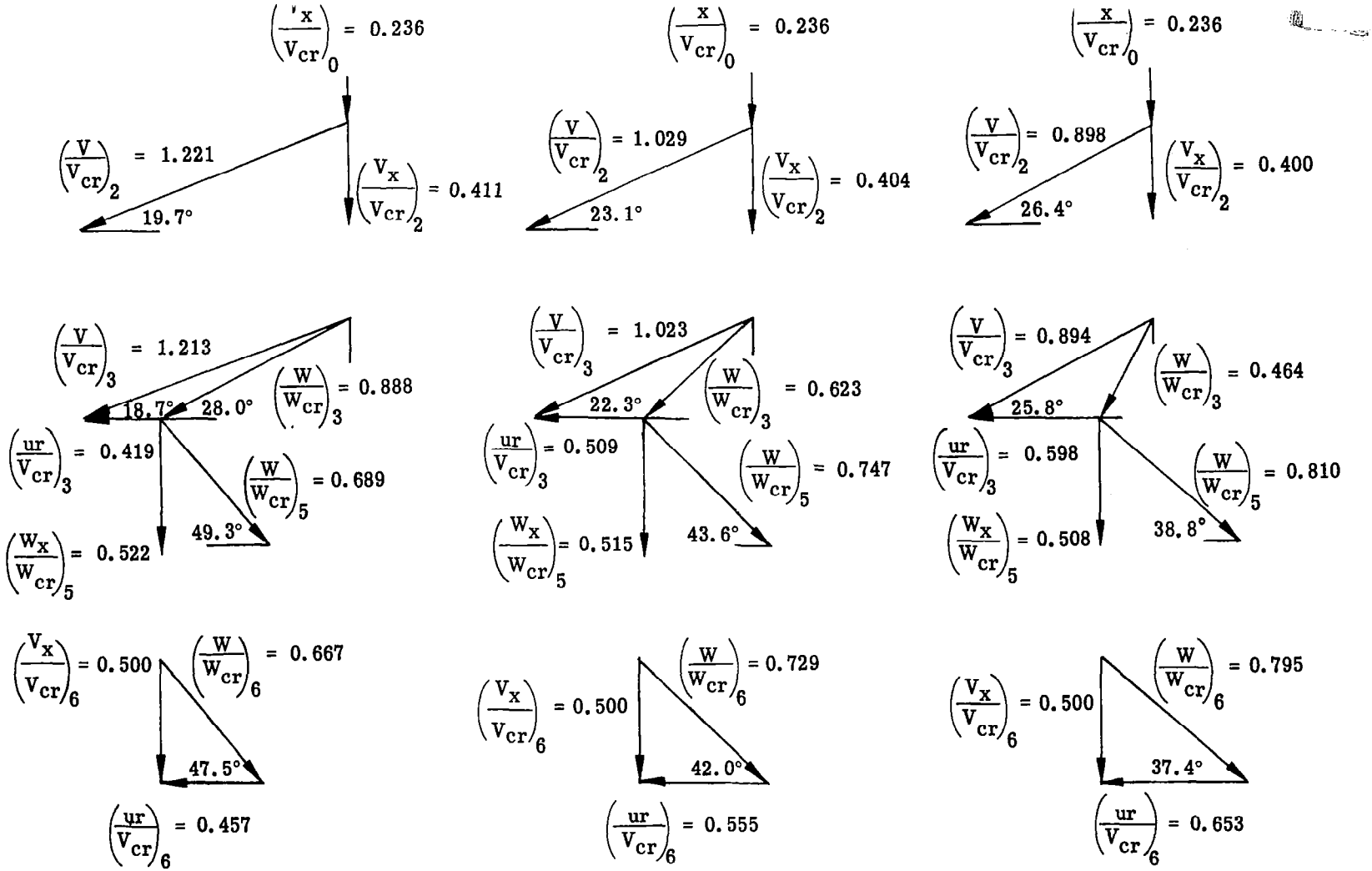

(c) Velocity triangles

Figure 1. Station nomenclature and velocity triangles (sheet 2 of 2).

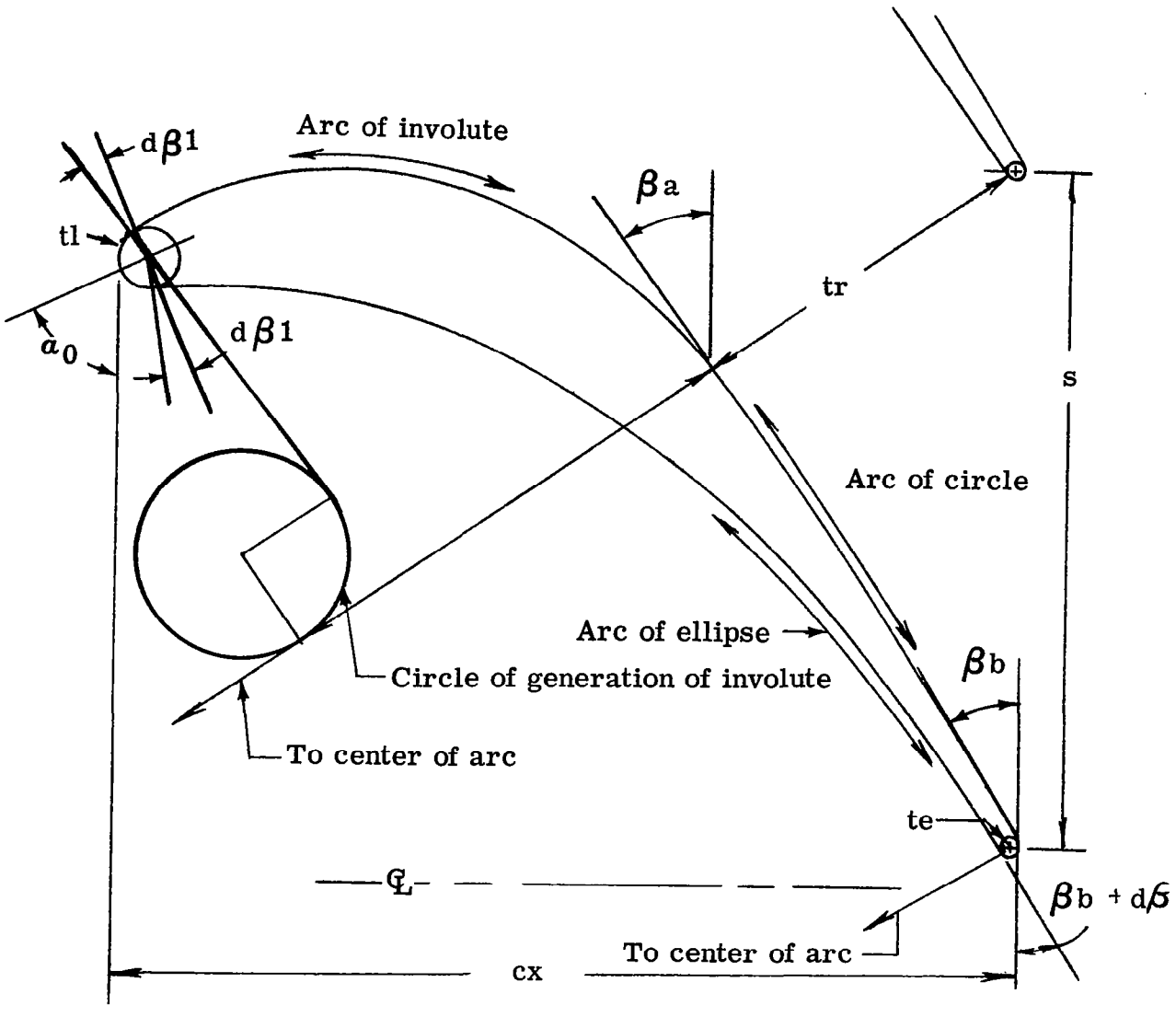

Figure 2. Schematic of stator profile geometry.

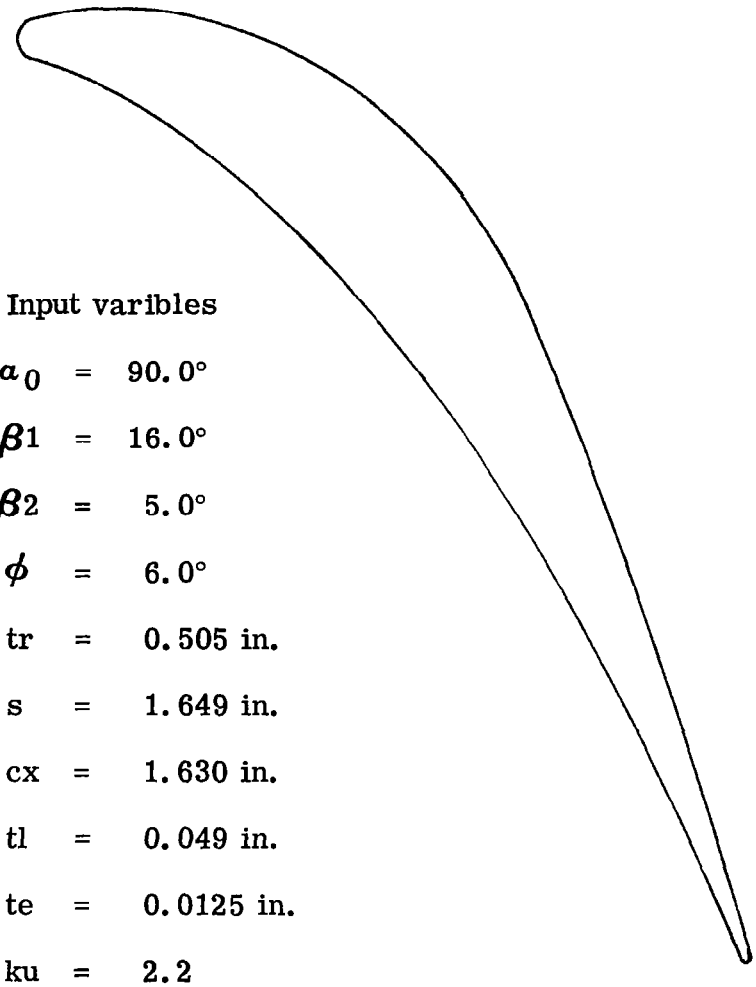

Input varibles

α_0 = 90.0°

dβ1 = 16.0°

dβ2 = 5.0°

ϕ = 6.0°

tr = 0.505 in.

s = 1.649 in.

cx = 1.630 in.

tl = 0.049 in.

te = 0.0125 in.

ku = 2.2

Figure 3. Stator-blade hub section profile.

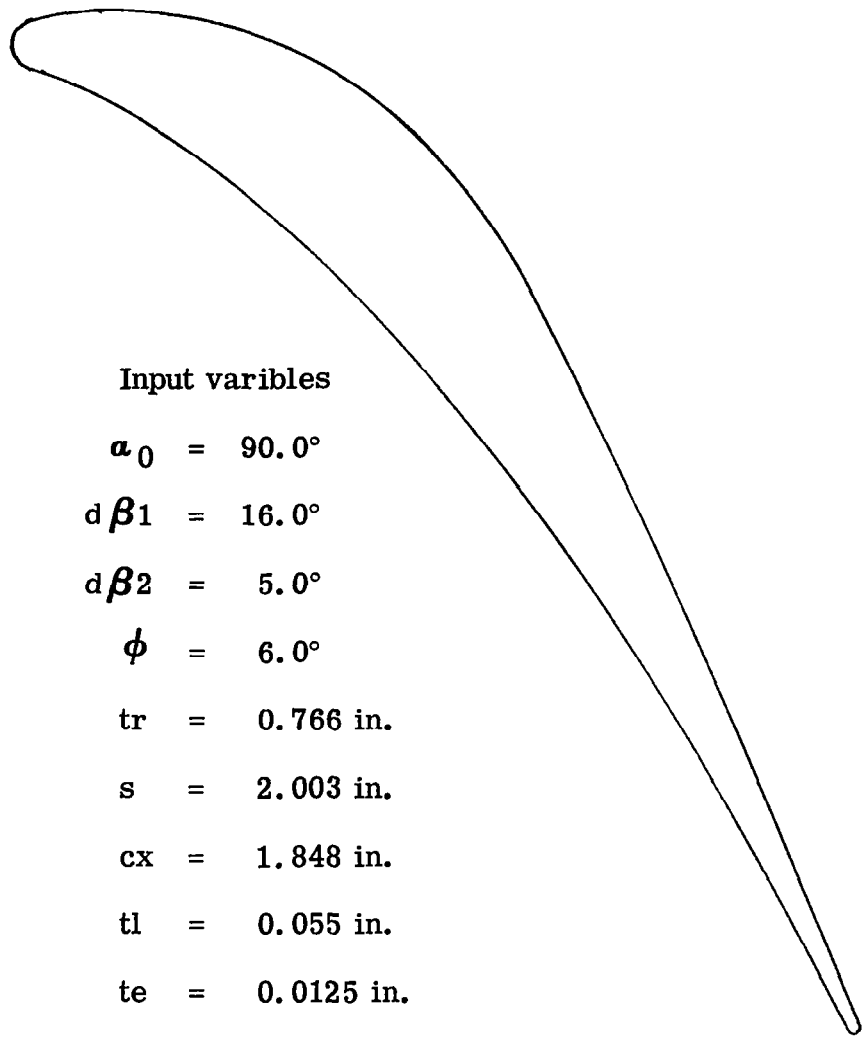

Input varibles

α_0 = 90.0°

$d\beta_1$ = 16.0°

$d\beta_2$ = 5.0°

ϕ = 6.0°

tr = 0.766 in.

s = 2.003 in.

cx = 1.848 in.

tl = 0.055 in.

te = 0.0125 in.

ku = 2.2

Figure 4. Stator-blade mean section profile.

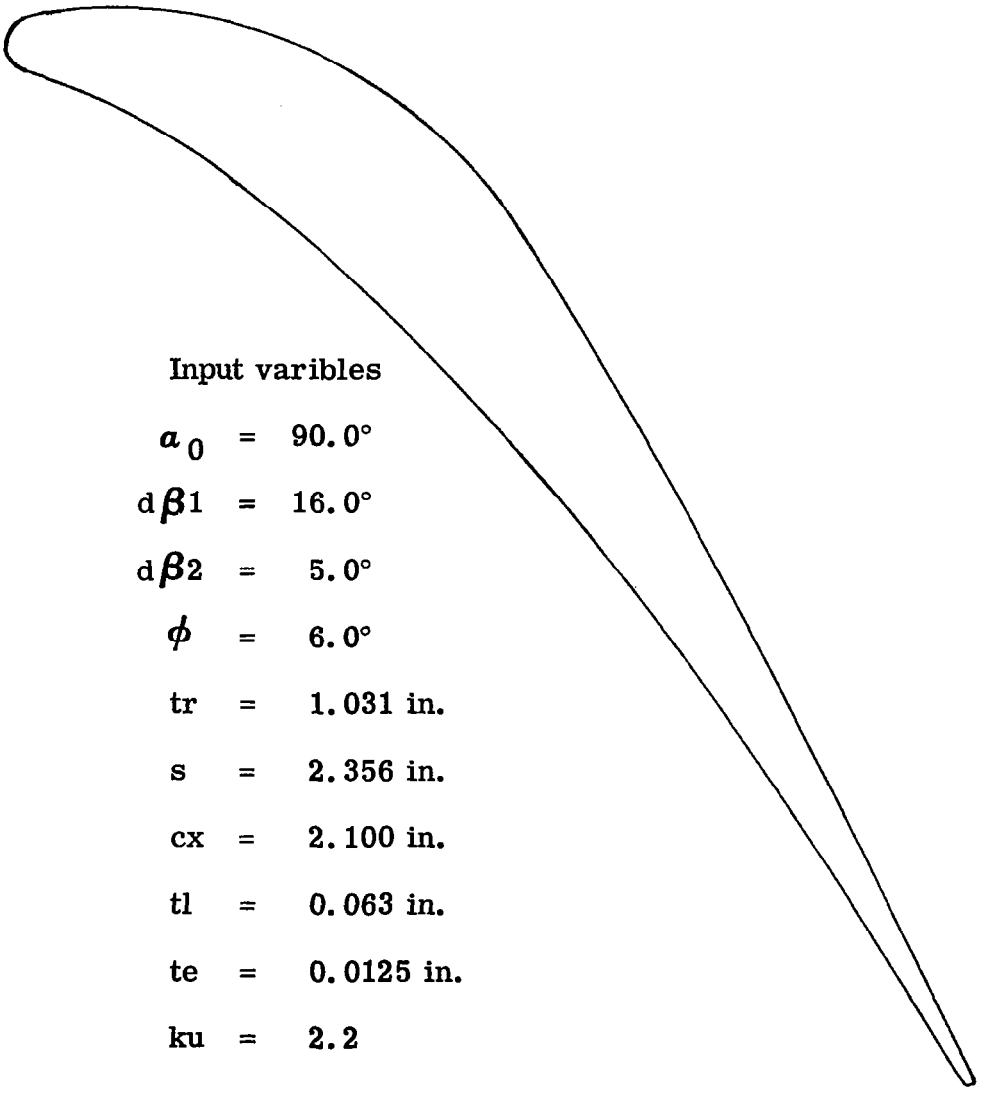

Figure 5. Stator-blade tip section profile.

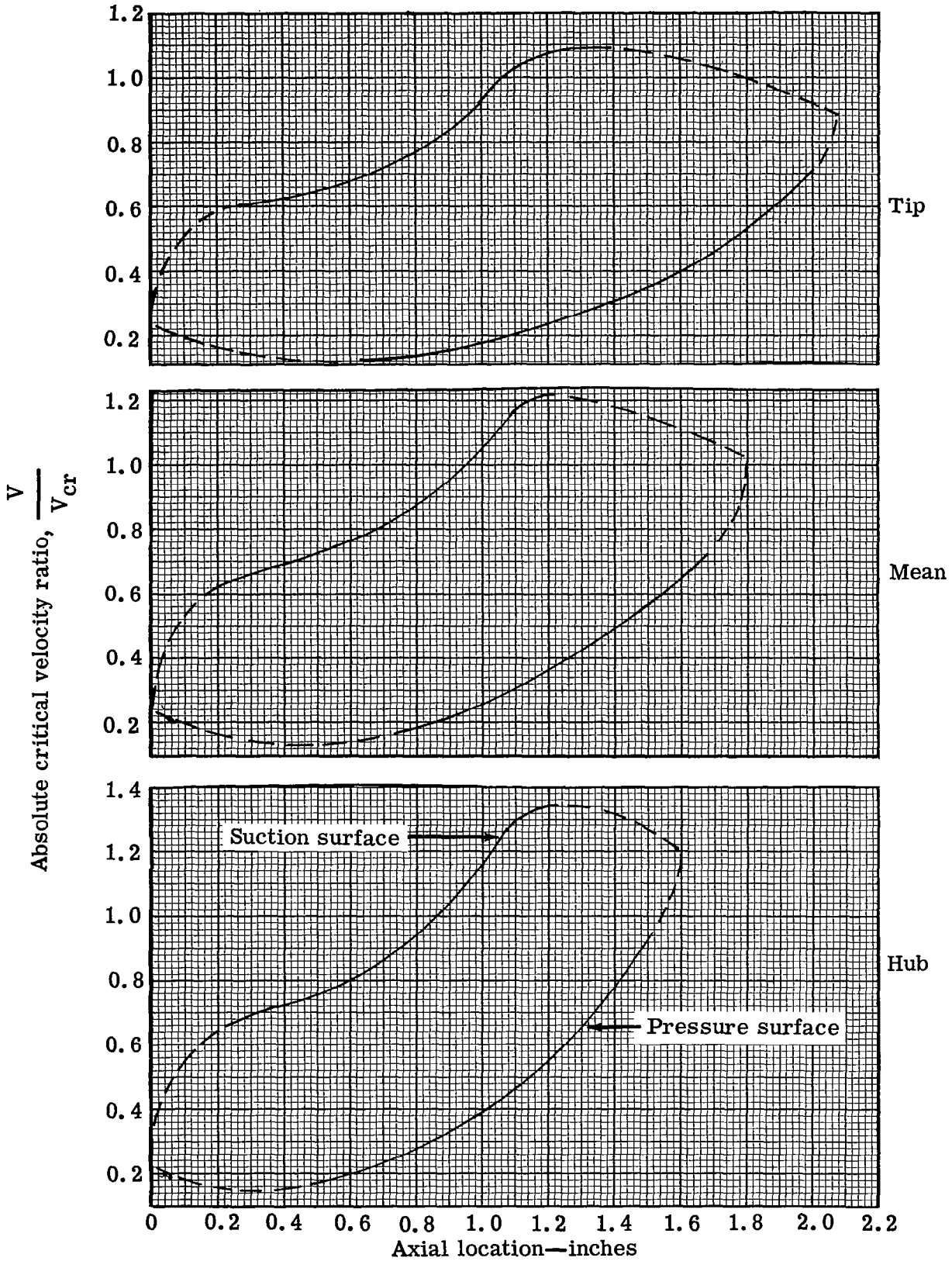

Figure 6. Design stator-blade surface velocity distribution.

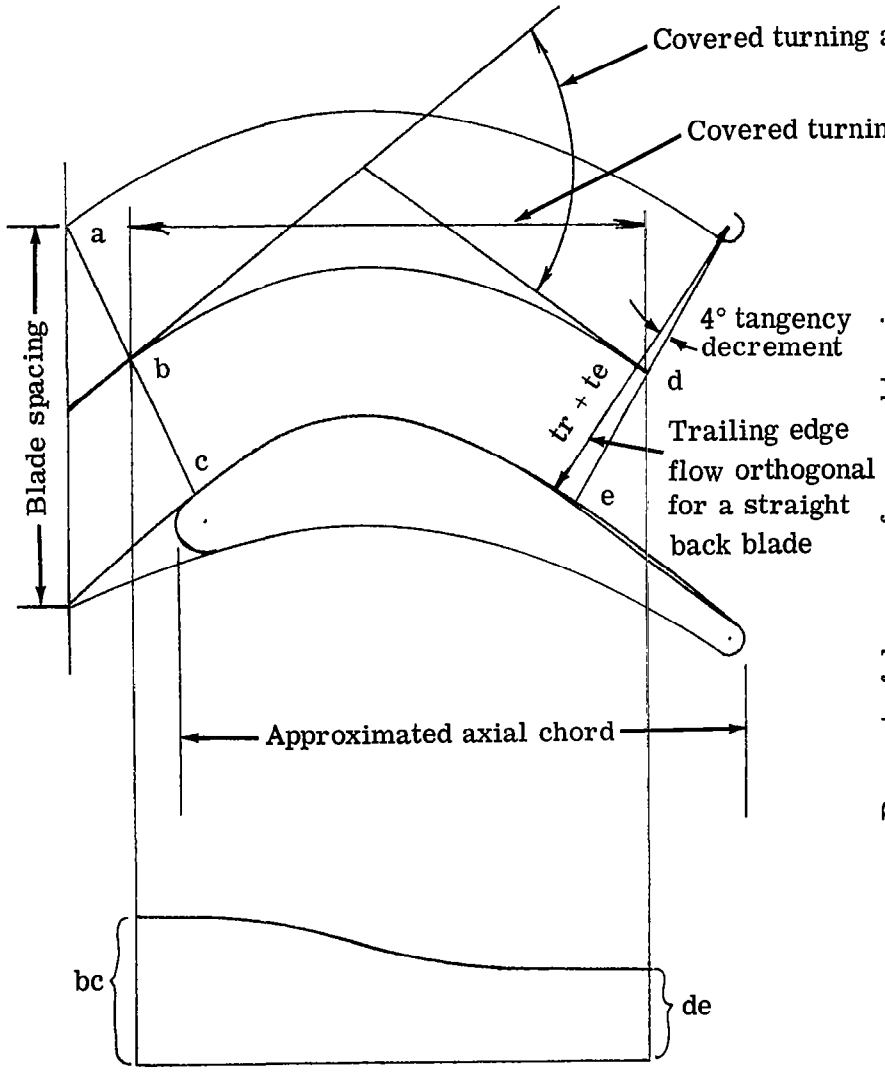

(a) Blade schematic layout

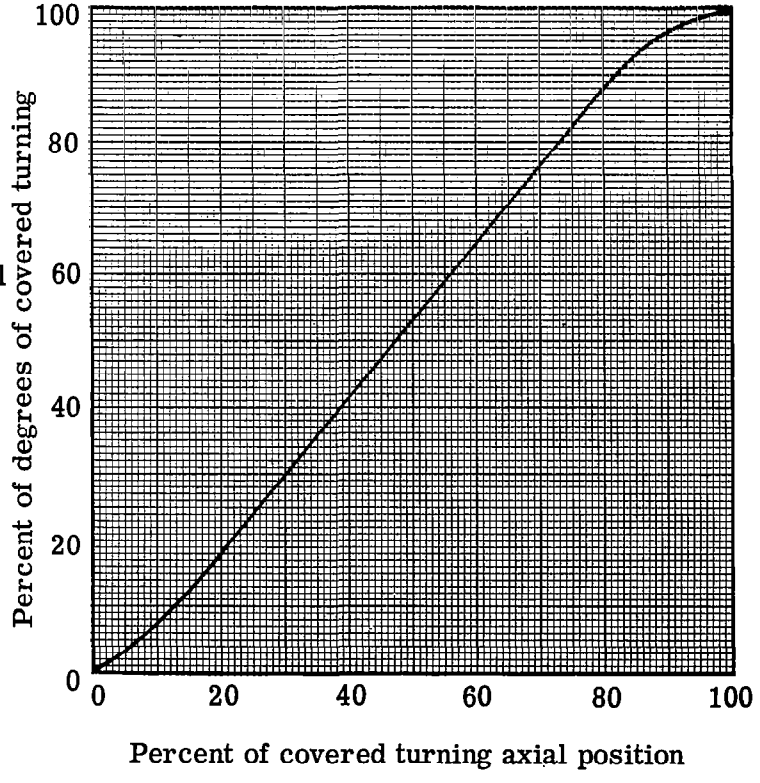

(b) Turning distribution for rotor blades

Figure 7. Blade schematic layout and turning distribution for rotor-blades.

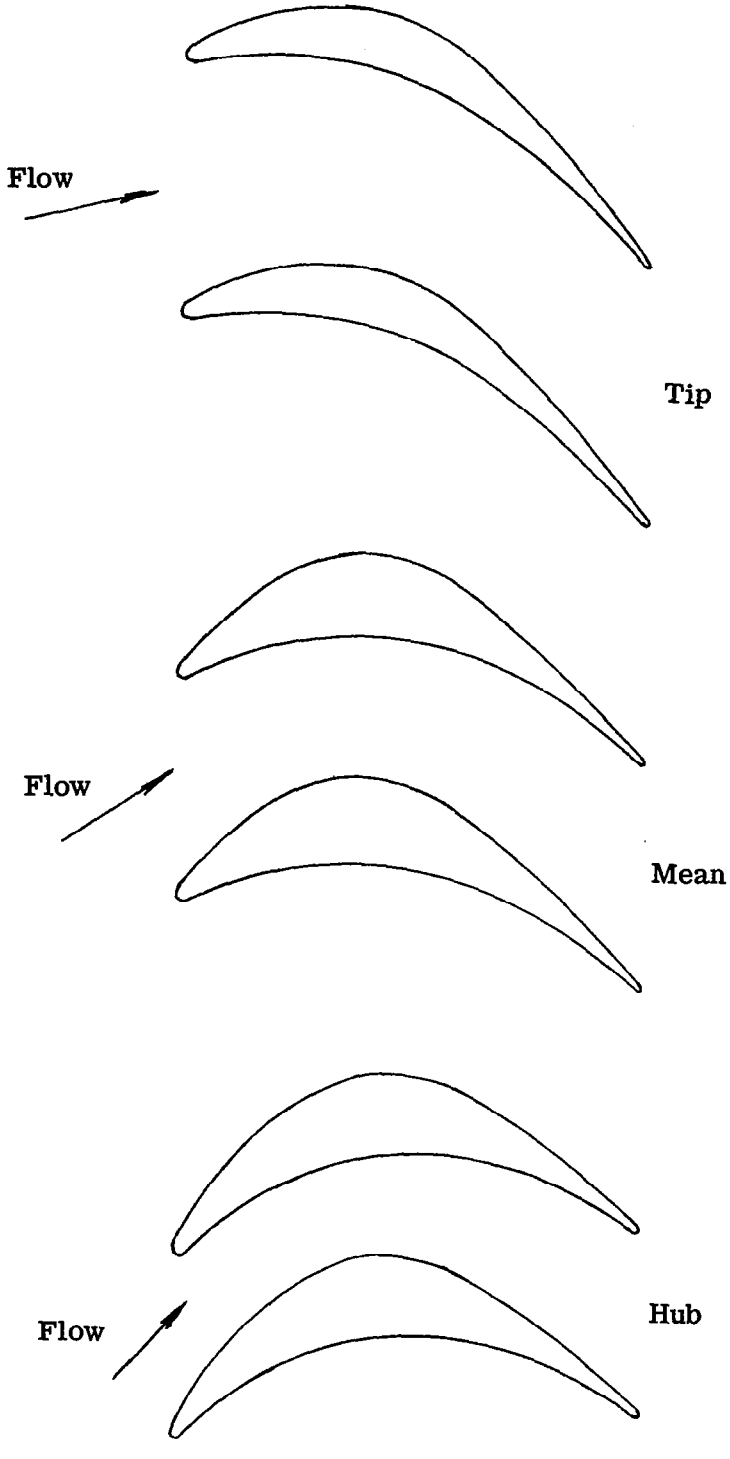

Figure 8. Plain rotor-blade profiles and channels.

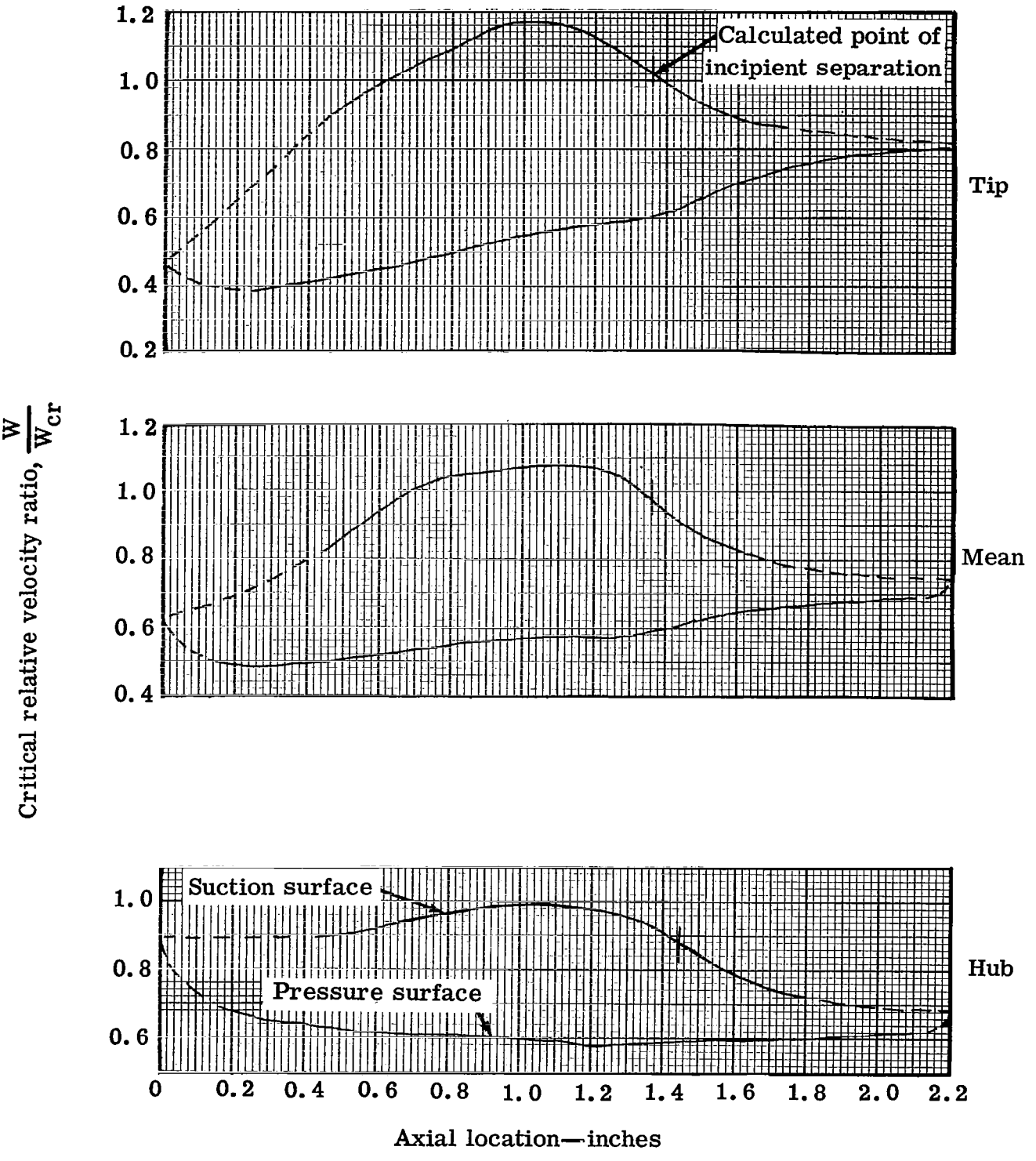

Figure 9. Design plain rotor-blade surface velocity distribution.

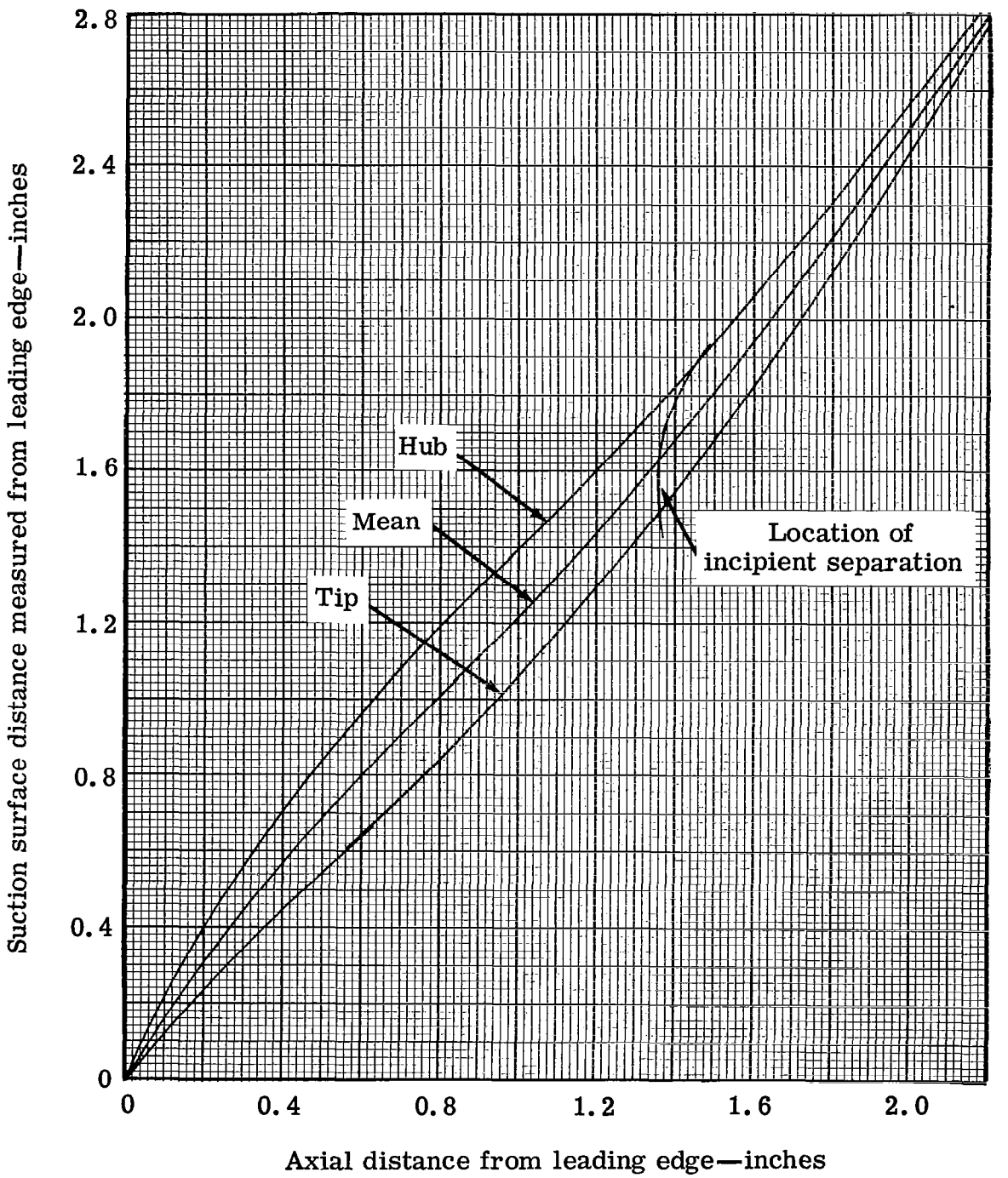

Figure 10. Variation of suction surface length with axial chord for the plain rotor-blade.

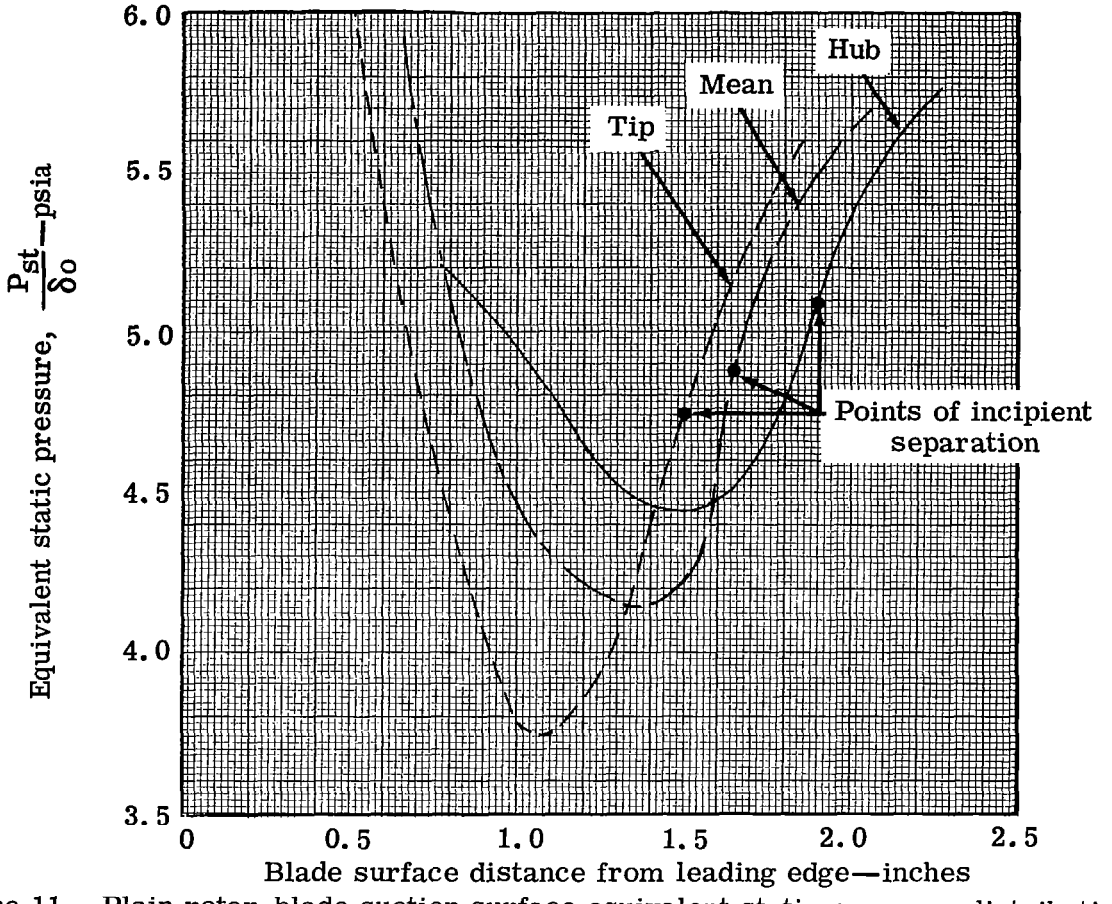

Figure 11. Plain rotor-blade suction surface equivalent static pressure distribution.

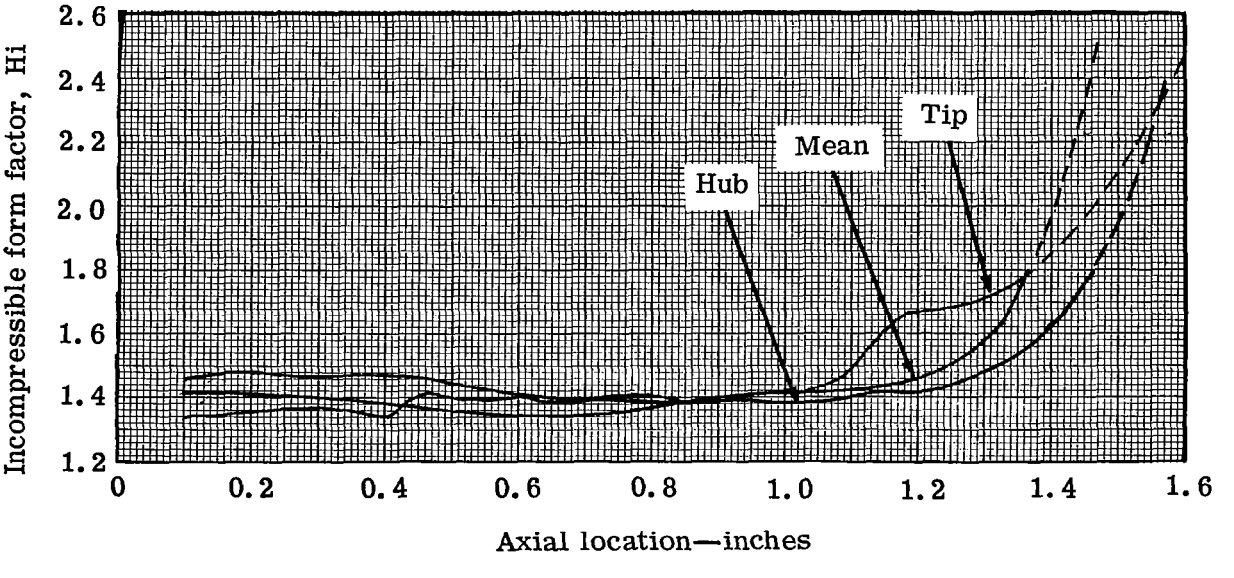

Figure 12. Plain rotor-blade suction surface incompressible form factor.

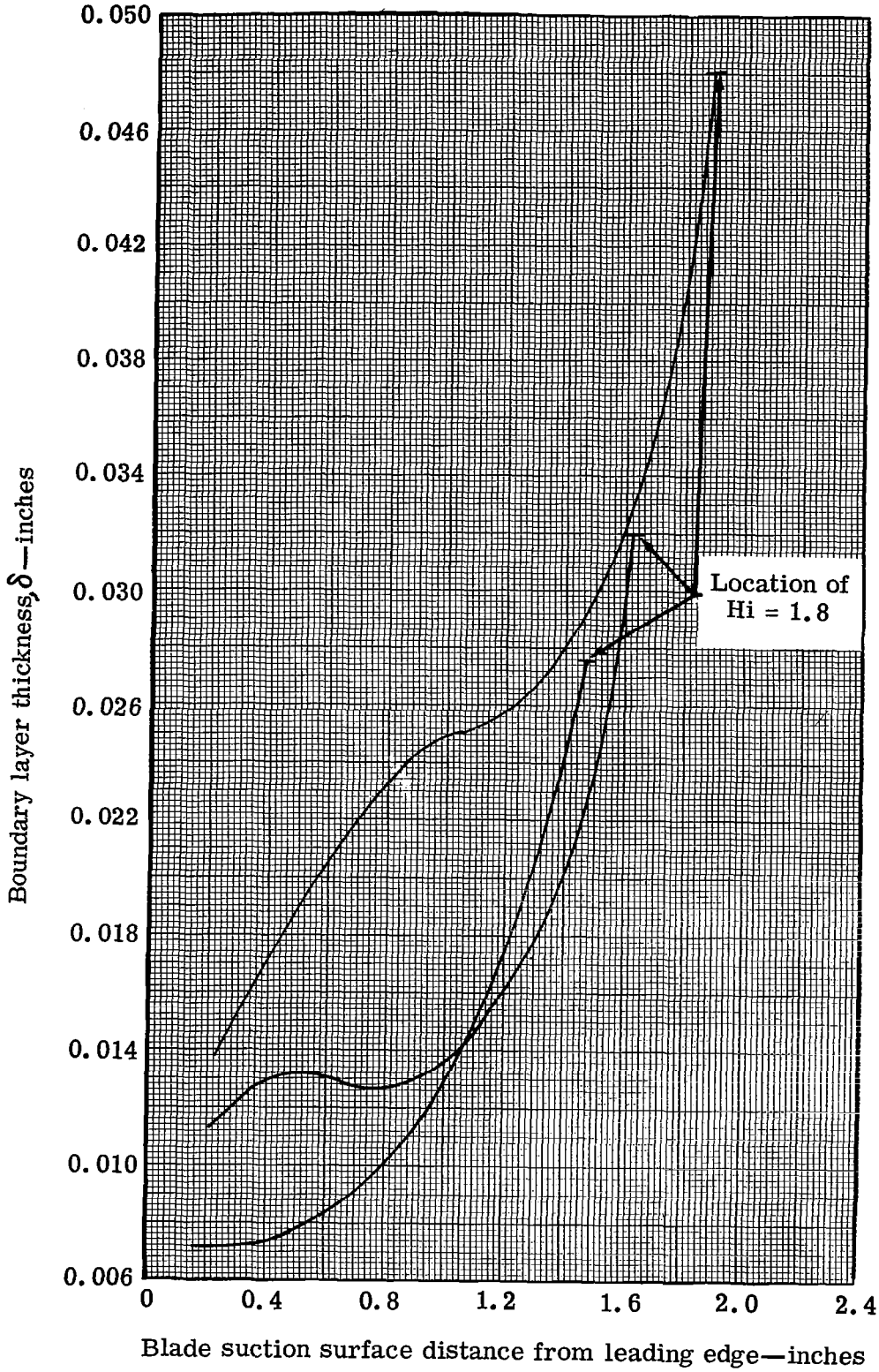

Figure 13. Boundary layer thickness of suction surface of plain rotor-blade.

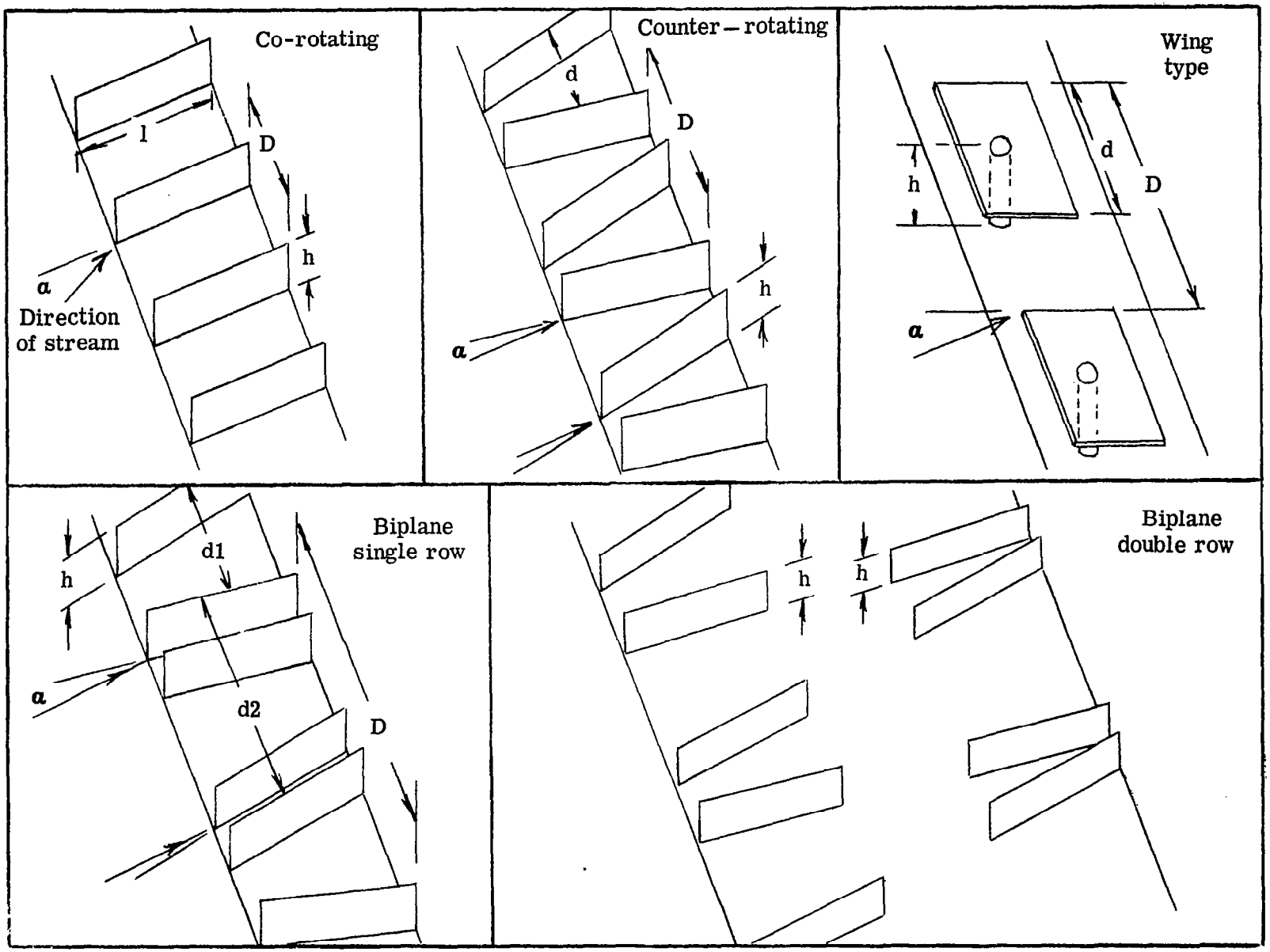

Figure 14. Vane-type vortex generators.

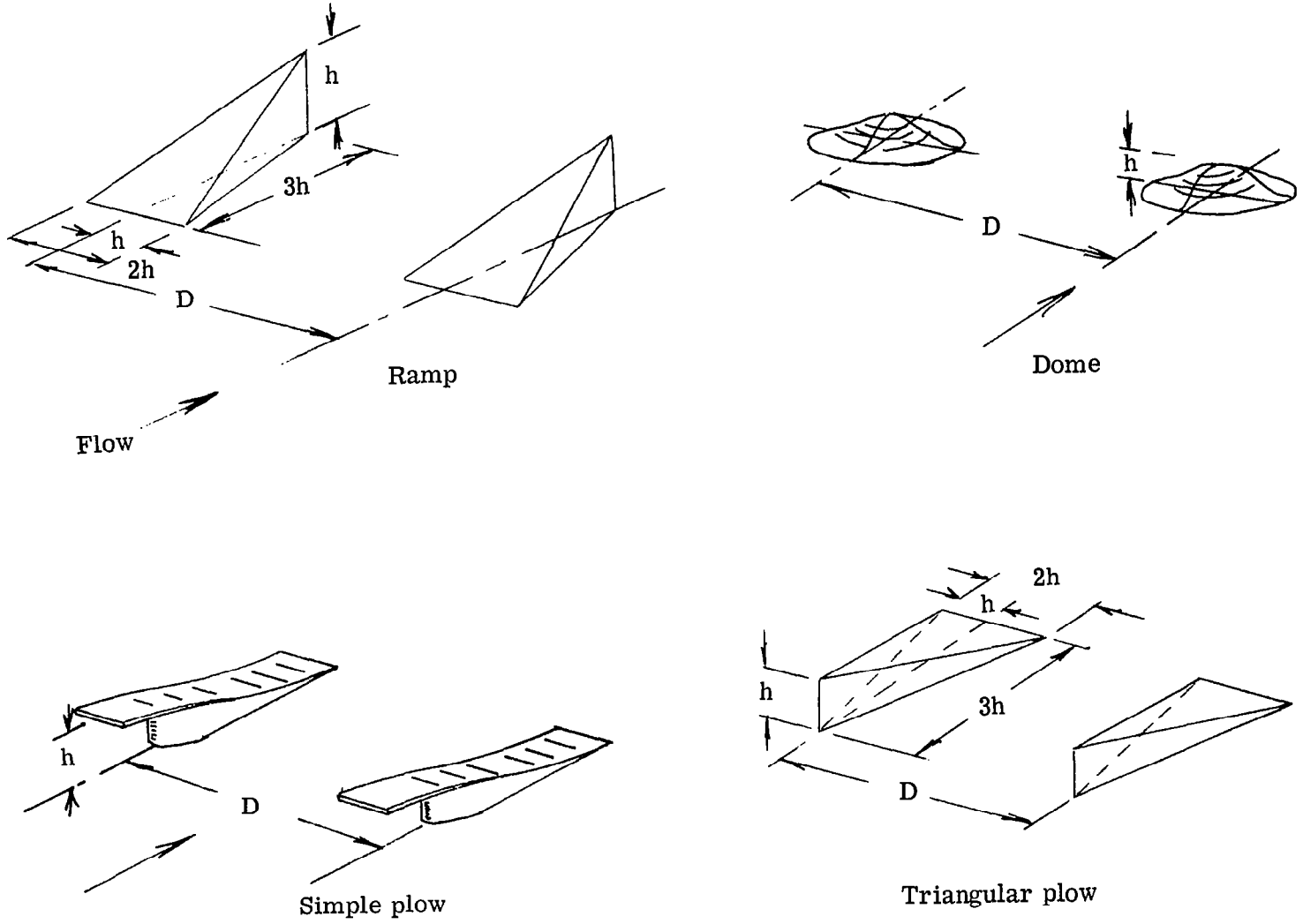

Figure 15. Three-dimensional vortex generators.

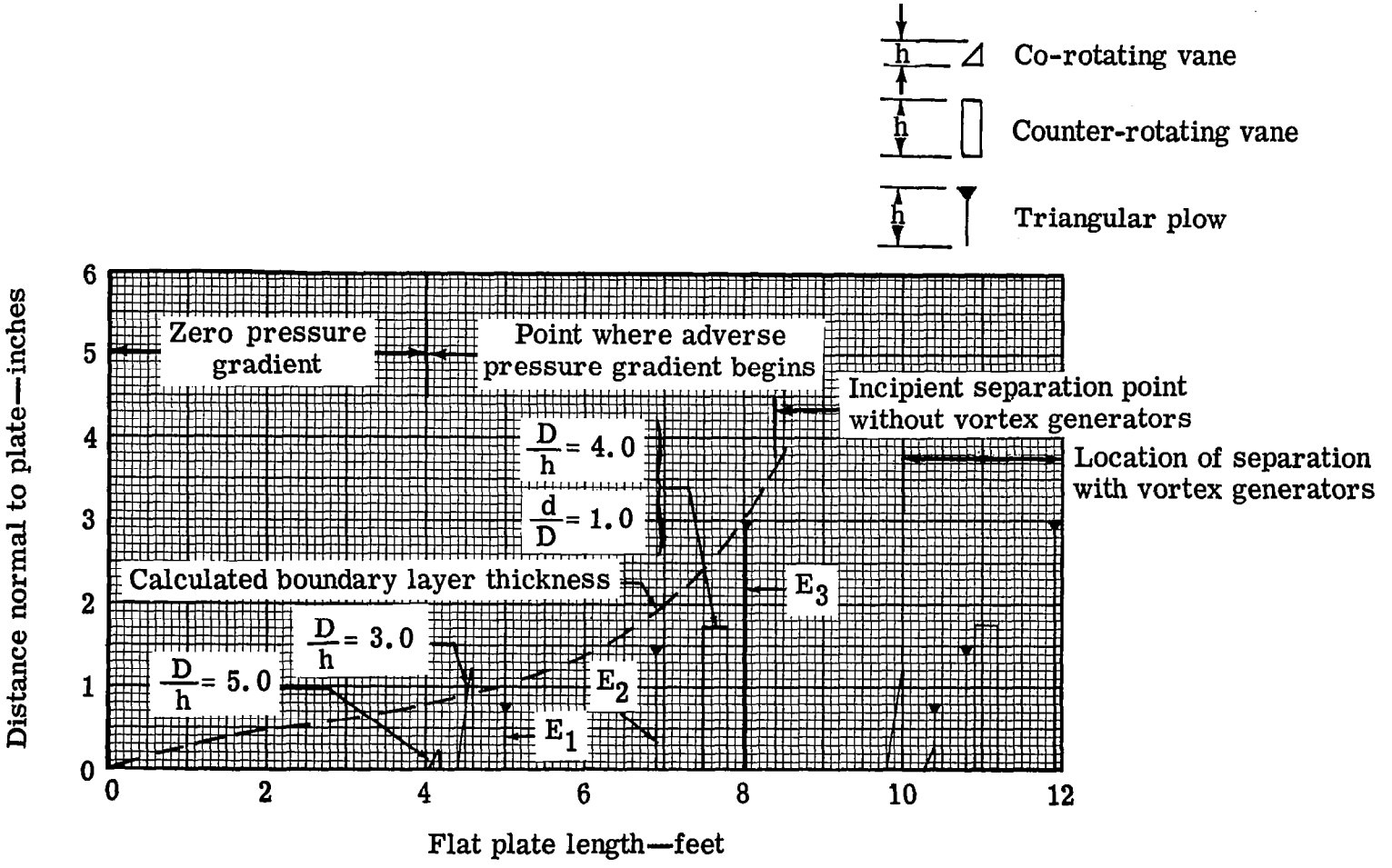

Figure 16. Comparison of vortex generator range.

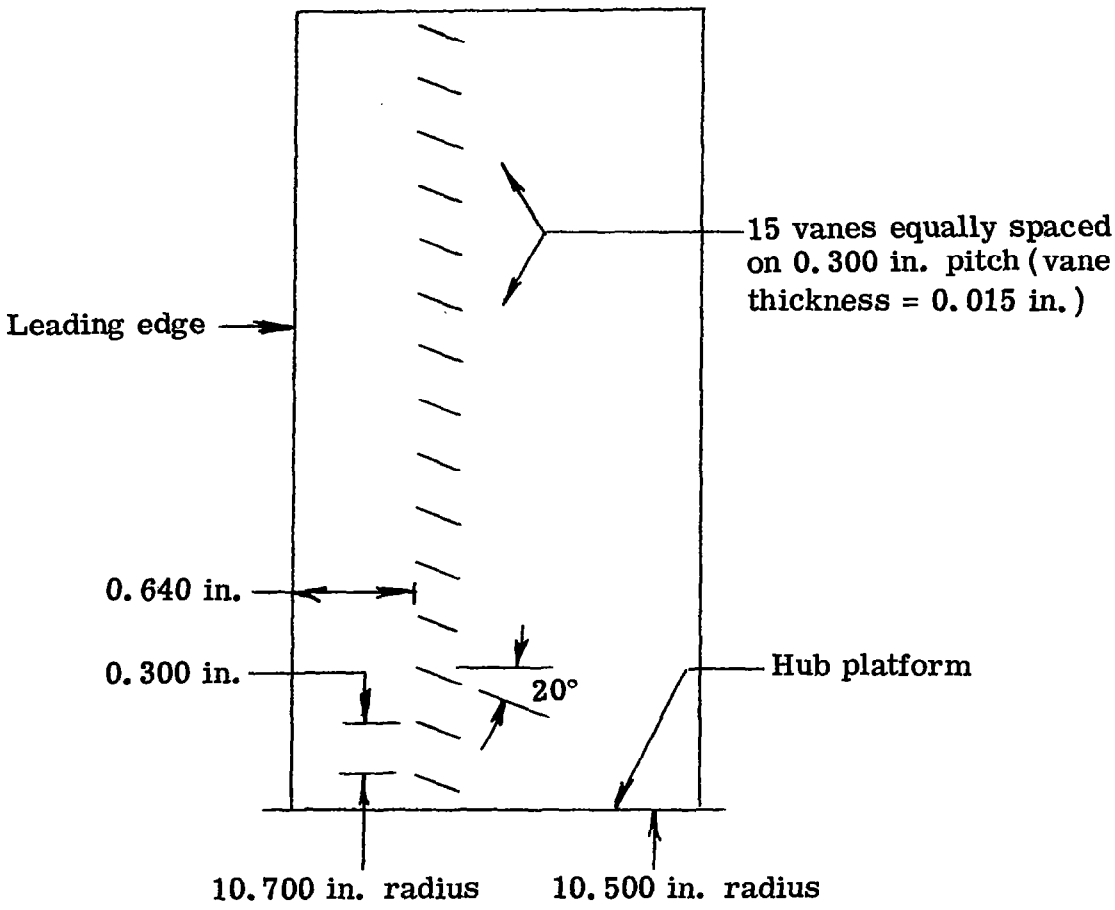

Figure 17. Plain rotor-blade with co-rotating vortex generators.

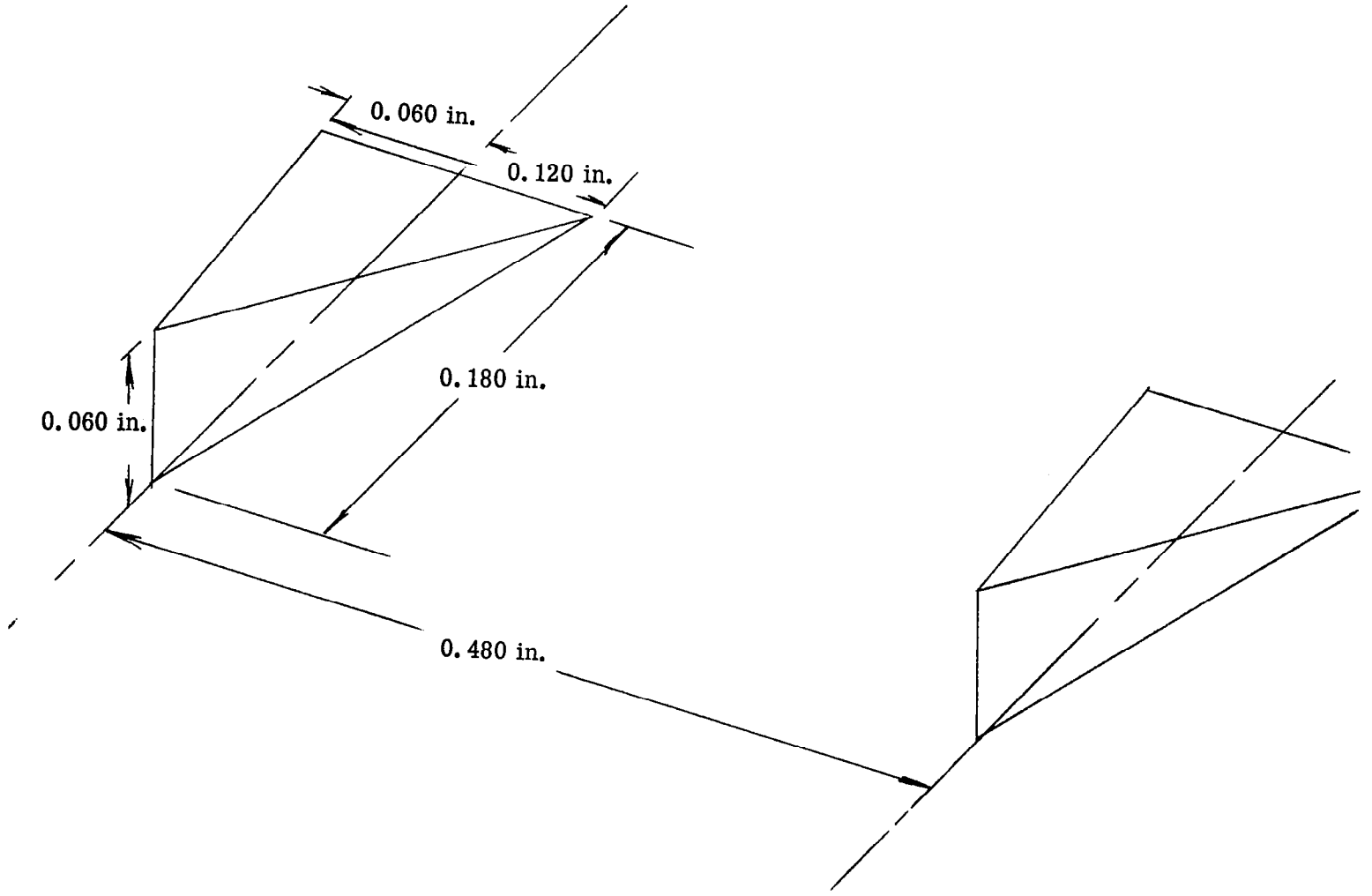

Figure 18. Triangular plow configuration.

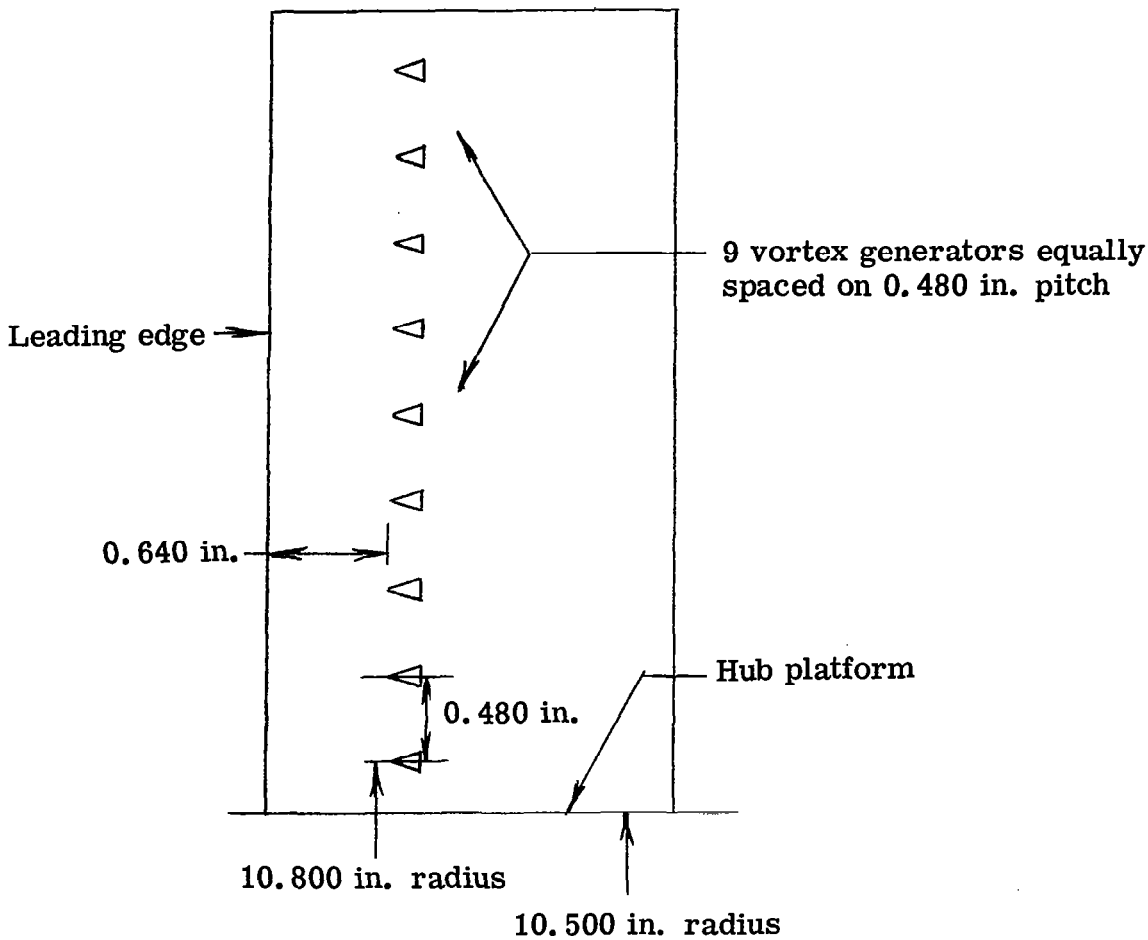

Figure 19. Side view of plain rotor-blade with triangular plow vortex generator.

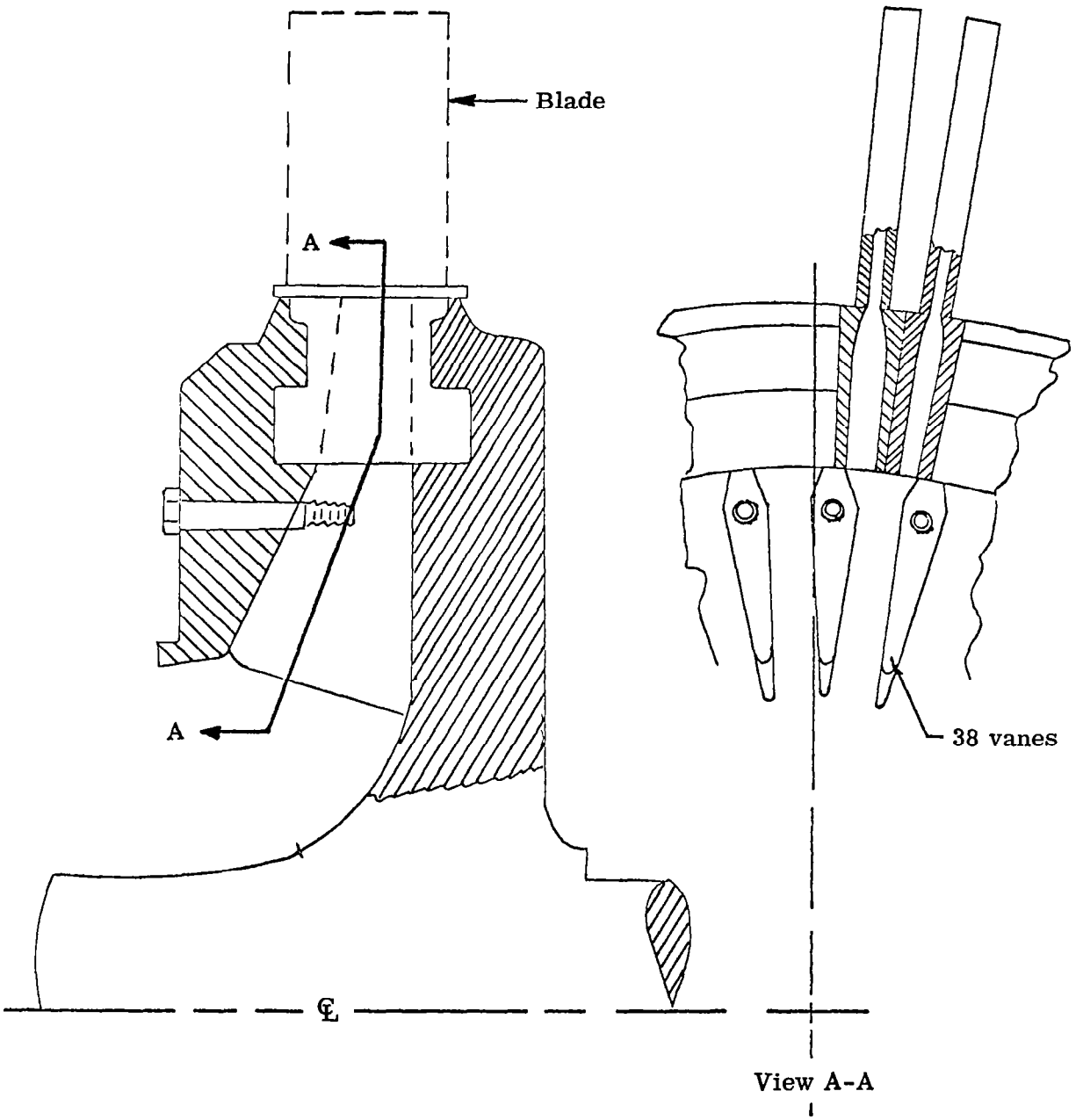

Figure 20. Rotor wheel assembly schematic.

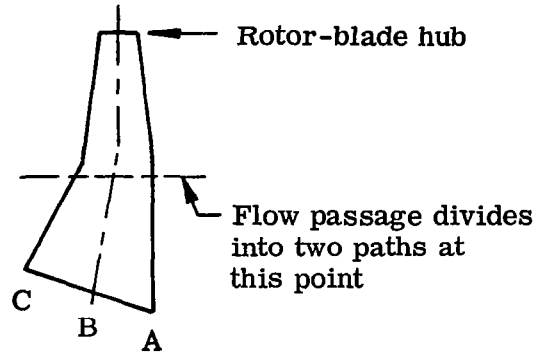

Secondary flow rotor-vane

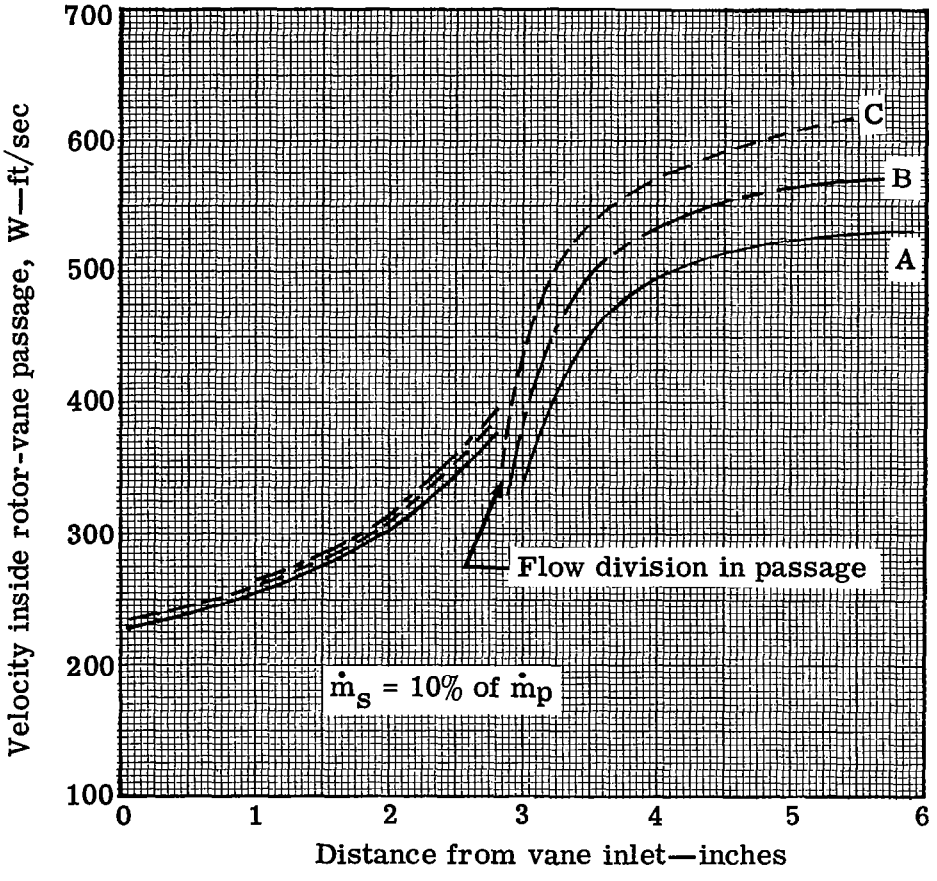

Figure 21. Velocity distribution inside rotor-vane based on $P_{T_I}/\delta o$ = 14.7 psia and $T_{T_I}/\sqrt{\theta}cr$ = 518.7°R.

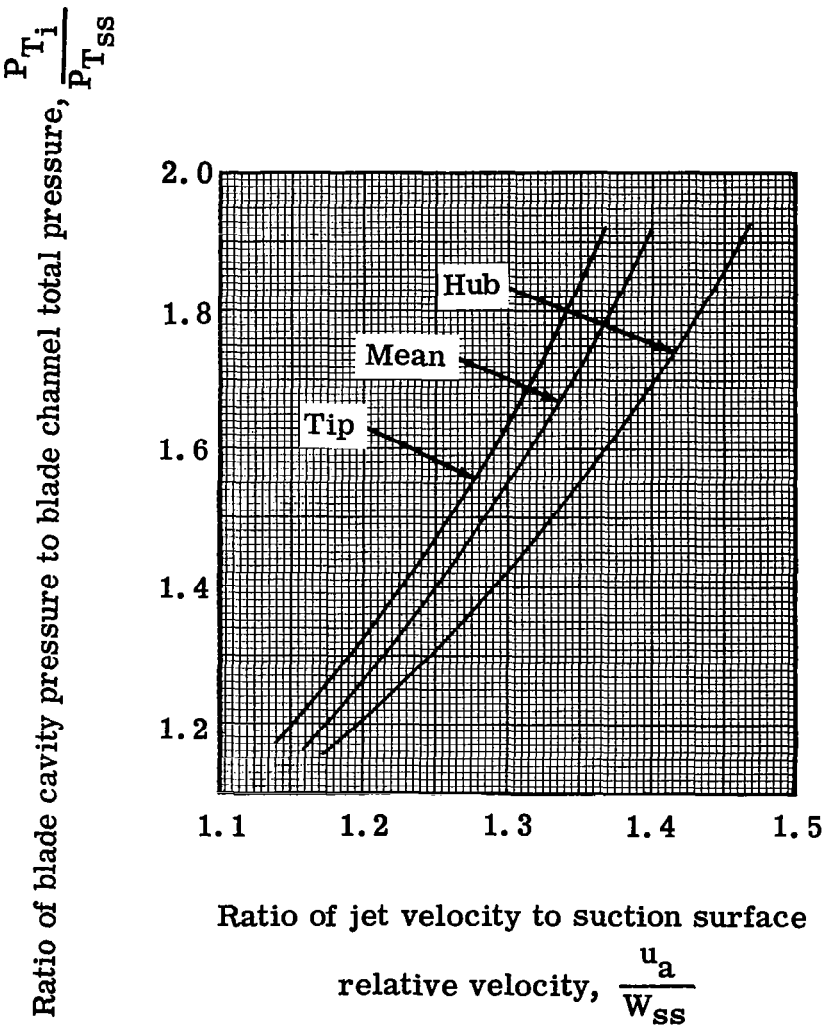

Figure 22. Variation of jet velocity ratio with slot total pressure ratio.

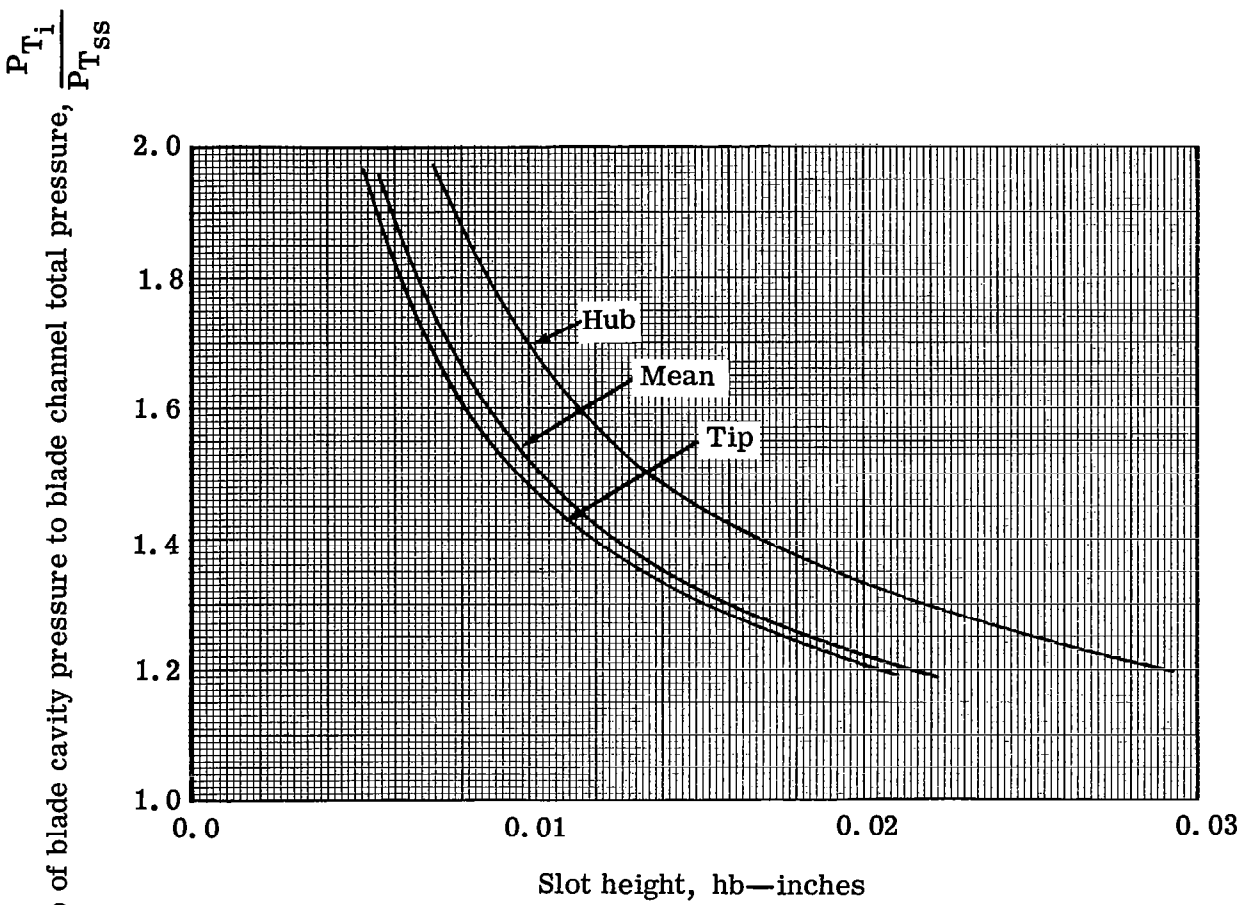

Figure 23. Variation of slot height with slot total pressure ratio.

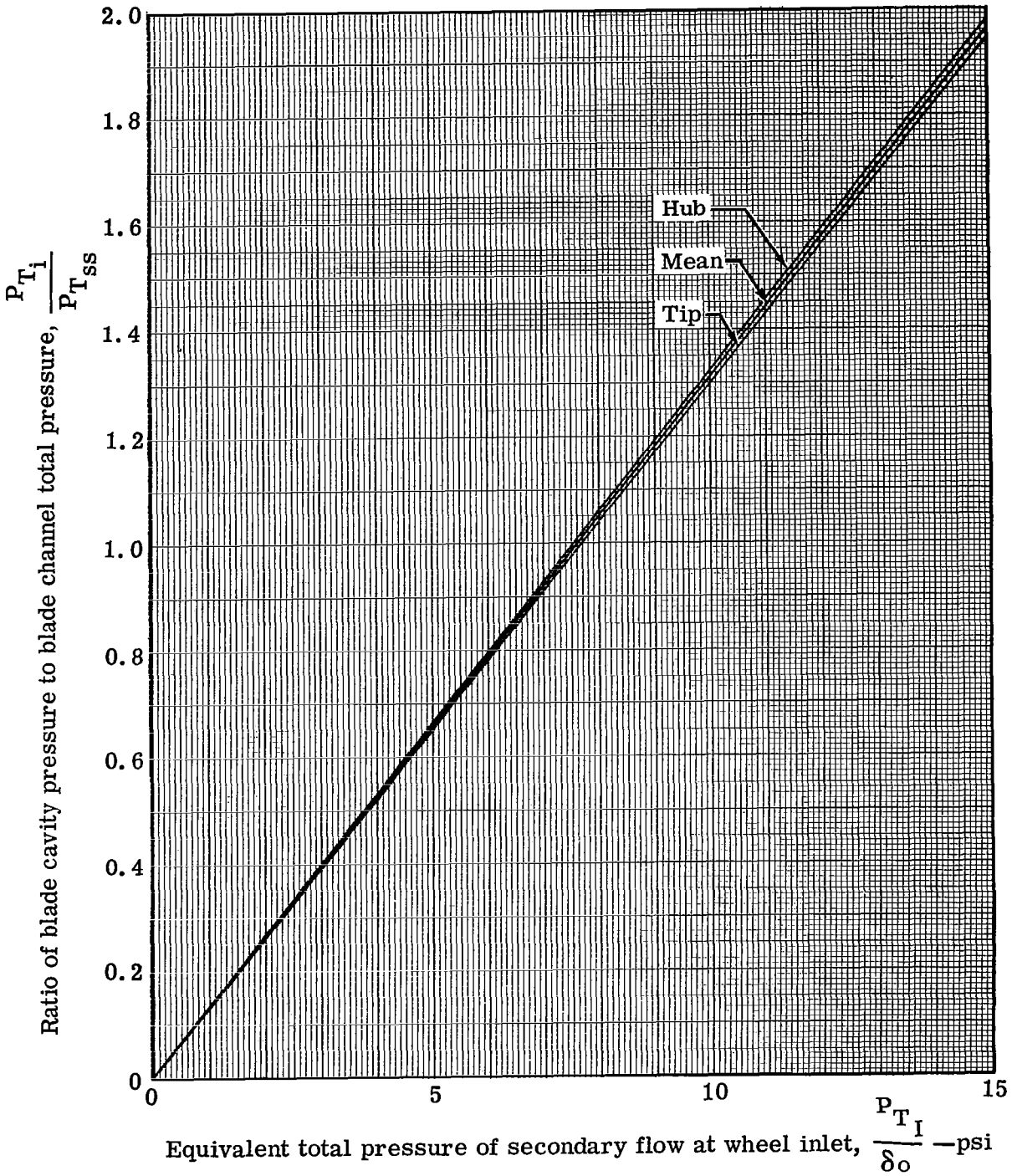

Figure 24. Variation of slot total pressure ratio with secondary flow inlet equivalent pressure.

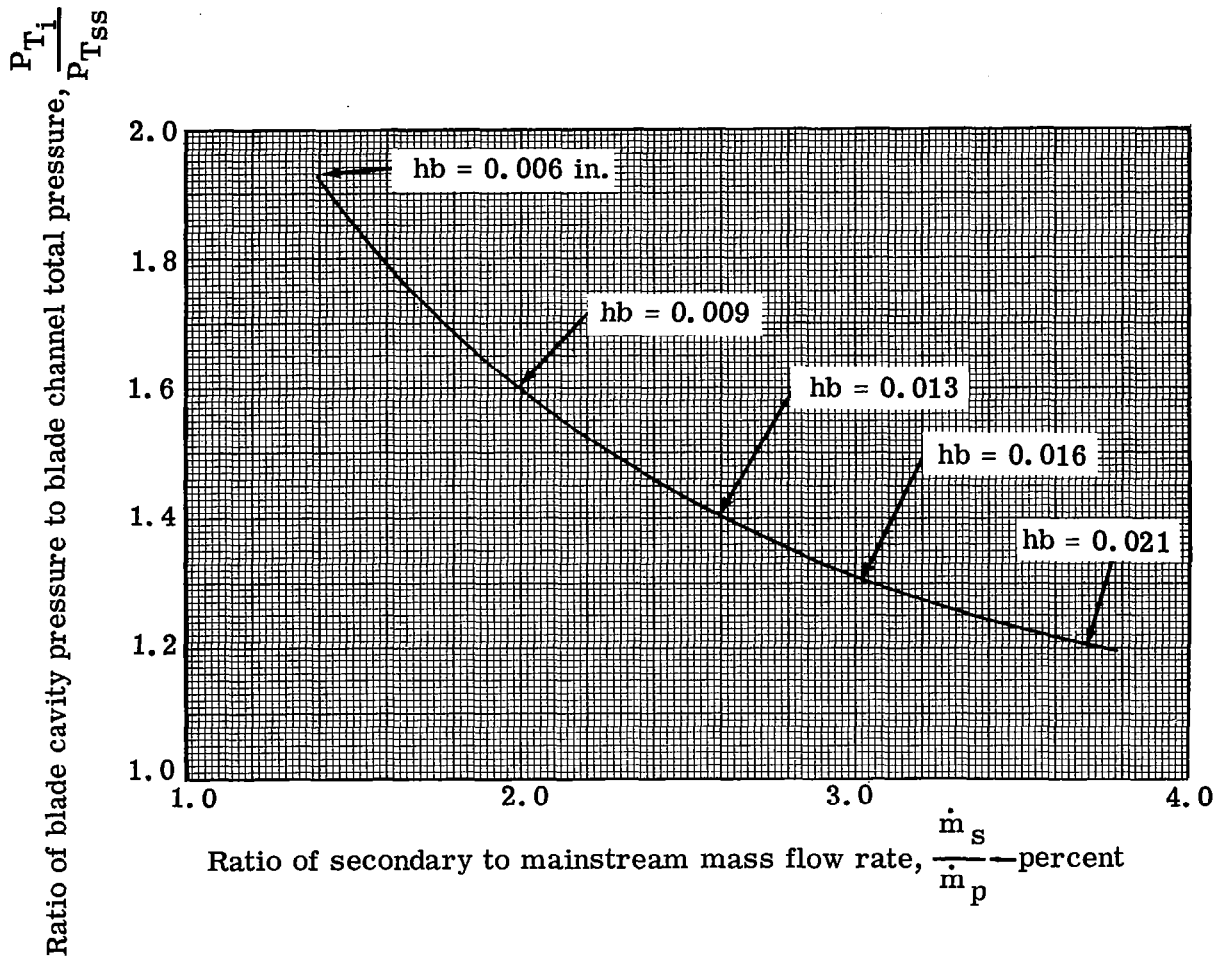

Figure 25. Variation of secondary to maintstream mass ratio with slot total pressure ratio.

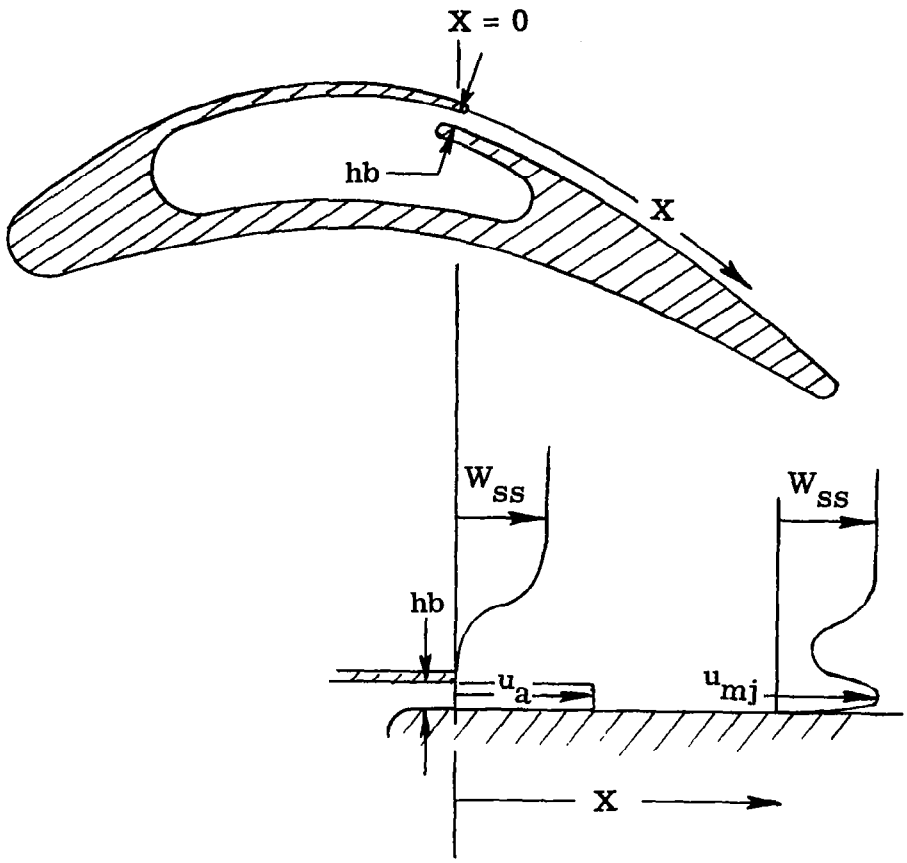

Figure 26. Tangential blowing rotor-blading nomenclature.

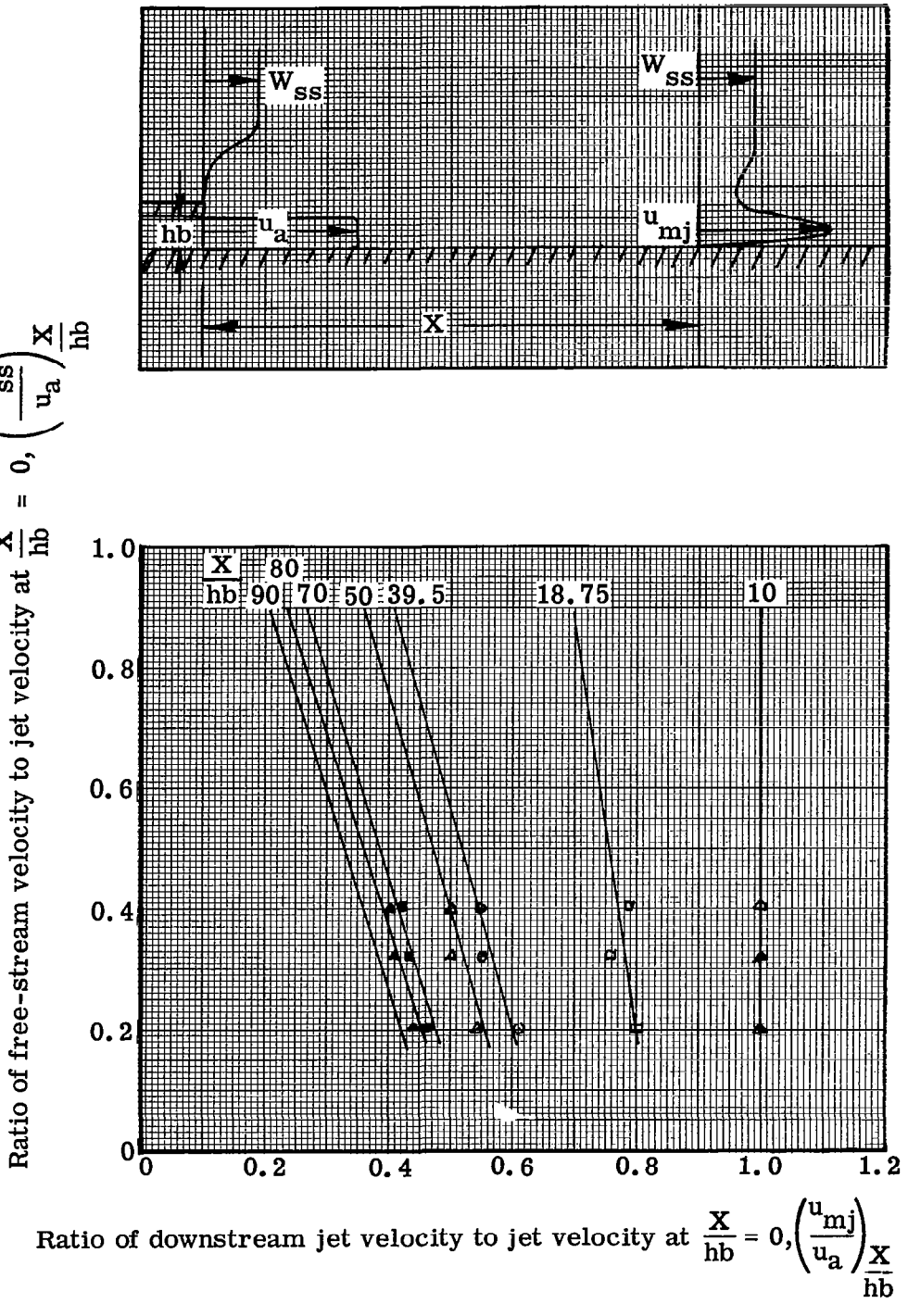

Figure 27. Variation of maximum jet velocity with location downstream of injection slot.

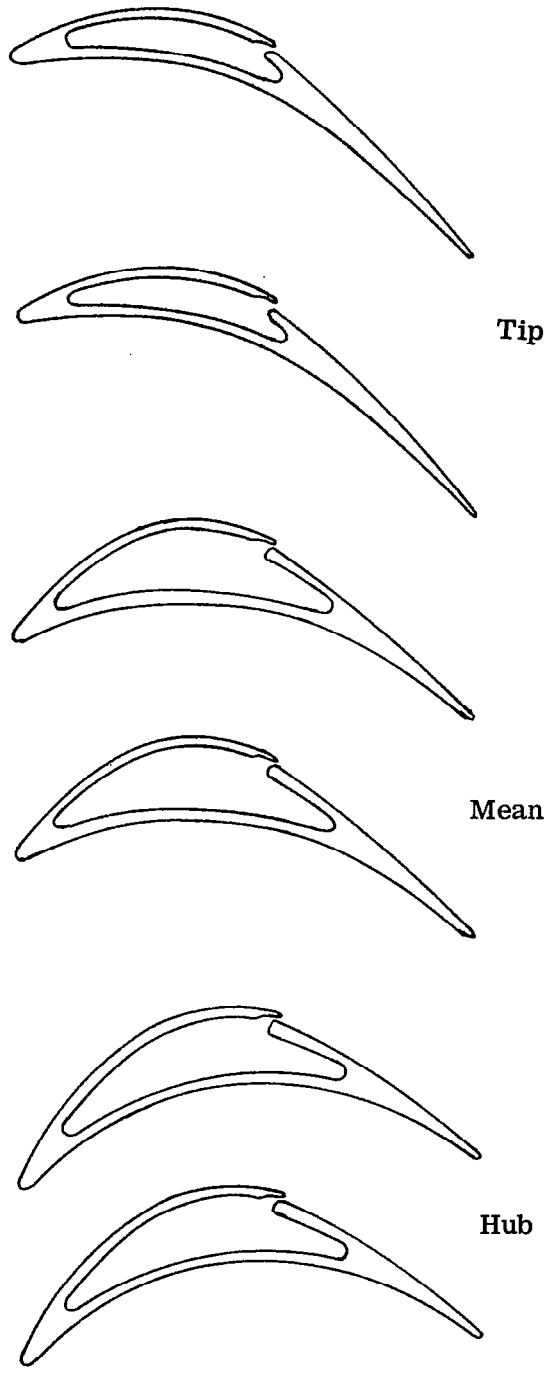

Figure 28. Tangential blowing rotor-blade profiles and passages.

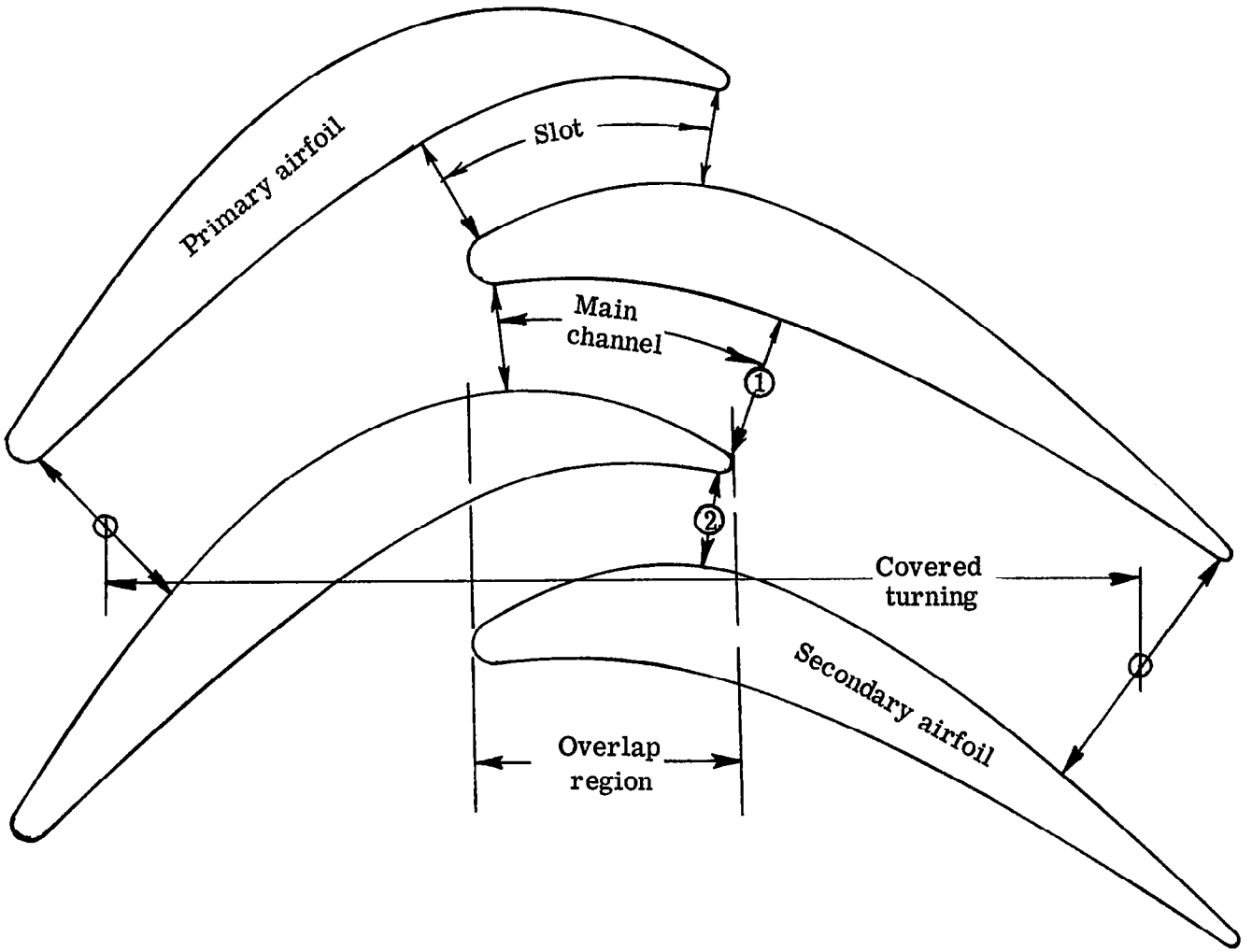

Figure 29. Schematic of tandem rotor-blade illustrating division of flow regimes used in analysis.

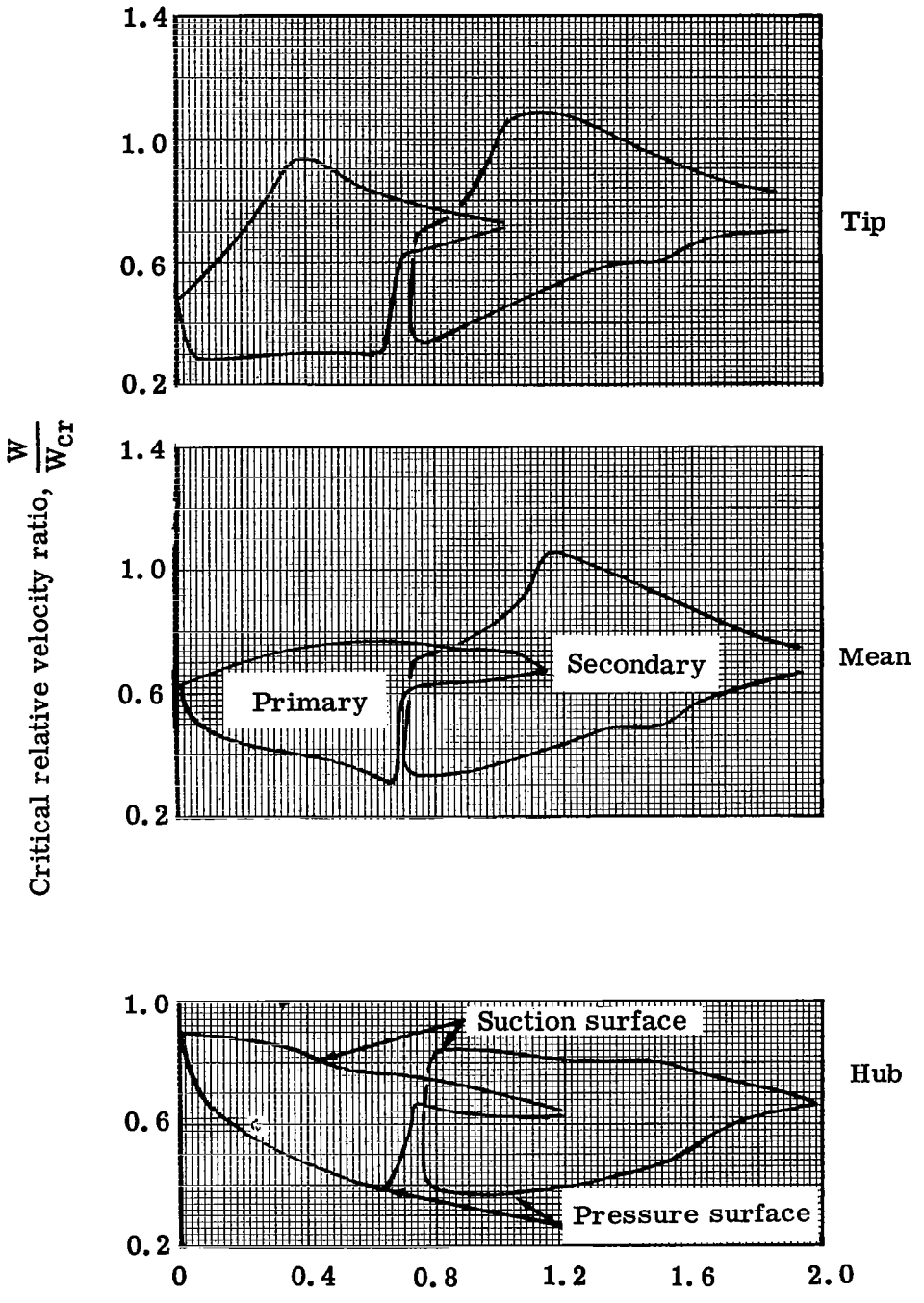

Figure 30. Design tandem rotor-blade surface velocity distribution.

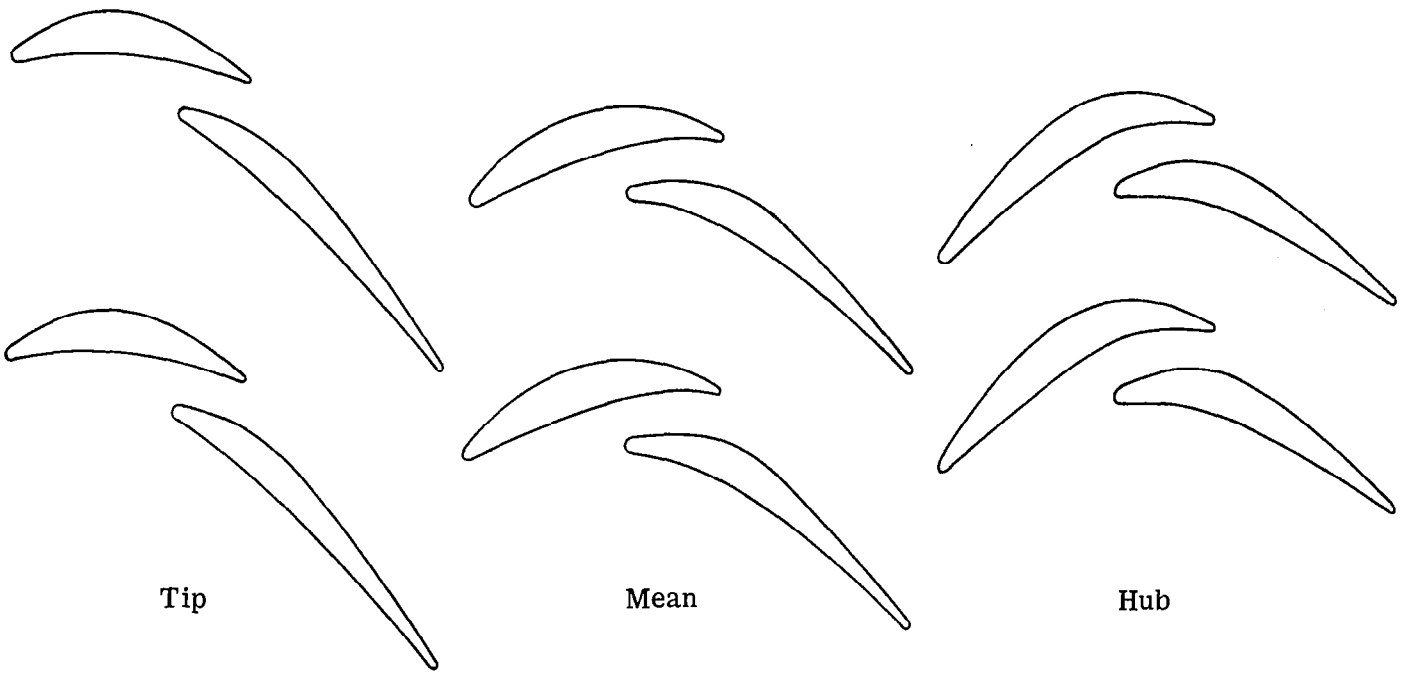

Figure 31. Tandem rotor-blade profiles and channels.

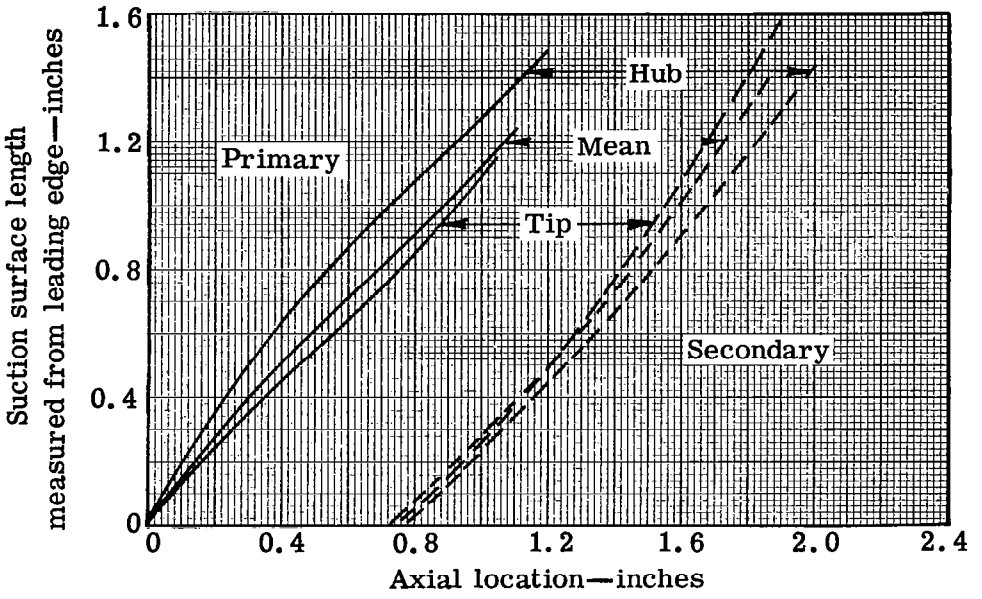

Figure 32. Variation of suction-surface length with axial chord for tandem rotor-blade.

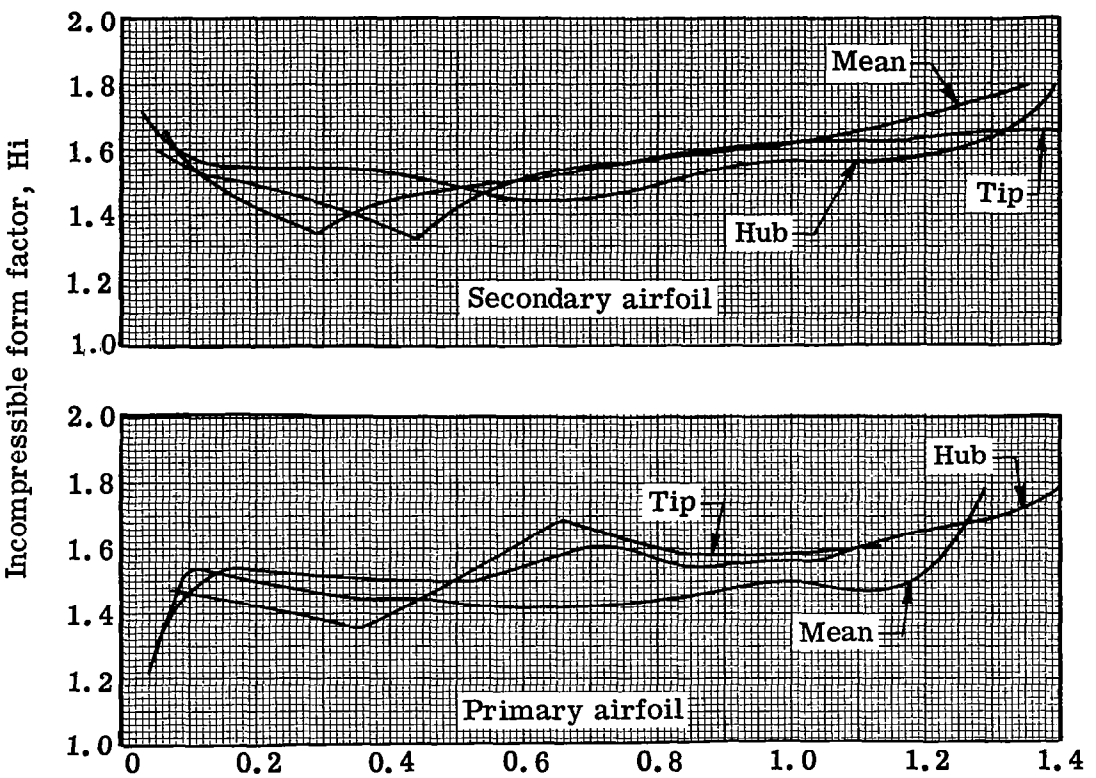

Figure 33. Tandem rotor-blade primary and secondary airfoil suction surface incompressible form factor.

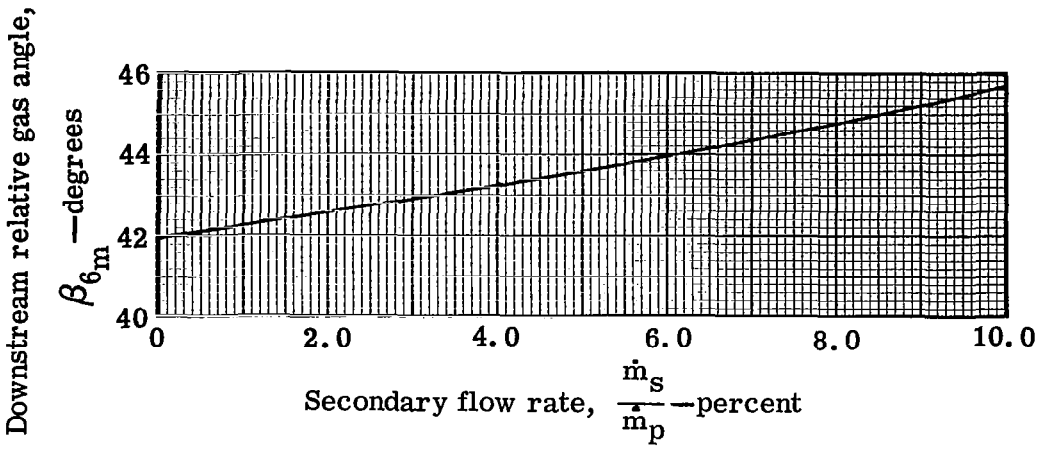

(a) Variation of downstream relative gas angle with secondary flow rate

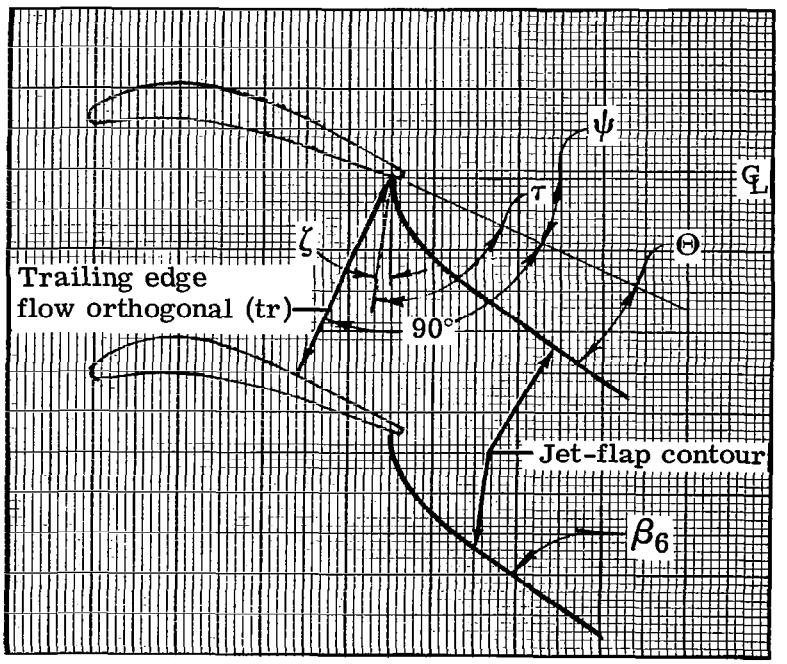

(b) Jet-flap nomenclature

Figure 34. Jet-flap rotor-blade nomenclature and downstream relative gas angle variation with jet-flap secondary flow rate.

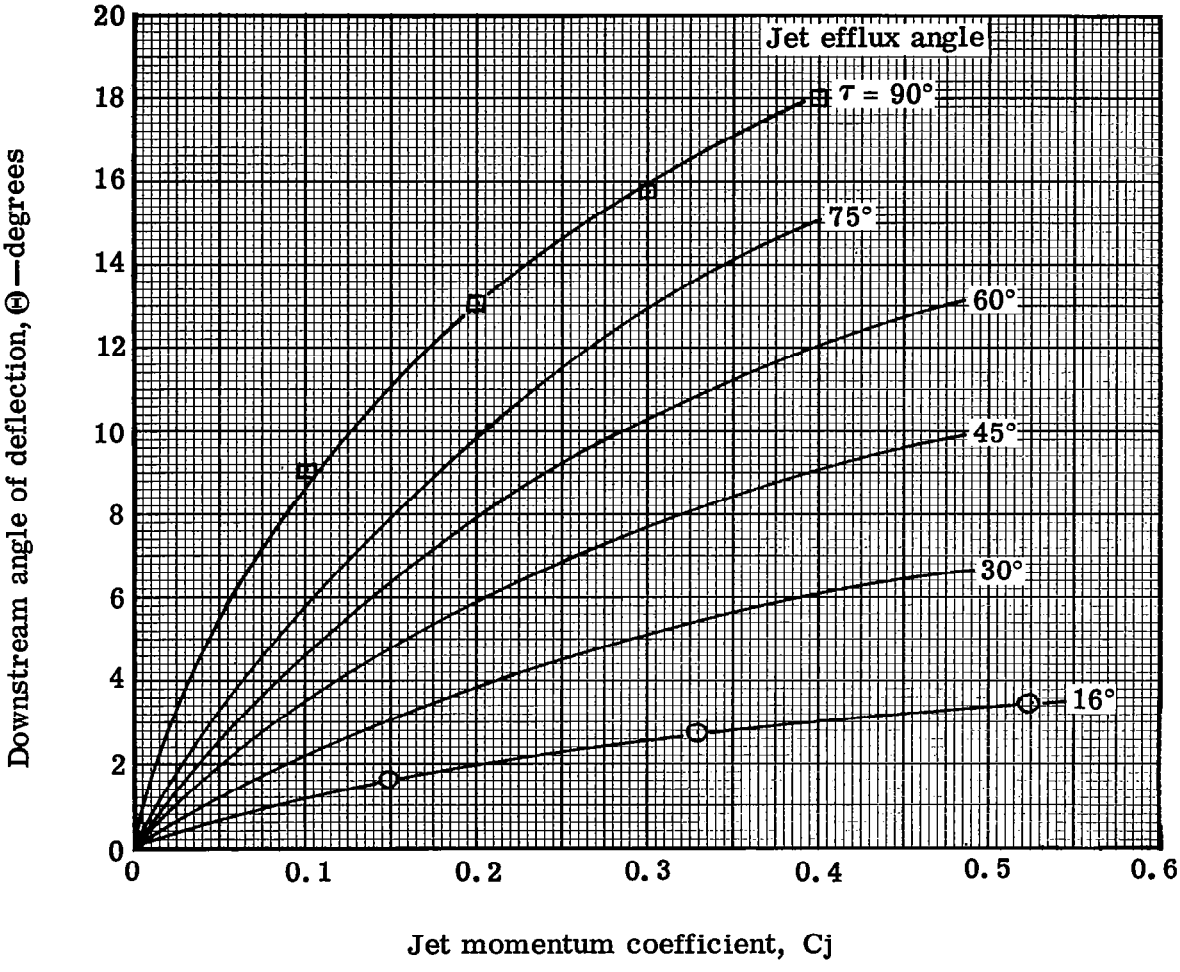

Figure 35. Variation of primary stream deflection with jet momentum coefficient and jet efflux angle.

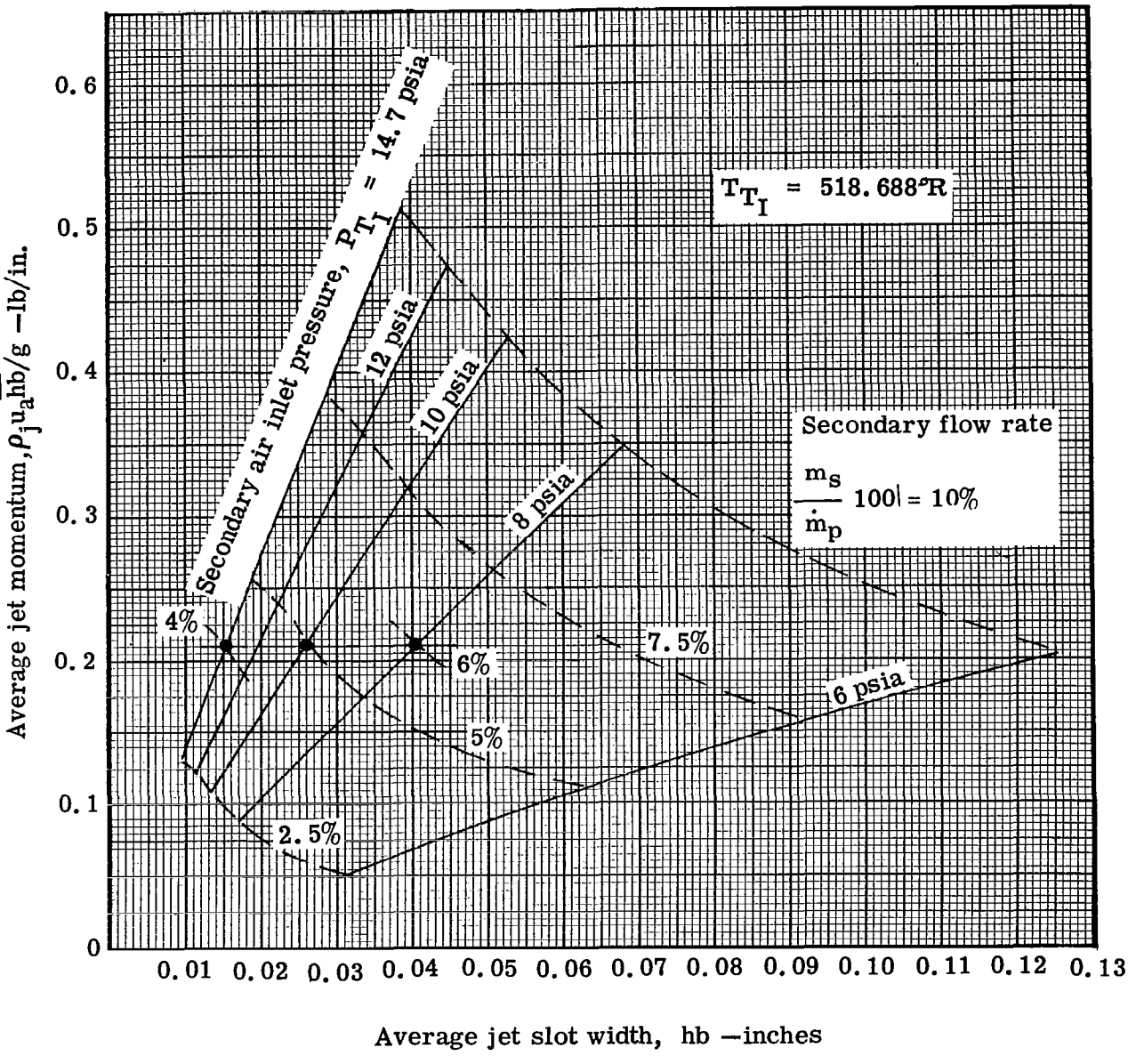

Figure 36. Variation of average jet momentum with average slot width and secondary air pressure.

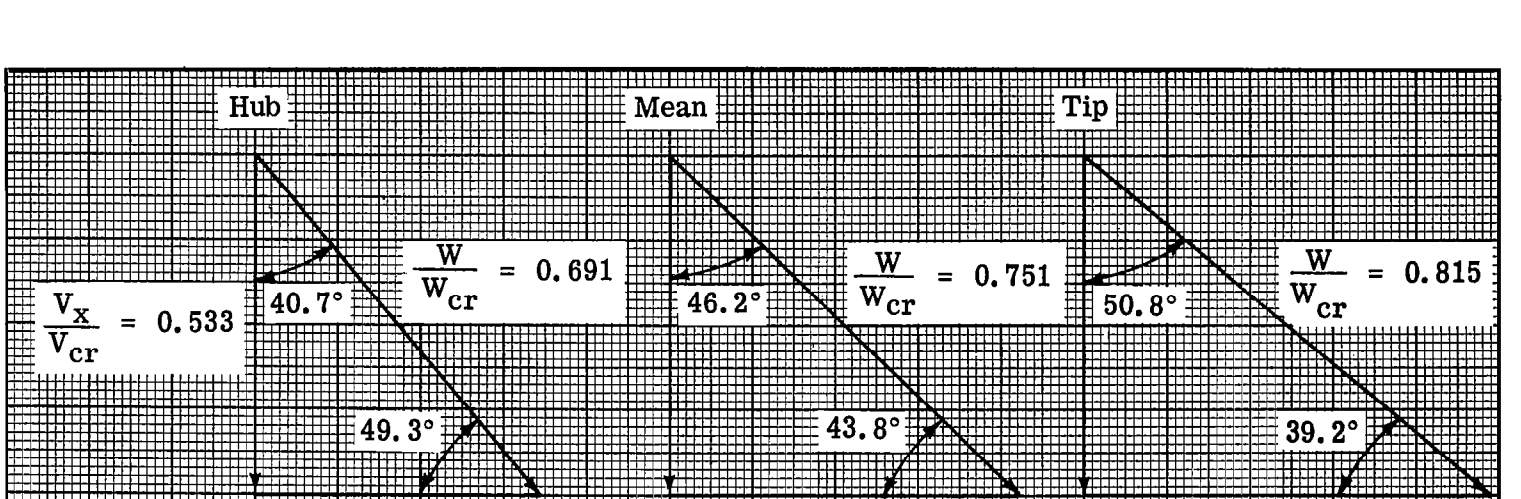

Figure 37. Jet-flap downstream velocity diagram with 5 percent secondary flow.

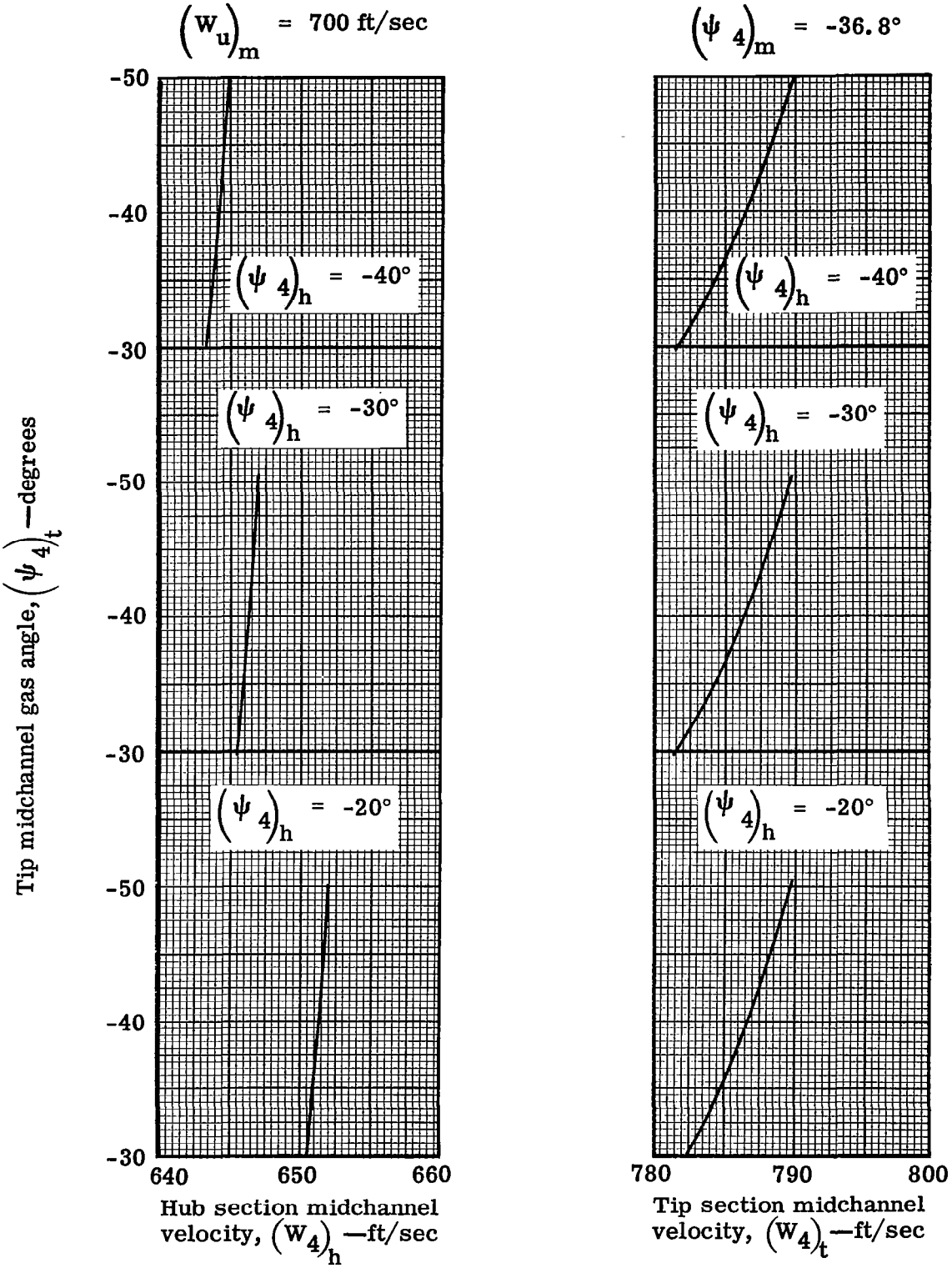

Figure 38. Variation of jet-flap blade hub and tip section midchannel velocity with hub and tip midchannel gas angle at the trailing edge orthogonal.

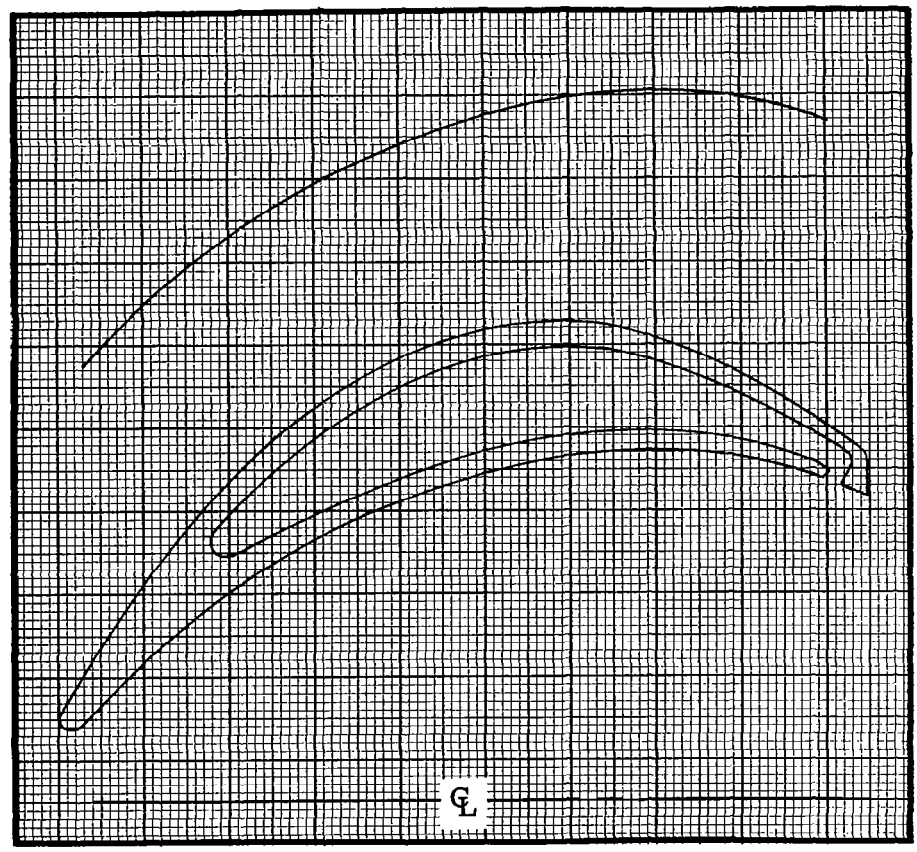

Figure 39. Jet-flap rotor-blade hub section profile and channel.

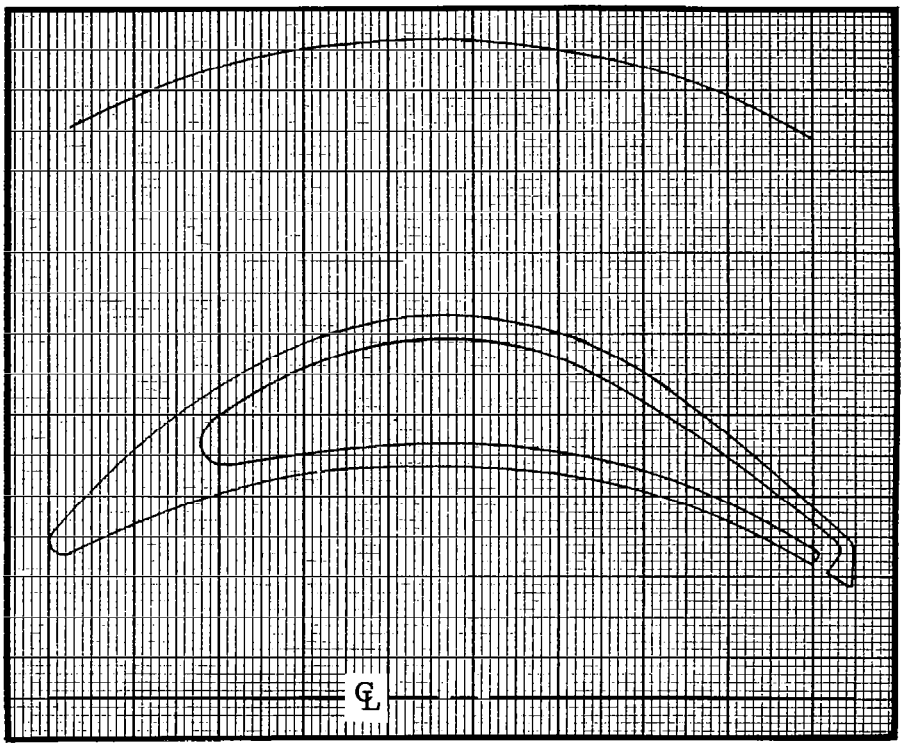

Figure 40. Jet-flap rotor-blade mean section profile and channel.

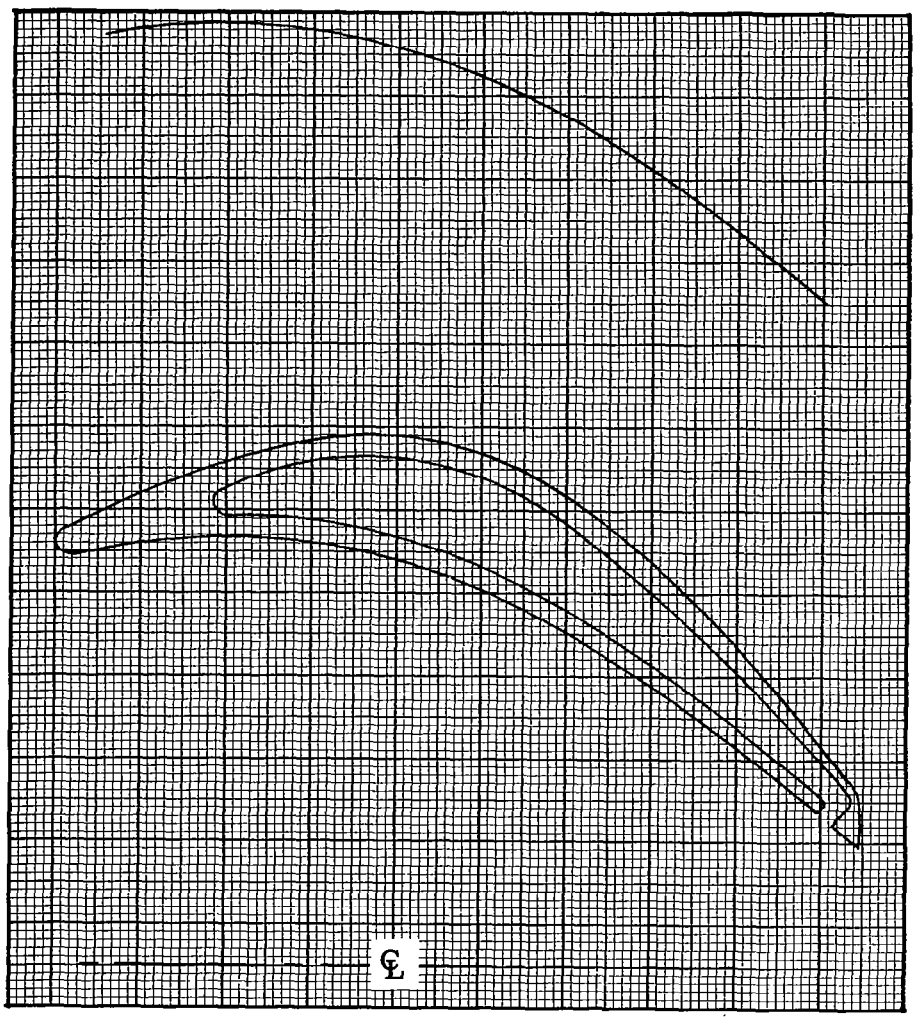

Figure 41. Jet-flap rotor-blade tip section profile and channel.

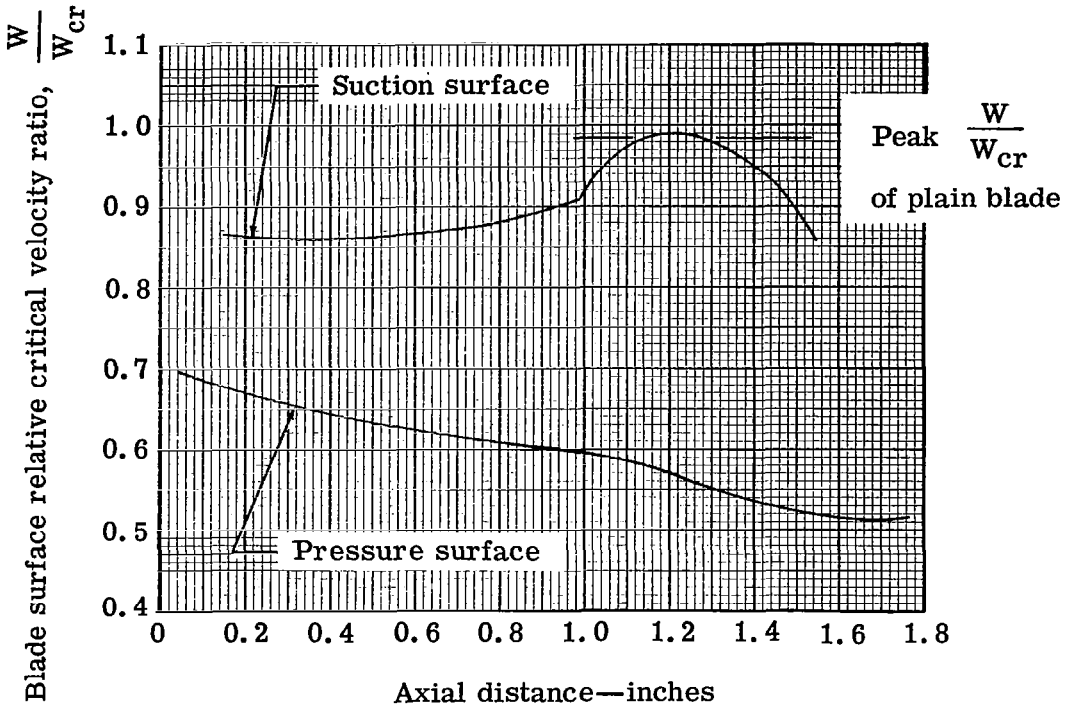

Figure 42. Jet-flap rotor-blade hub section surface velocity distribution without jet.

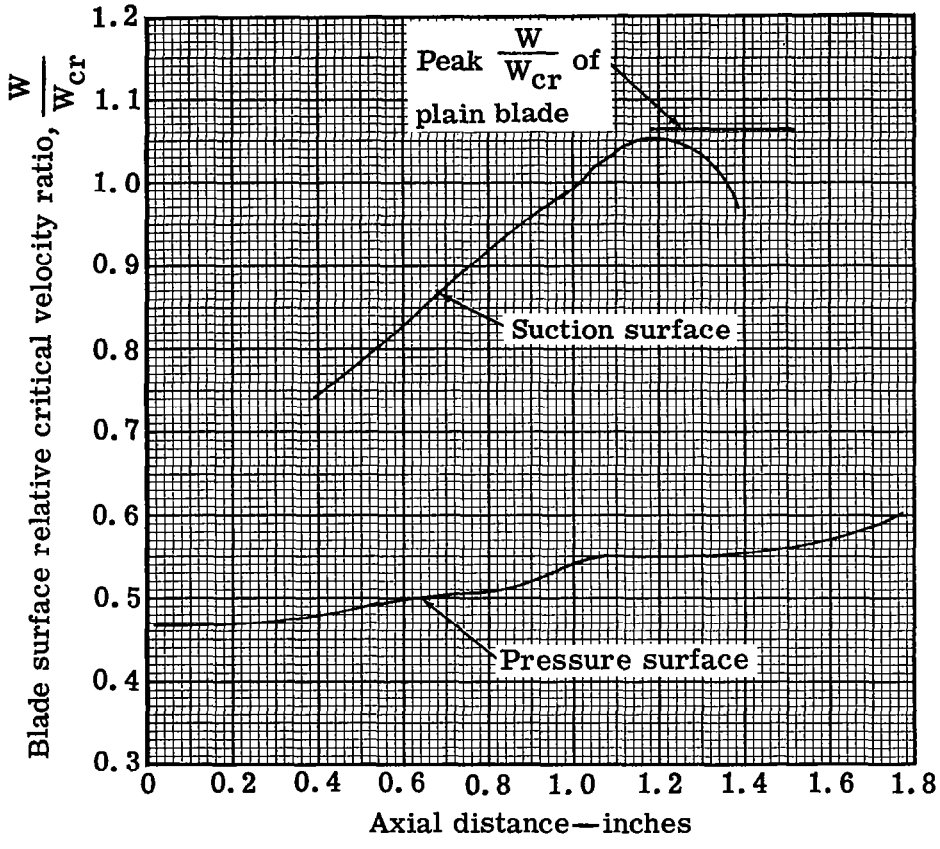

Figure 43. Jet-flap rotor-blade mean section surface velocity distribution without jet.

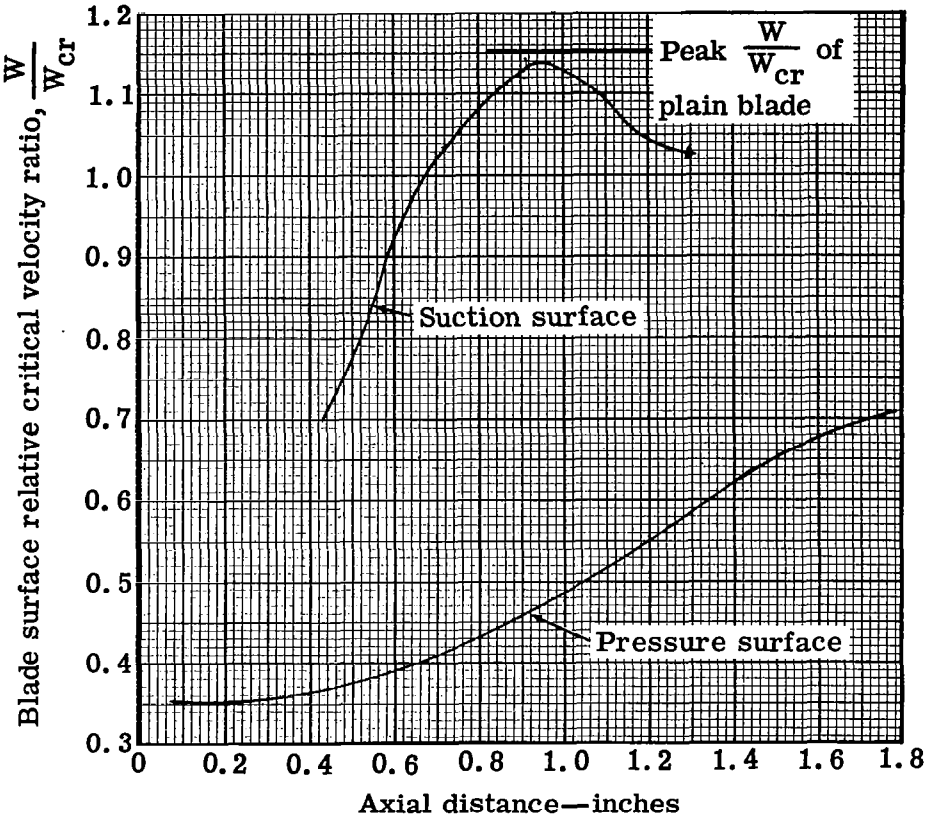

Figure 44. Jet-flap rotor-blade tip section surface velocity distribution without jet.

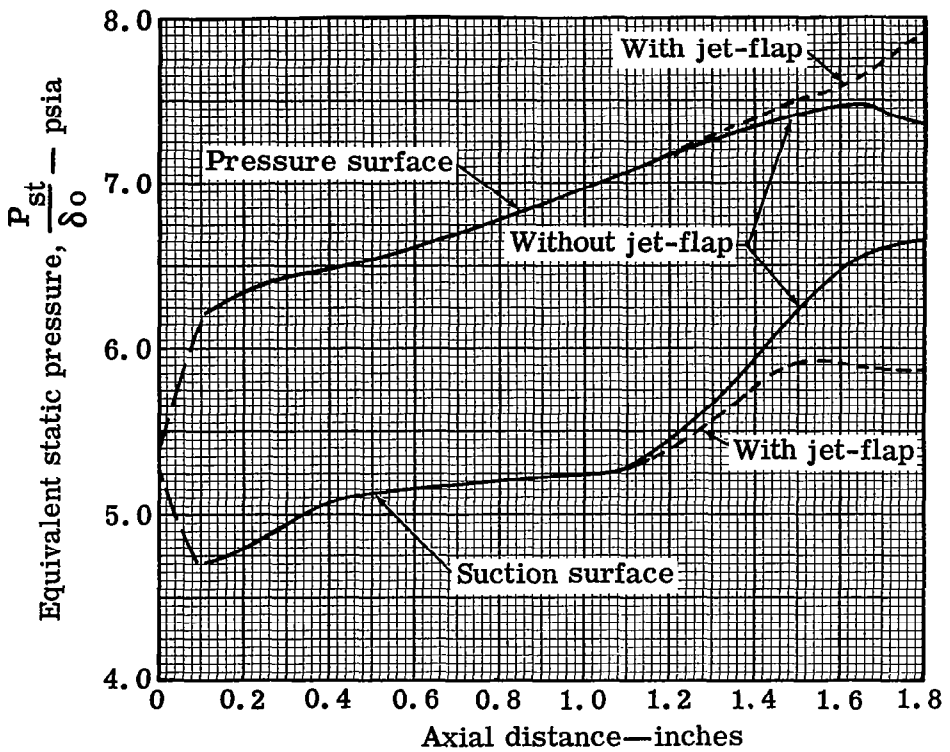

Figure 45. Jet-flap rotor-blade hub section surface static pressure distribution with and without jet-flap based on two-dimensional incompressible solution.

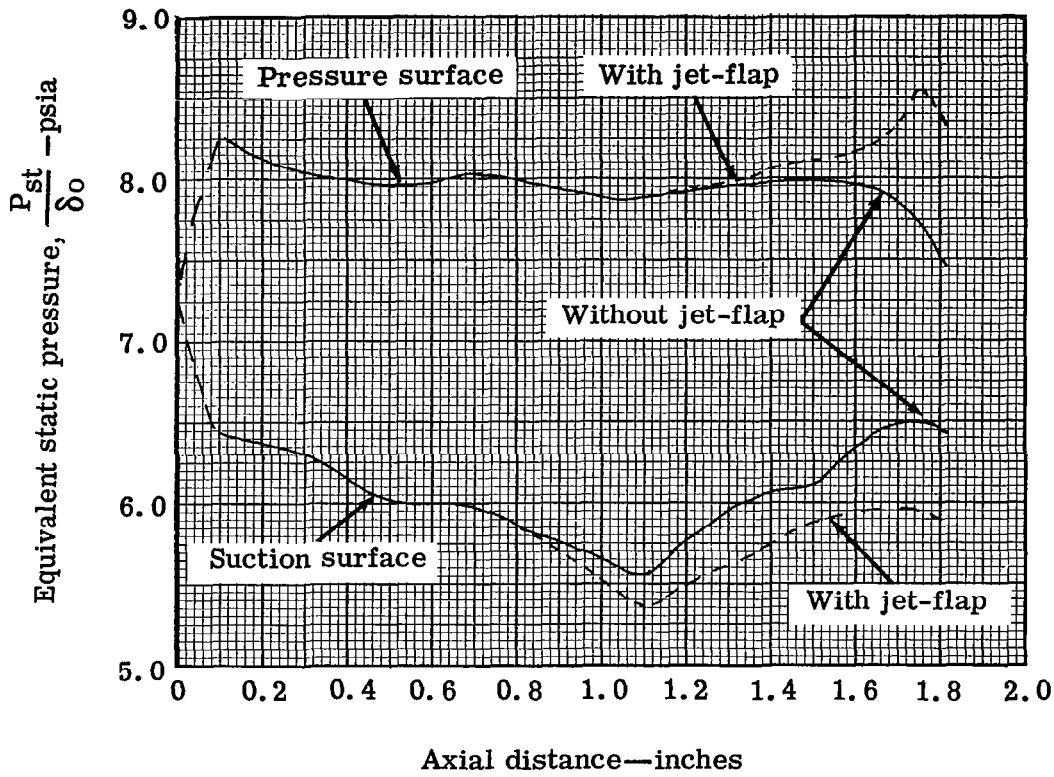

Figure 46. Jet-flap rotor-blade mean section surface static pressure distribution with and without jet-flap based on two-dimensional incompressible solution.

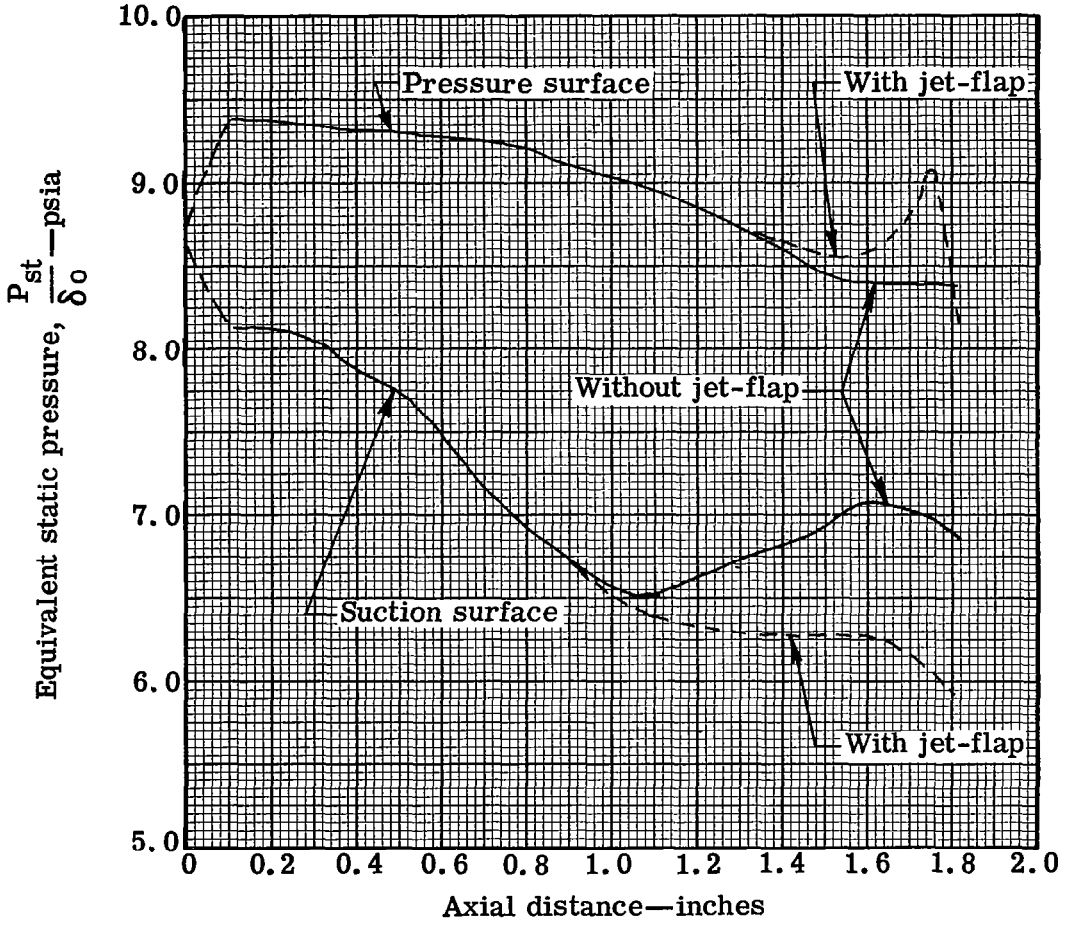

Figure 47. Jet-flap rotor-blade tip section surface static pressure distribution with and without jet-flap based on two-dimensional incompressible solution.

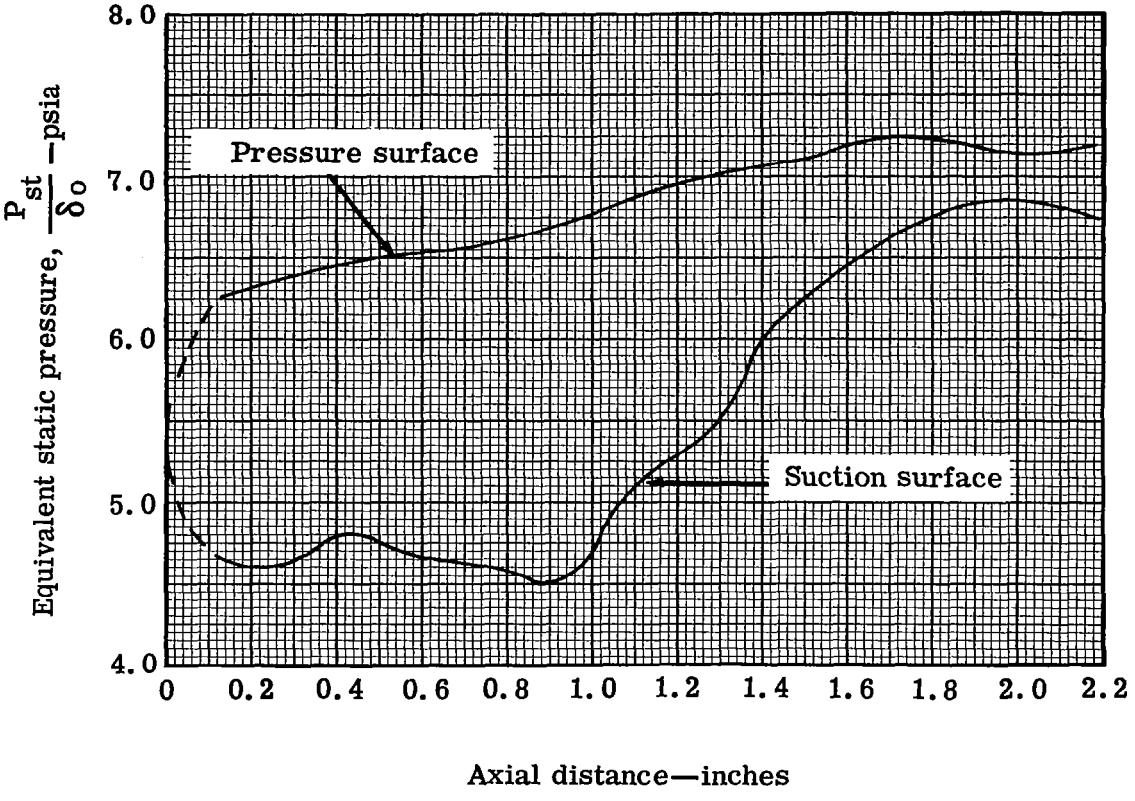

Figure 48. Plain rotor-blade hub section static pressure distribution based on incompressible two-dimensional solution.

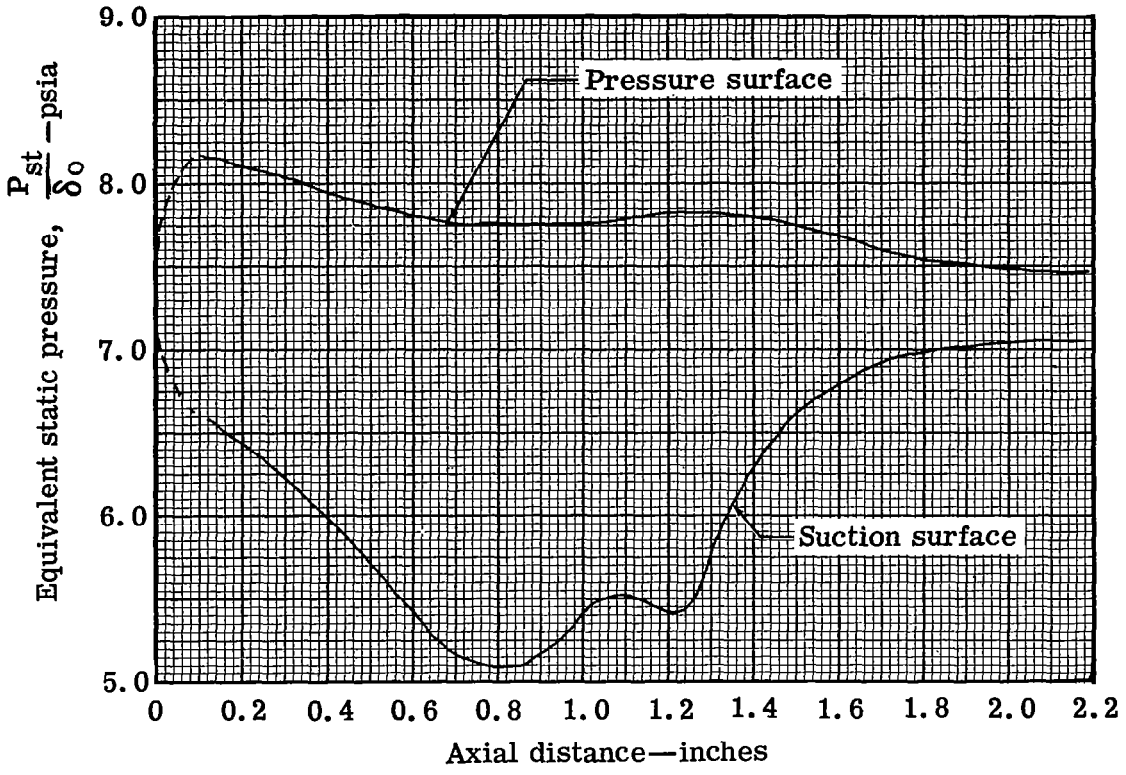

Figure 49. Plain rotor-blade mean section static pressure distribution based on incompressible two-dimensional solution.

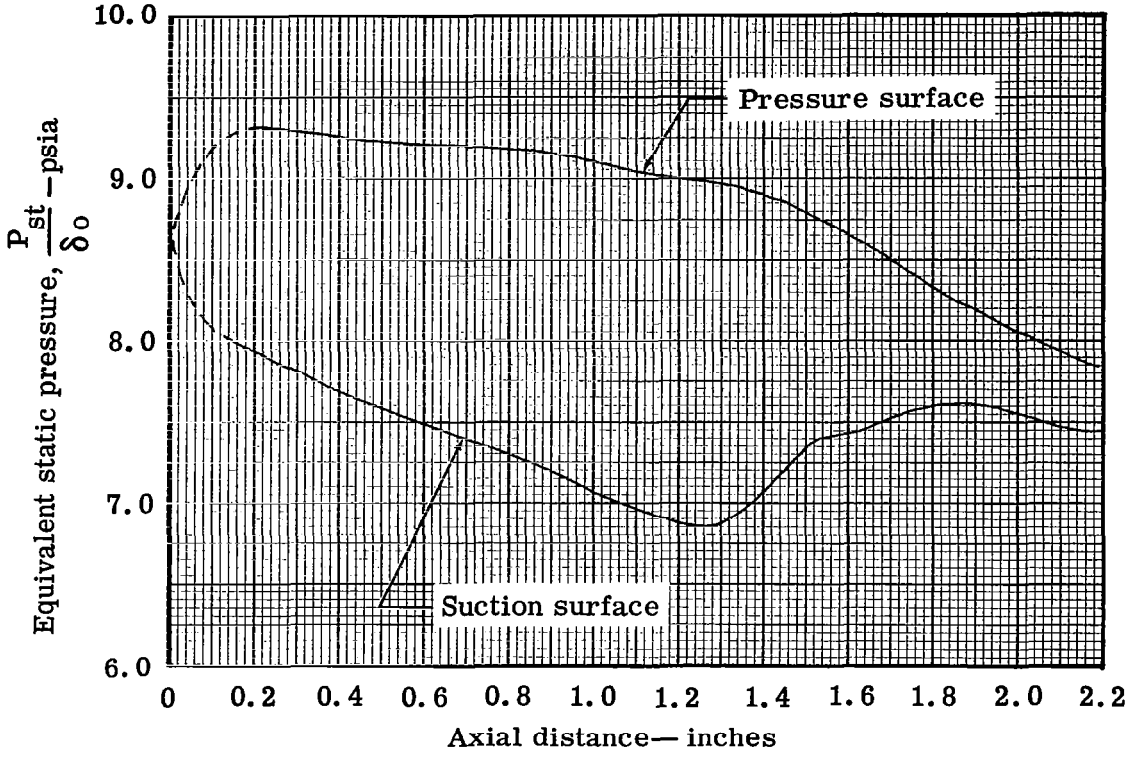

Figure 50. Plain rotor-blade tip section static pressure distribution based on incompressible two-dimensional solution.

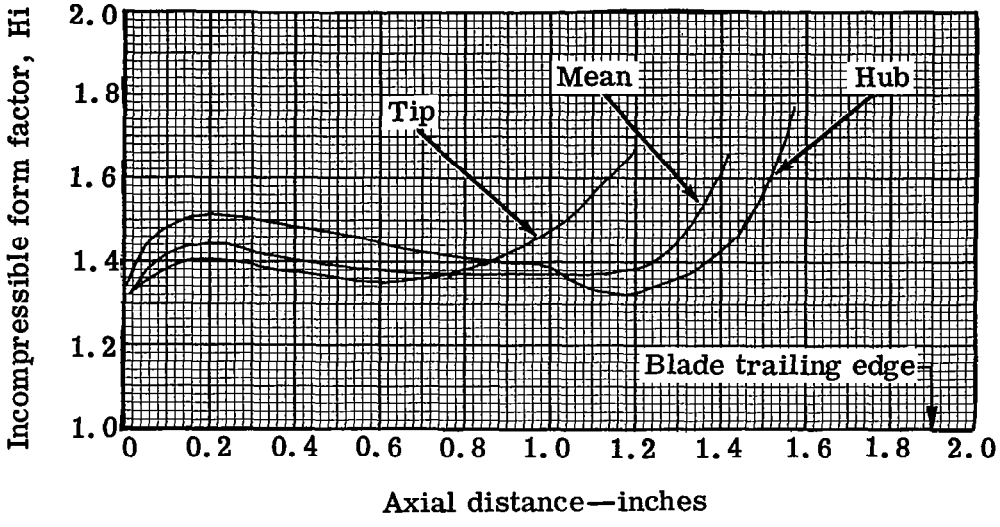

Figure 51. Jet-flap rotor-blade suction surface incompressible form factor for blade without jet-flap.

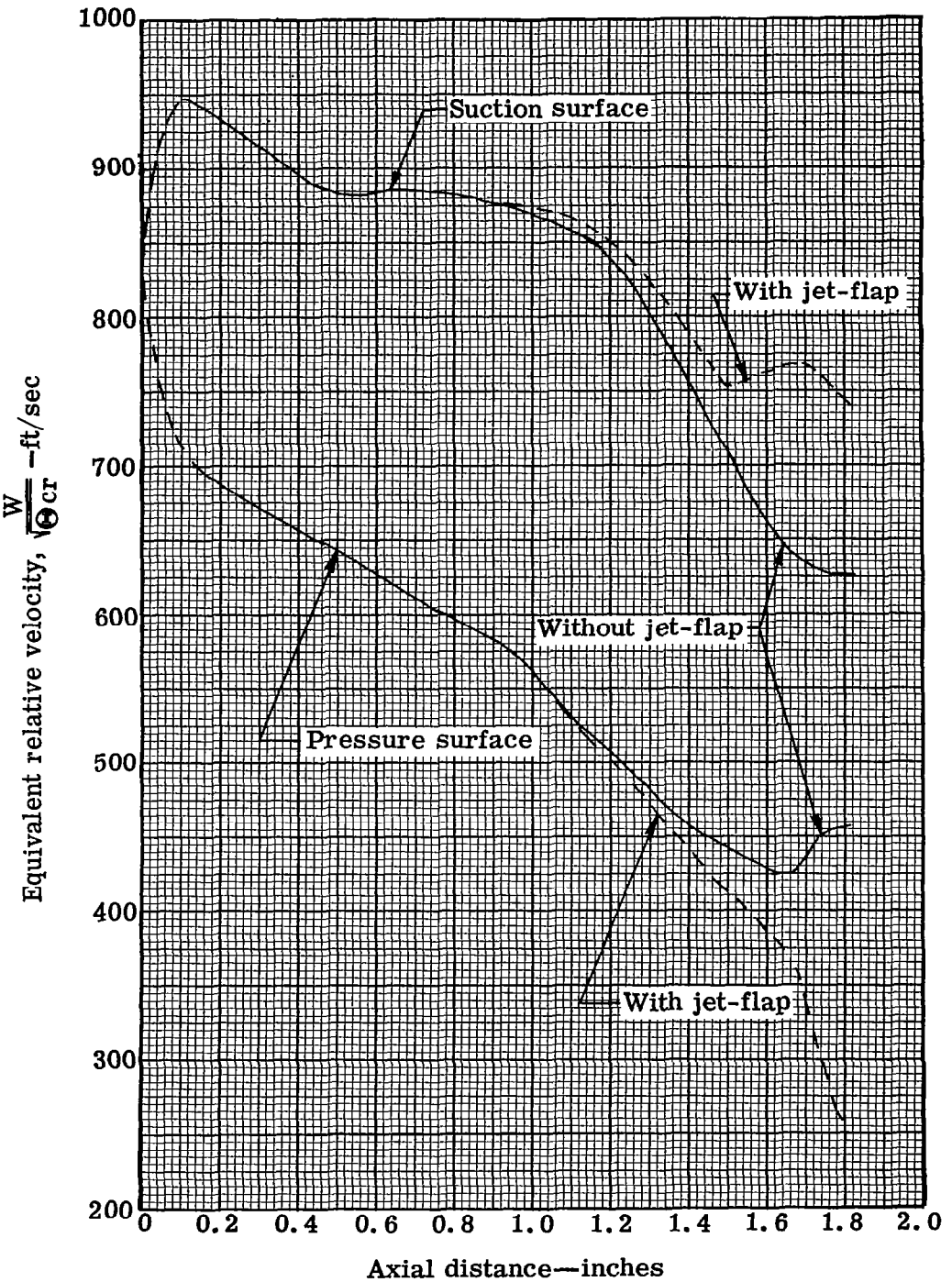

Figure 52. Jet-flap rotor-blade hub section surface equivalent velocity distribution with and without jet-flap based on incompressible two-dimensional solution.

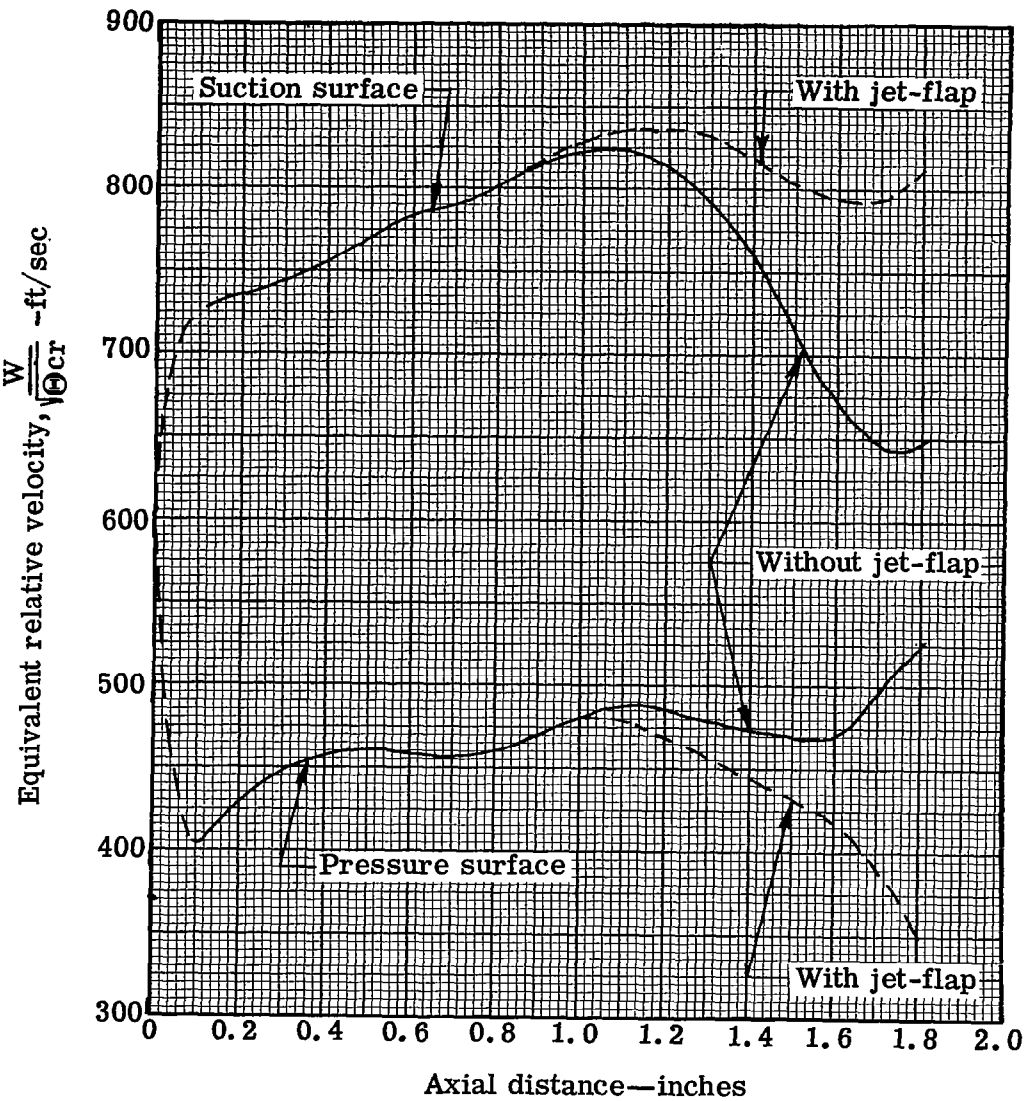

Figure 53. Jet-flap rotor-blade mean section surface equivalent velocity distribution with and without jet-flap based on incompressible two-dimensional solution.

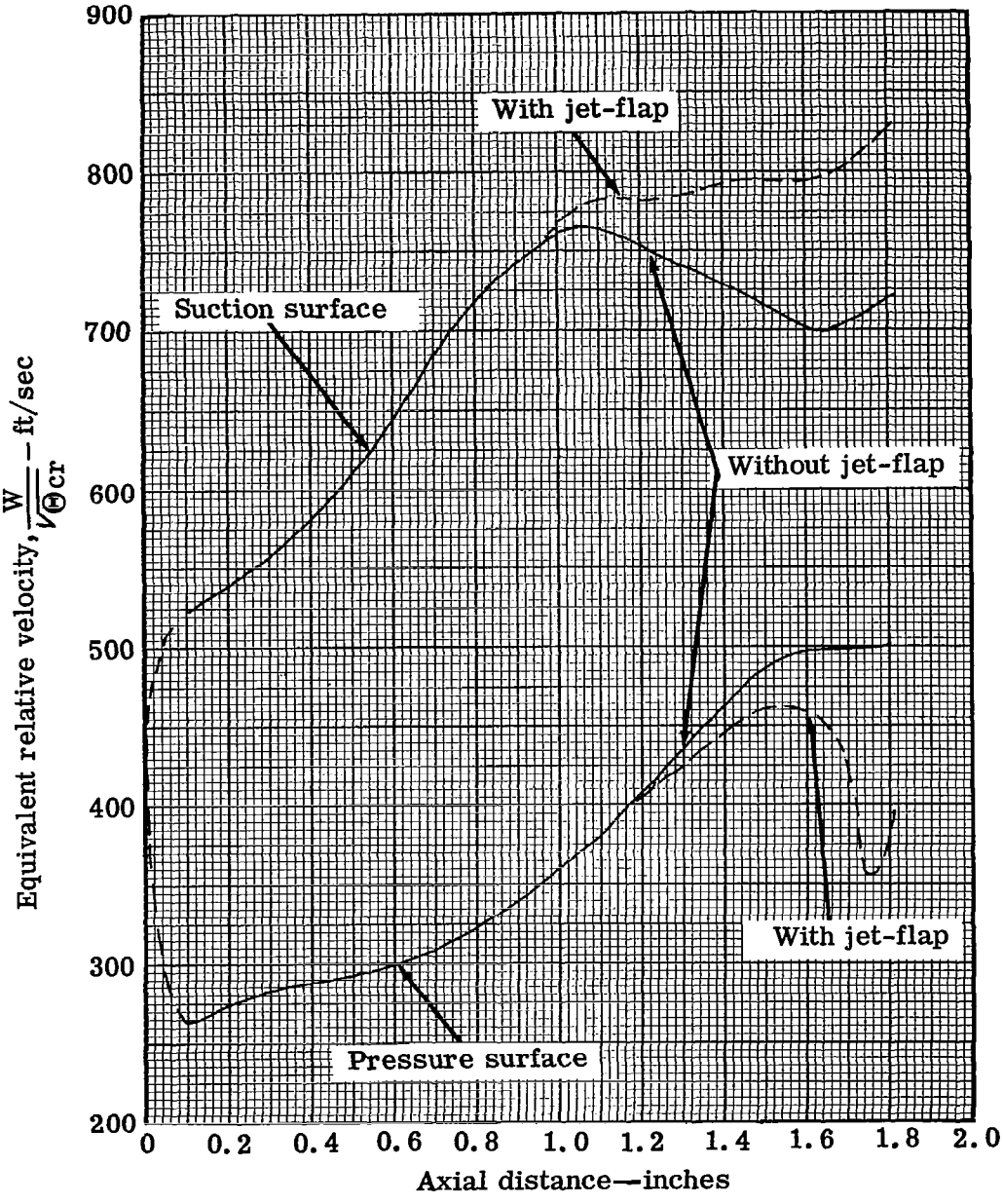

Figure 54. Jet-flap rotor-blade tip section surface equivalent velocity distribution with and without jet-flap based on incompressible two-dimensional solution.

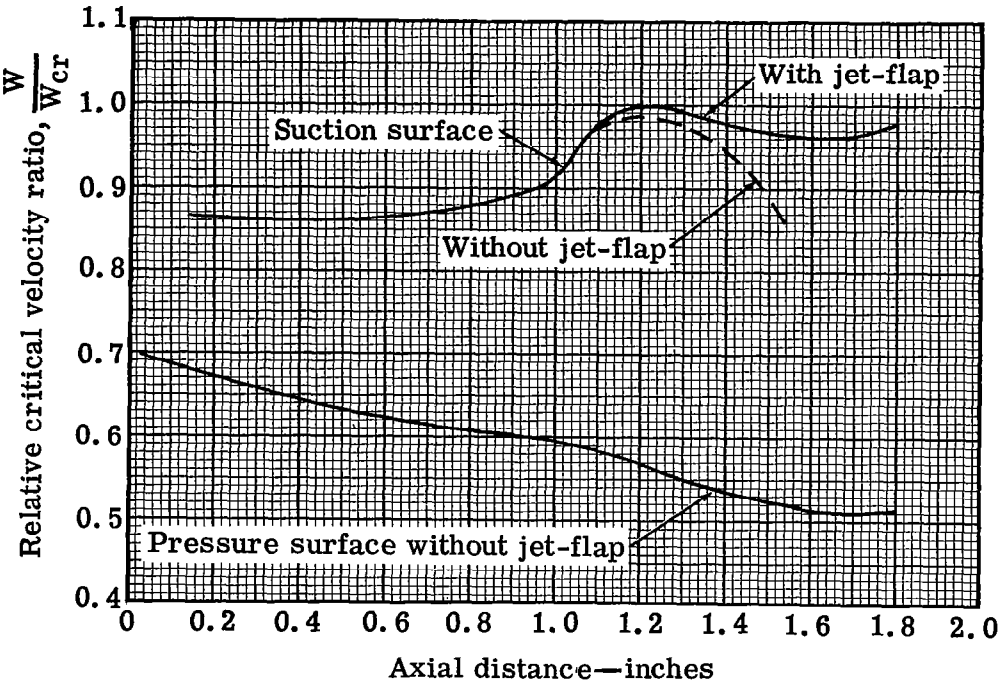

Figure 55. Jet-flap rotor-blade hub section surface relative critical velocity ratio distribution with and without jet-flap.

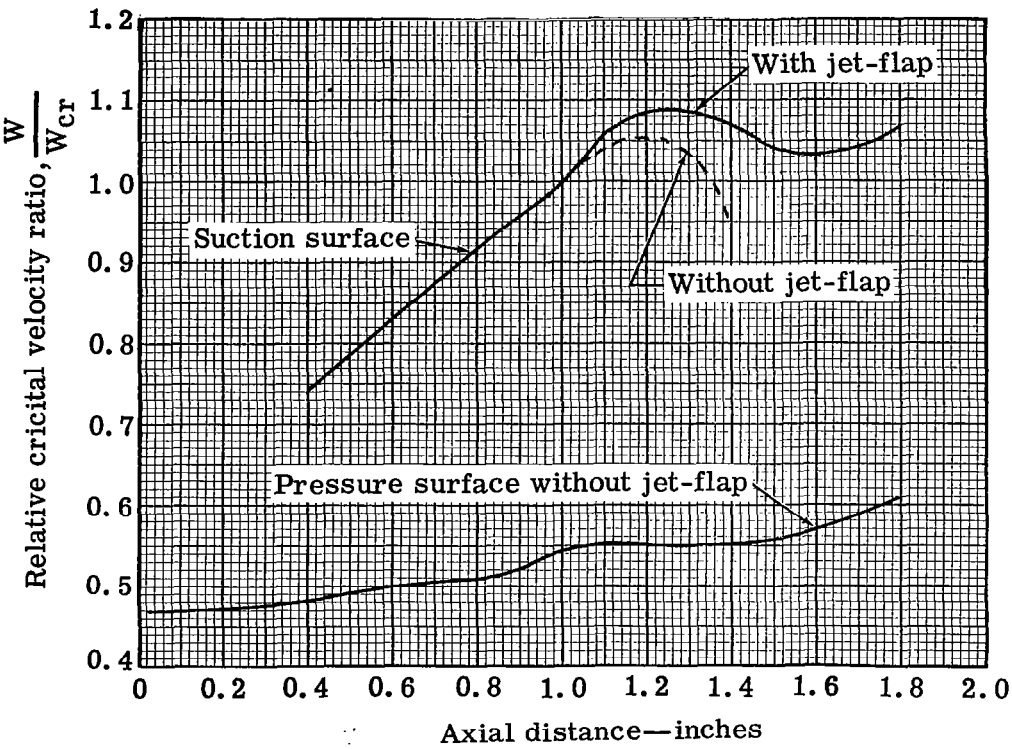

Figure 56. Jet-flap rotor-blade mean section surface relative critical velocity ratio distribution with and without jet-flap.

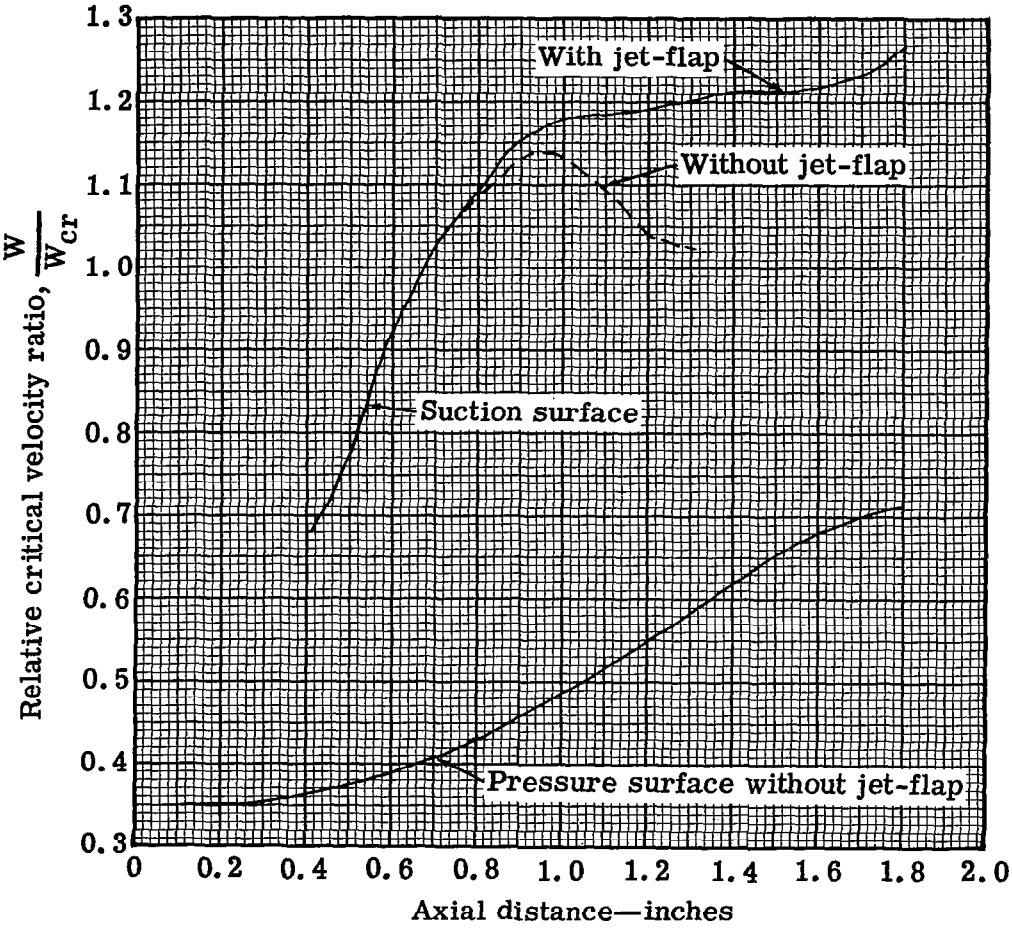

Figure 57. Jet-flap rotor-blade tip section surface relative critical velocity ratio distribution with and without jet-flap.

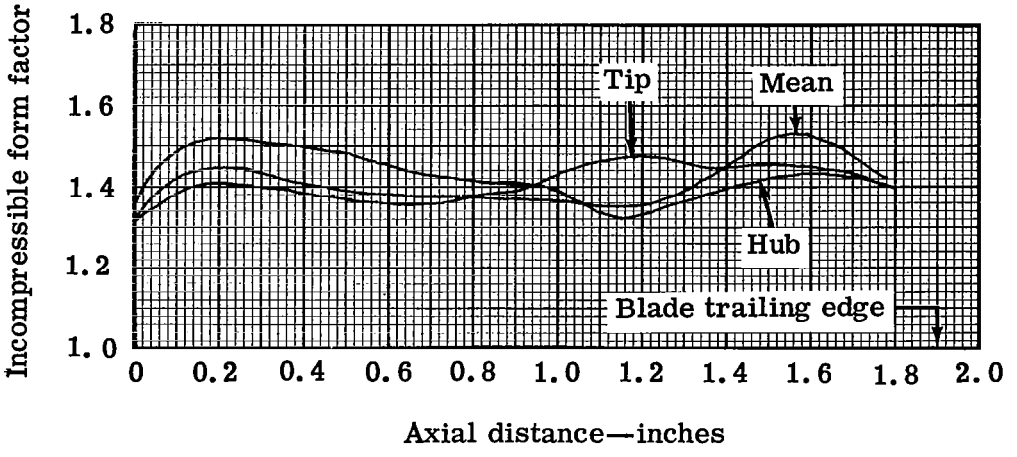

Figure 58. Jet-flap rotor-blade suction surface incompressible form factor with jet-flap.

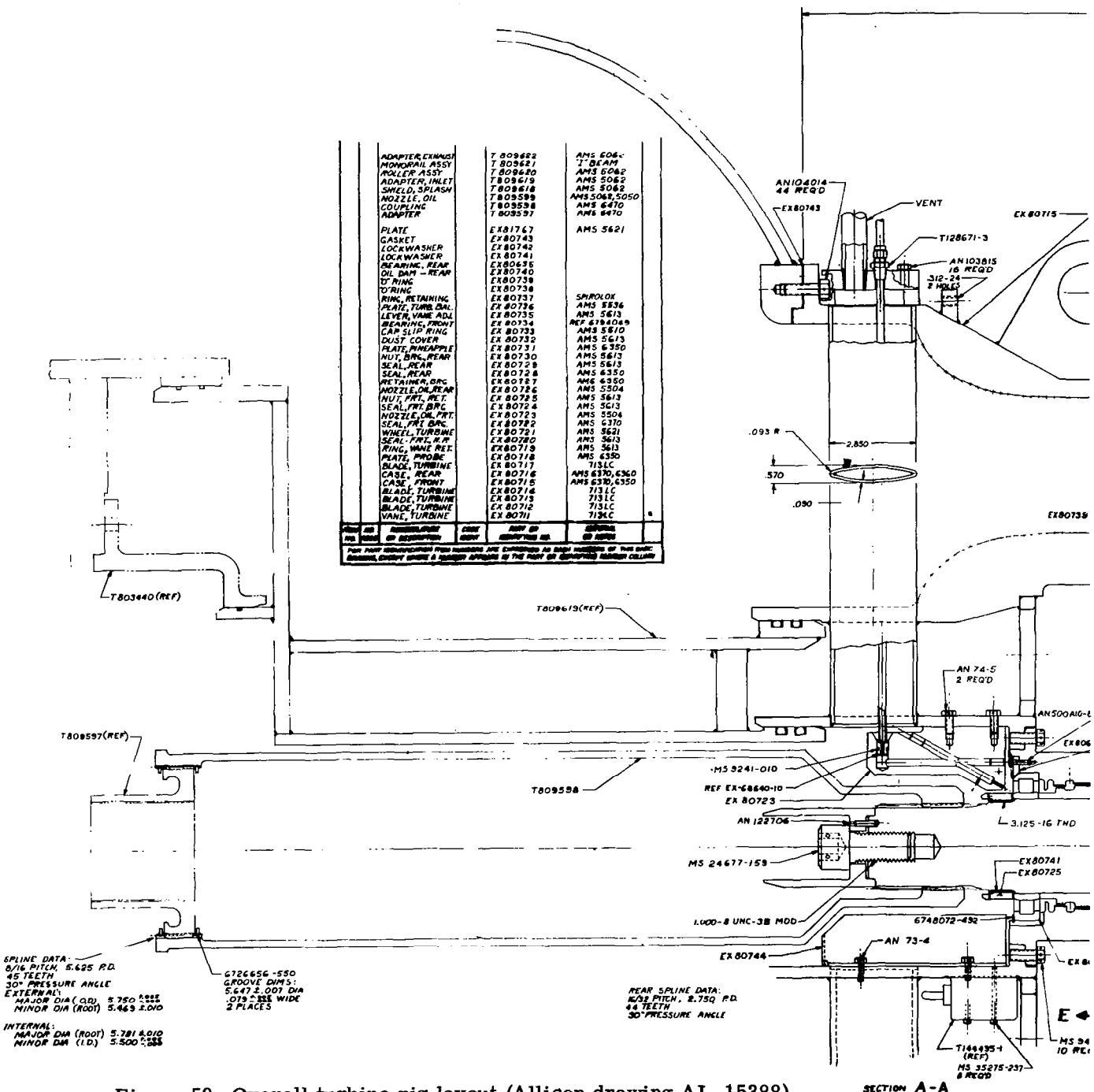

Figure 59. Overall turbine rig layout (Allison drawing AL-15388).

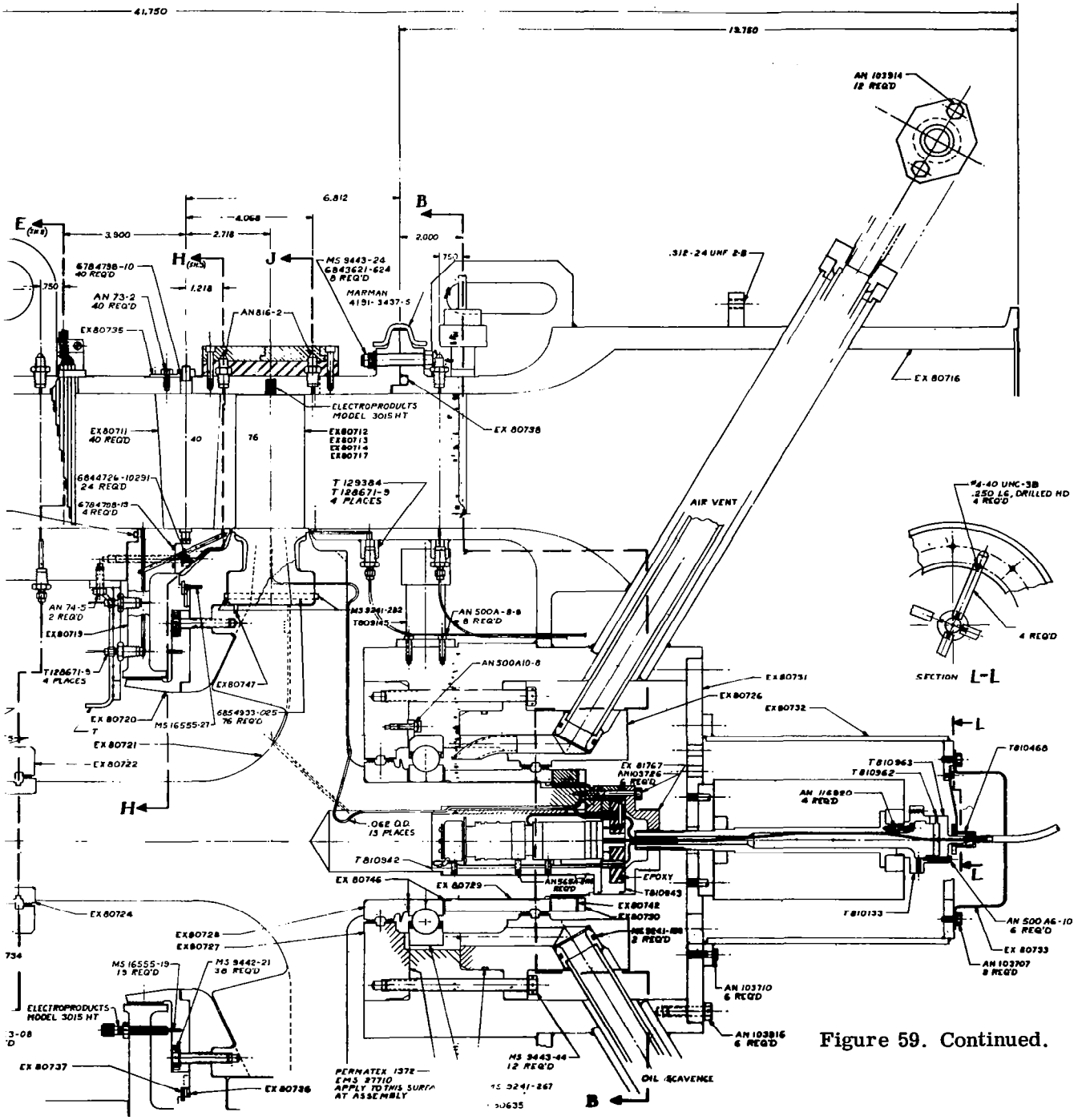

Figure 59. Continued.

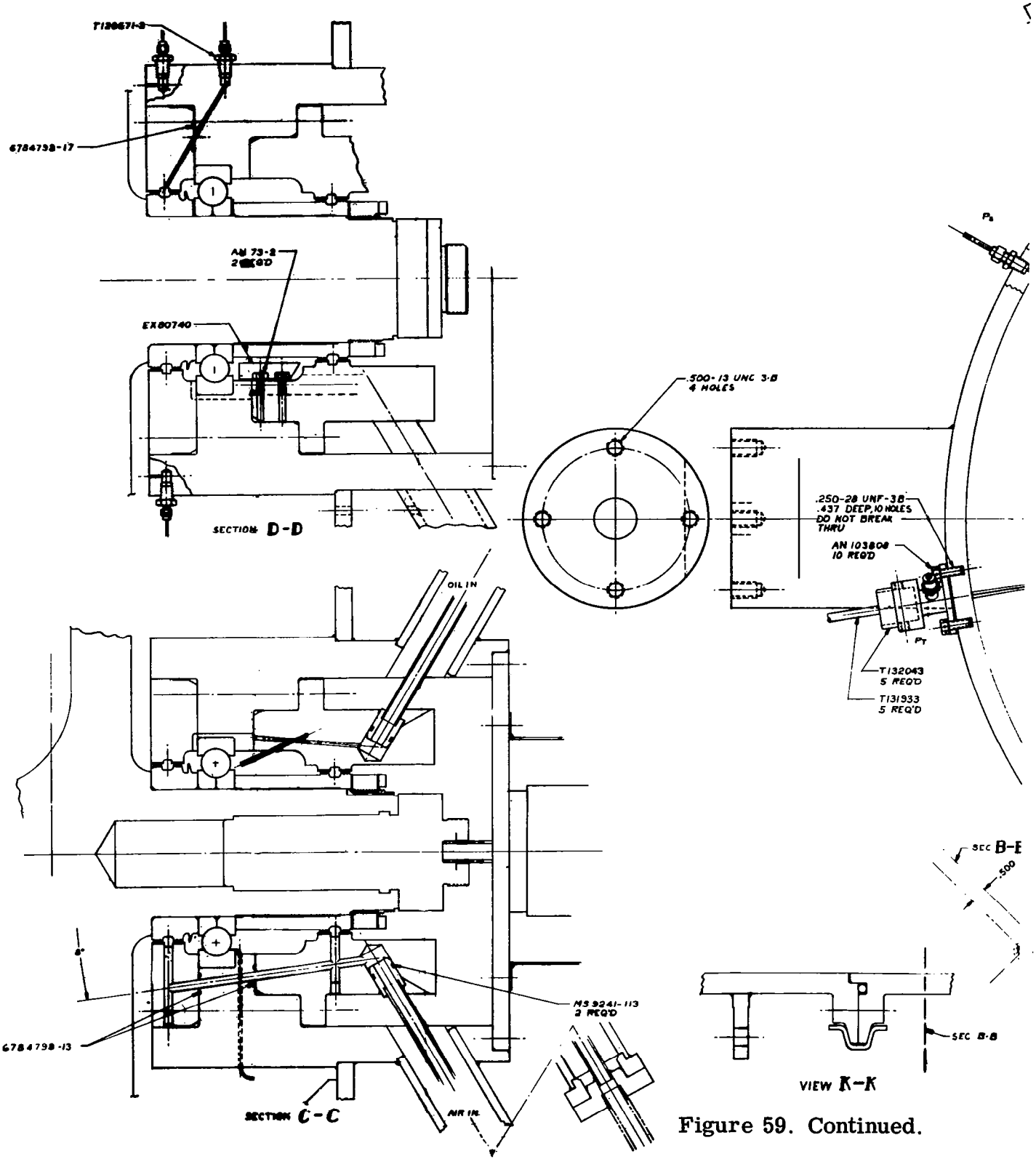

Figure 59. Continued.

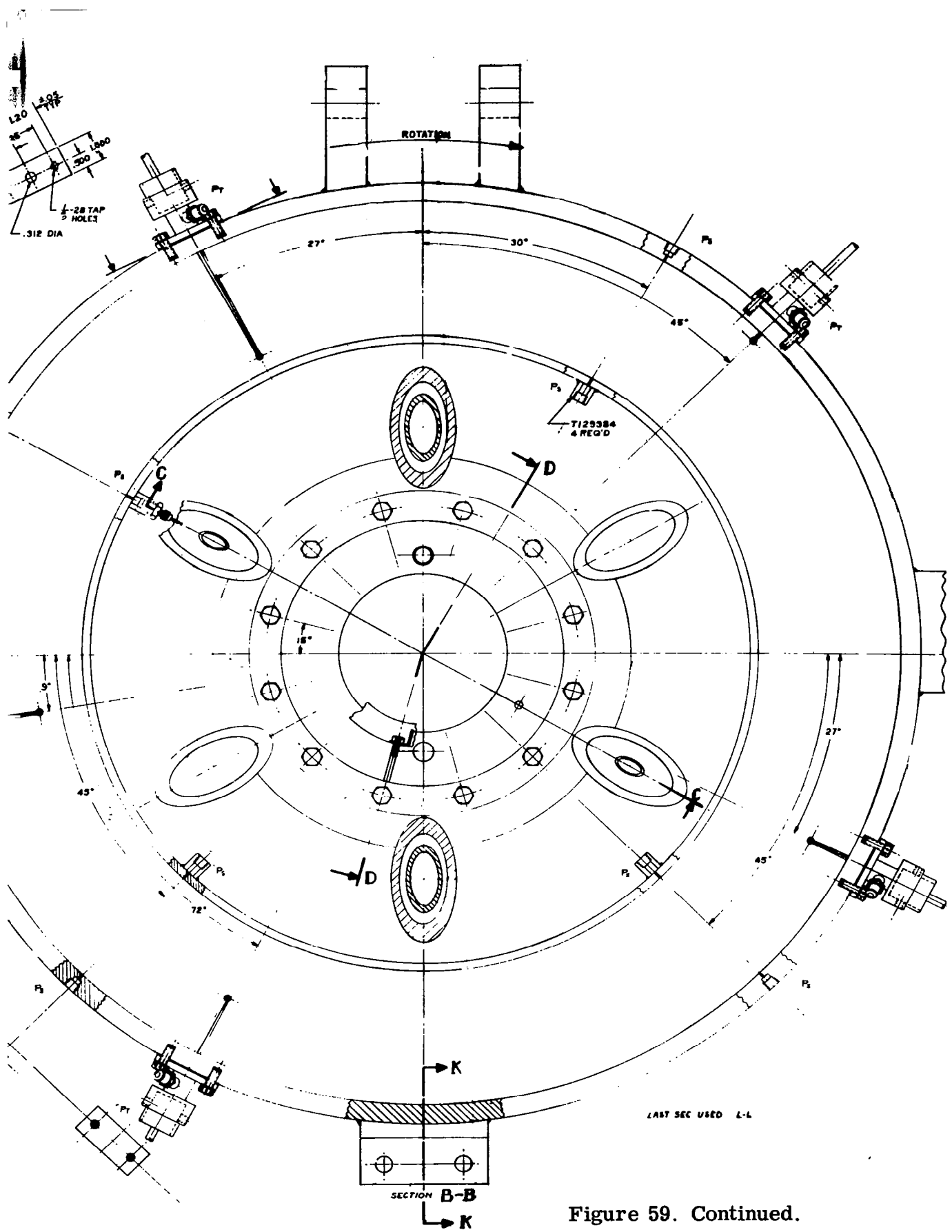

Figure 59. Continued.

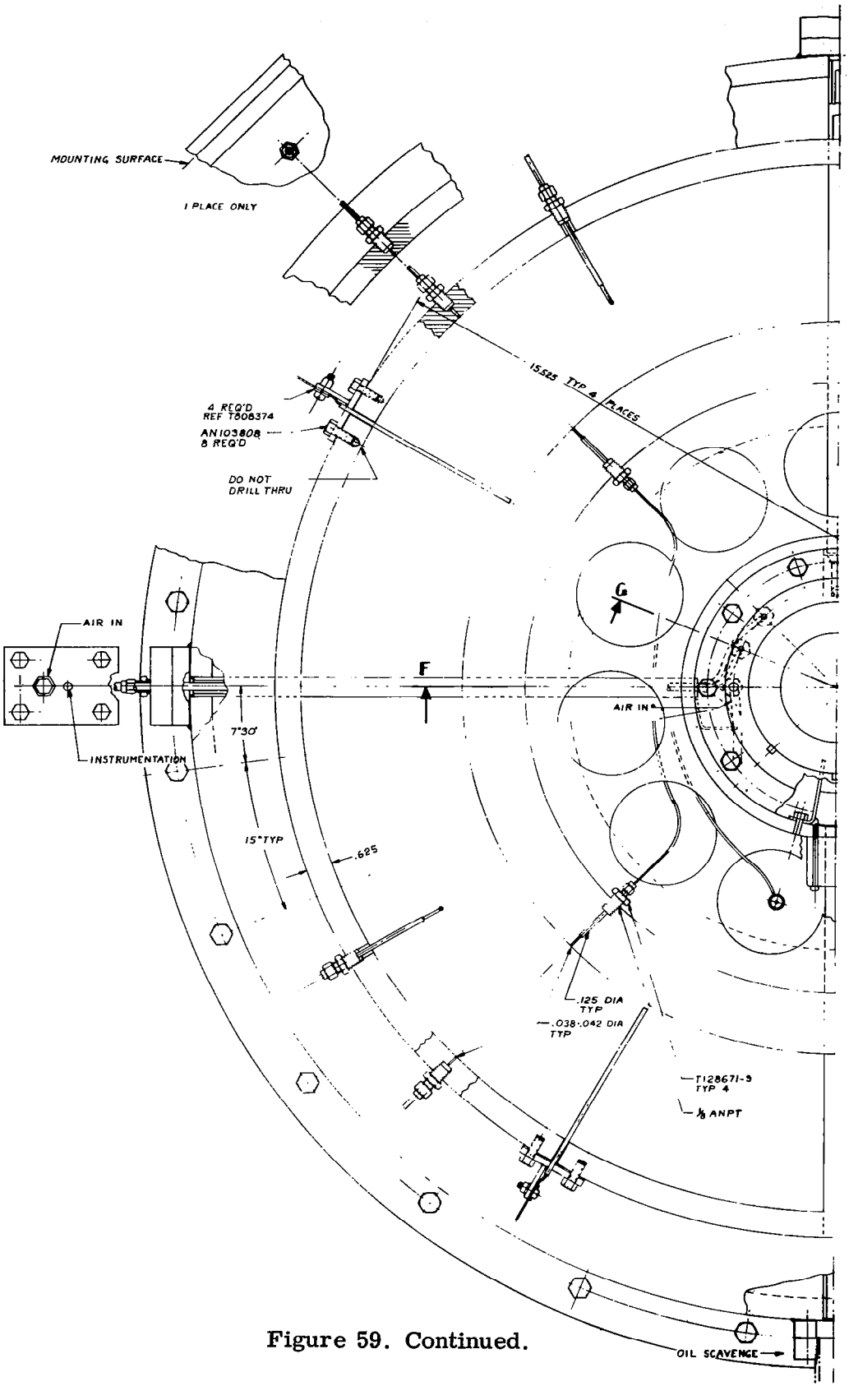

Figure 59. Continued.

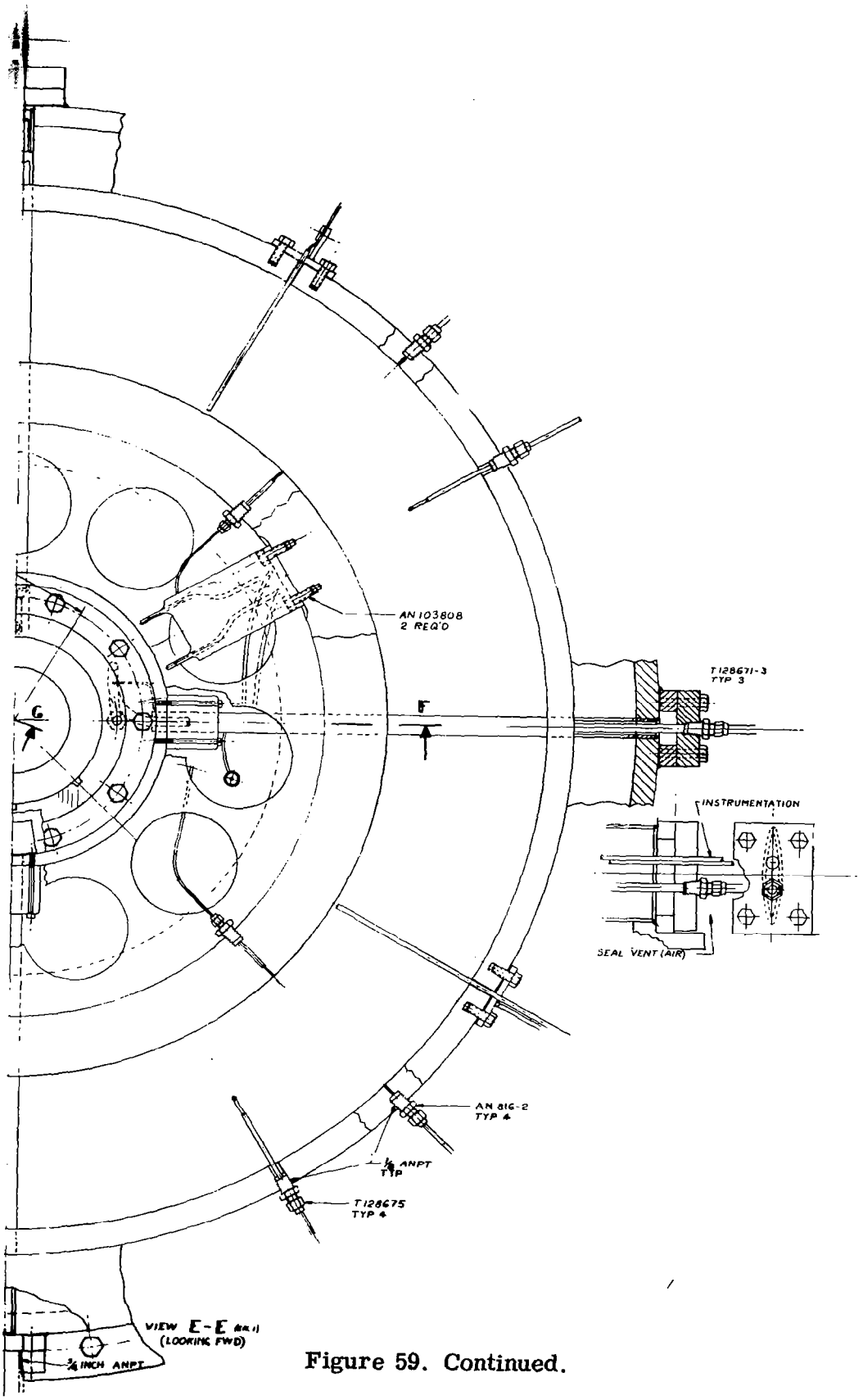

Figure 59. Continued.

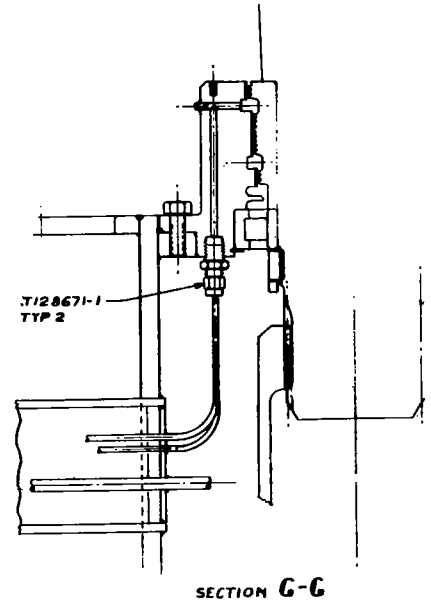

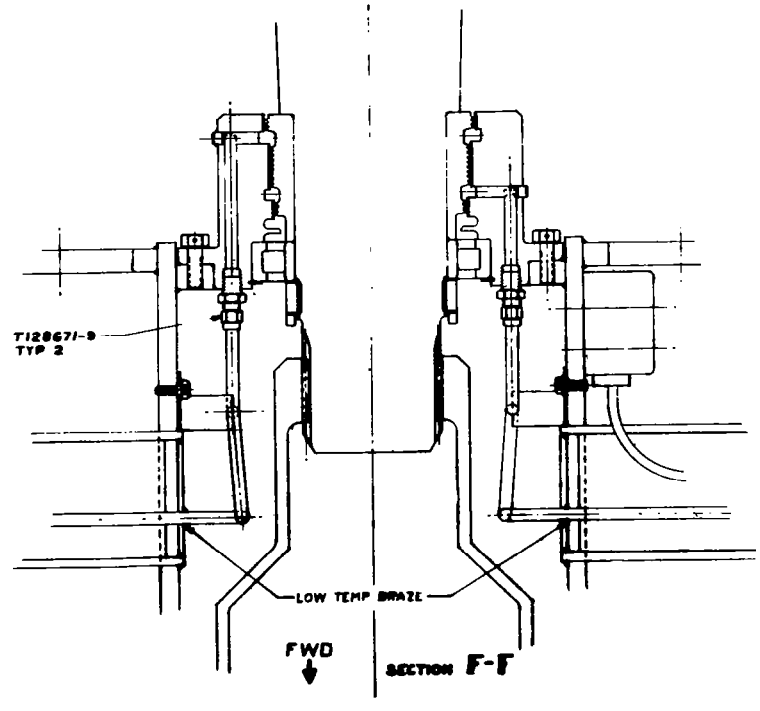

Figure 59. Continued.

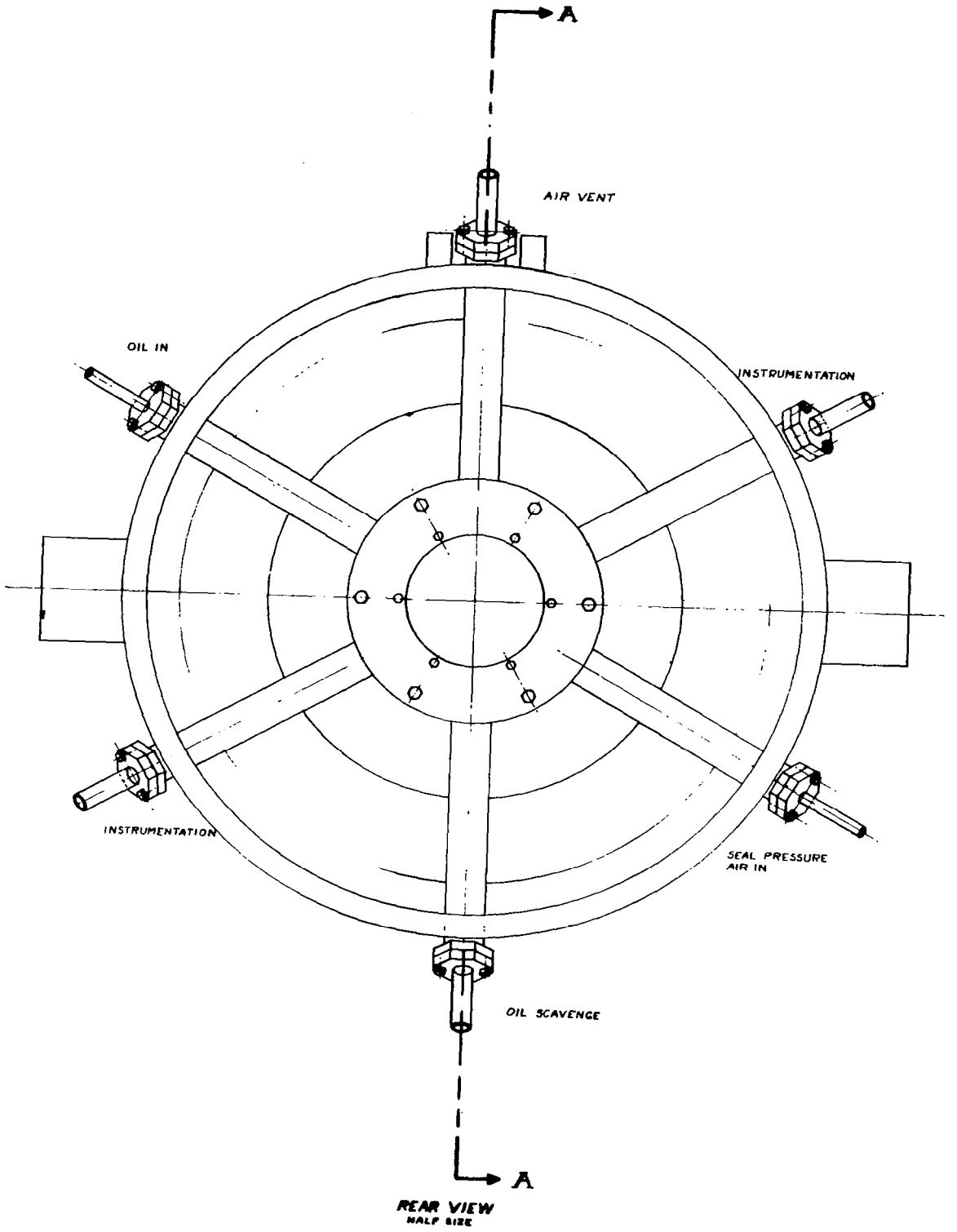

Figure 59. Continued.

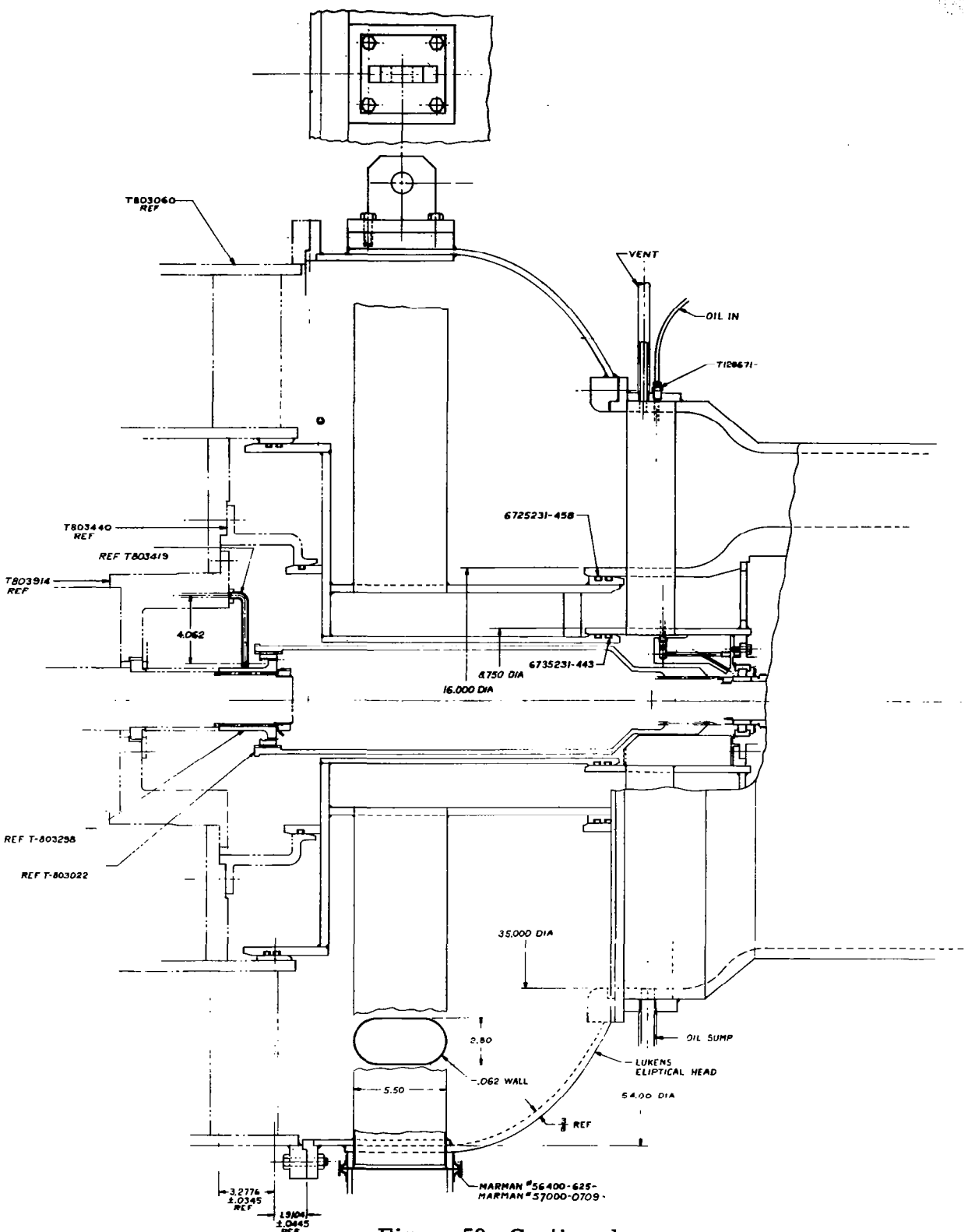

Figure 59. Continued.

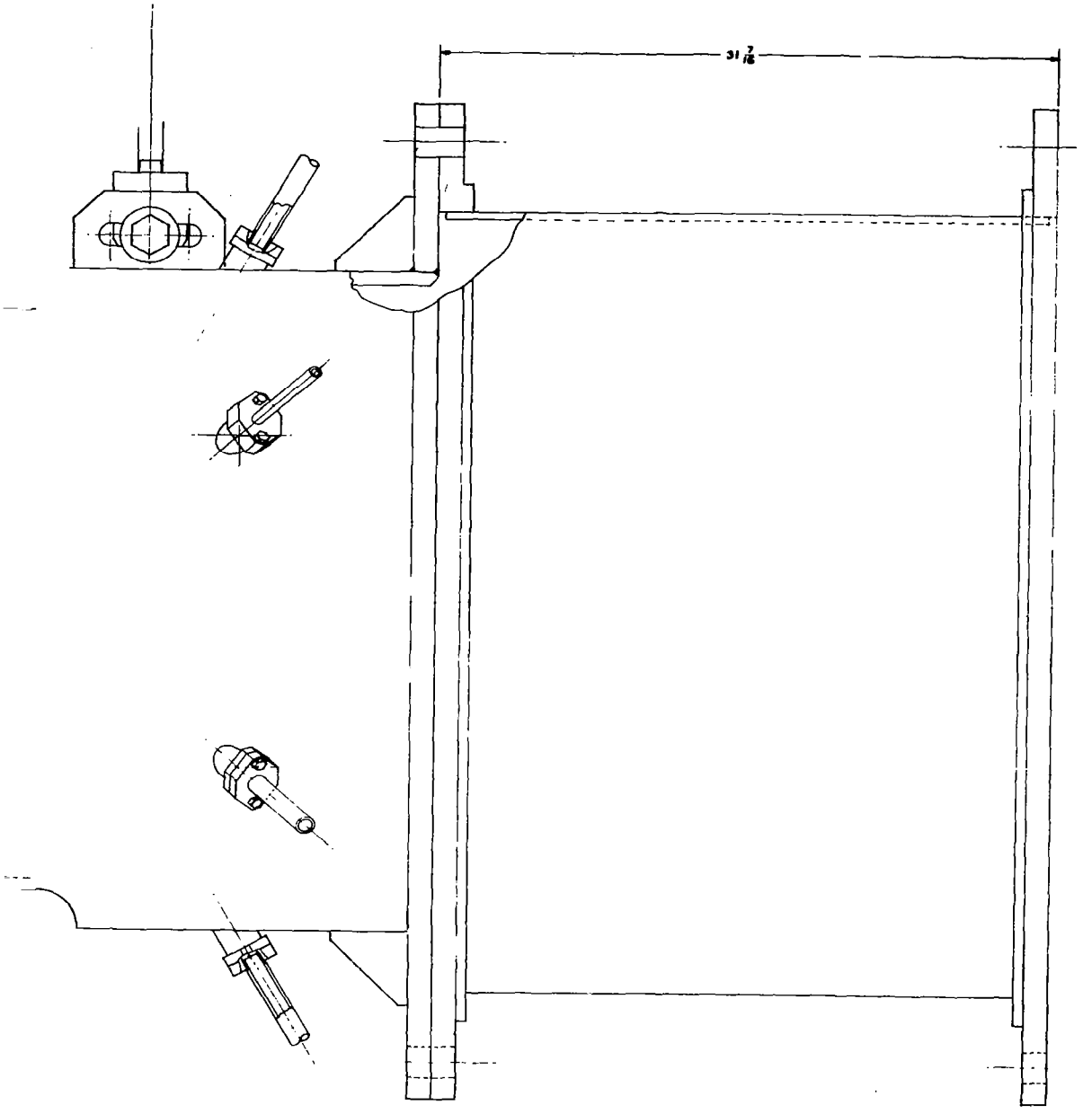

Figure 59. Continued.

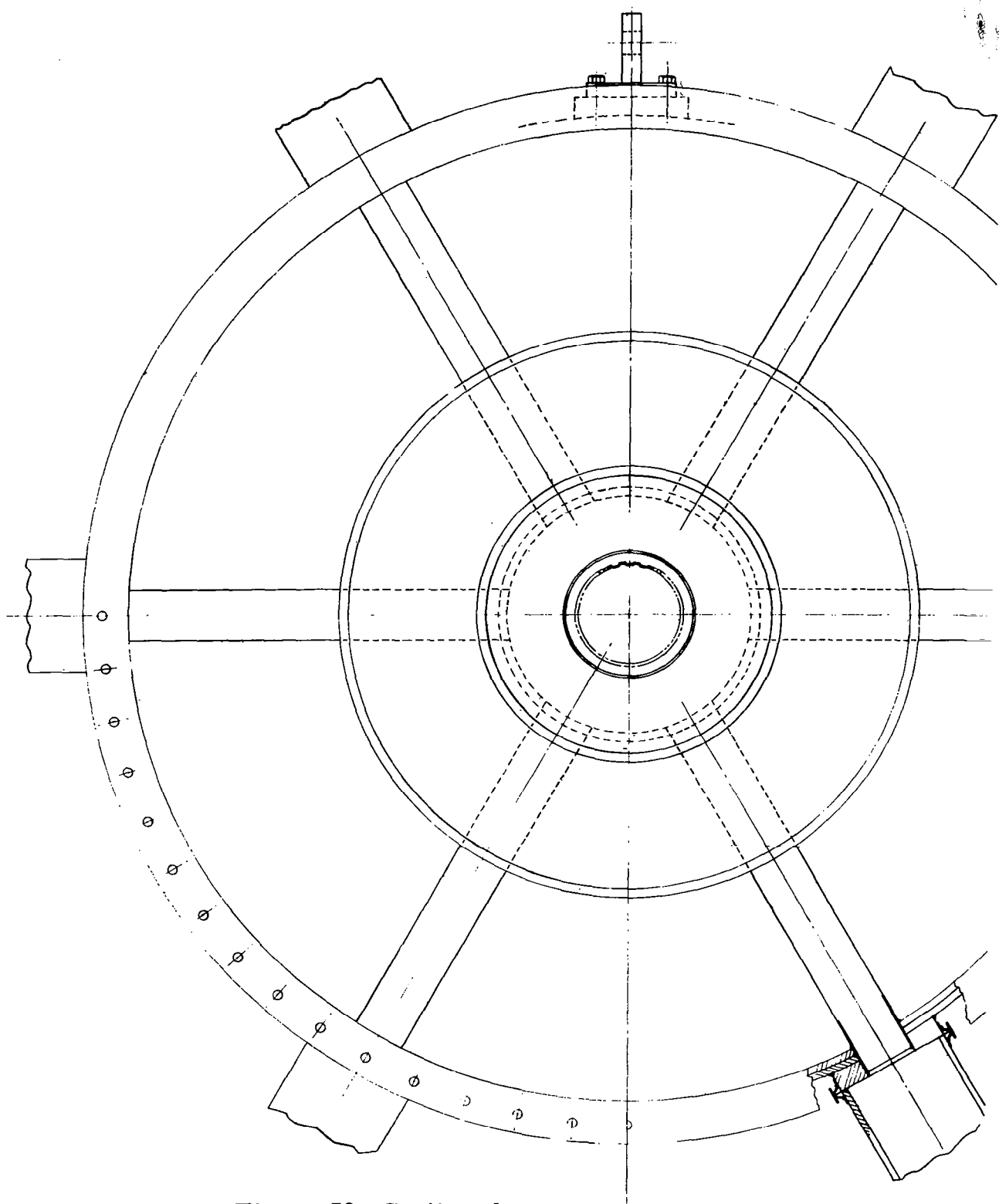

Figure 59. Continued.

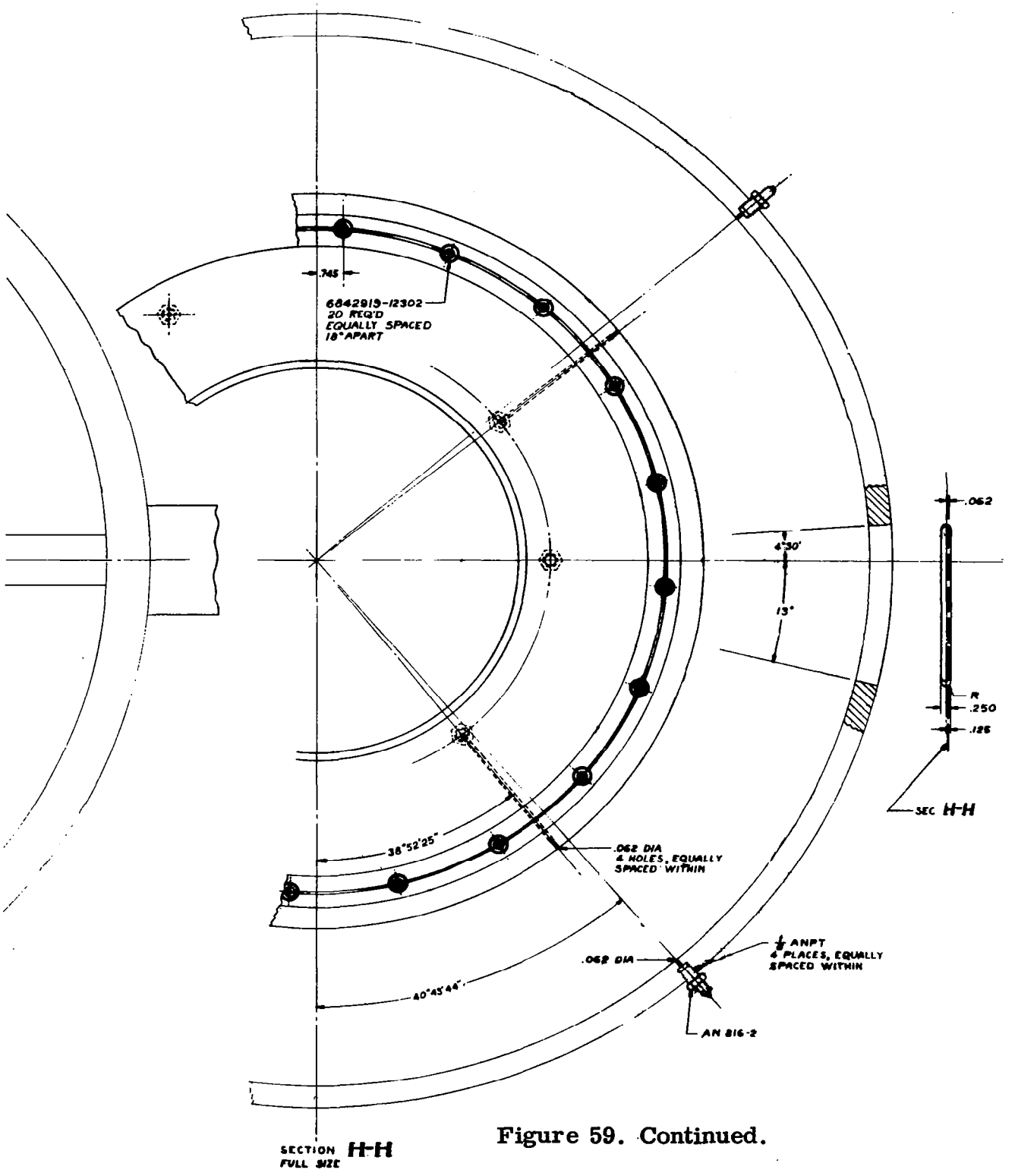

Figure 59. Continued.

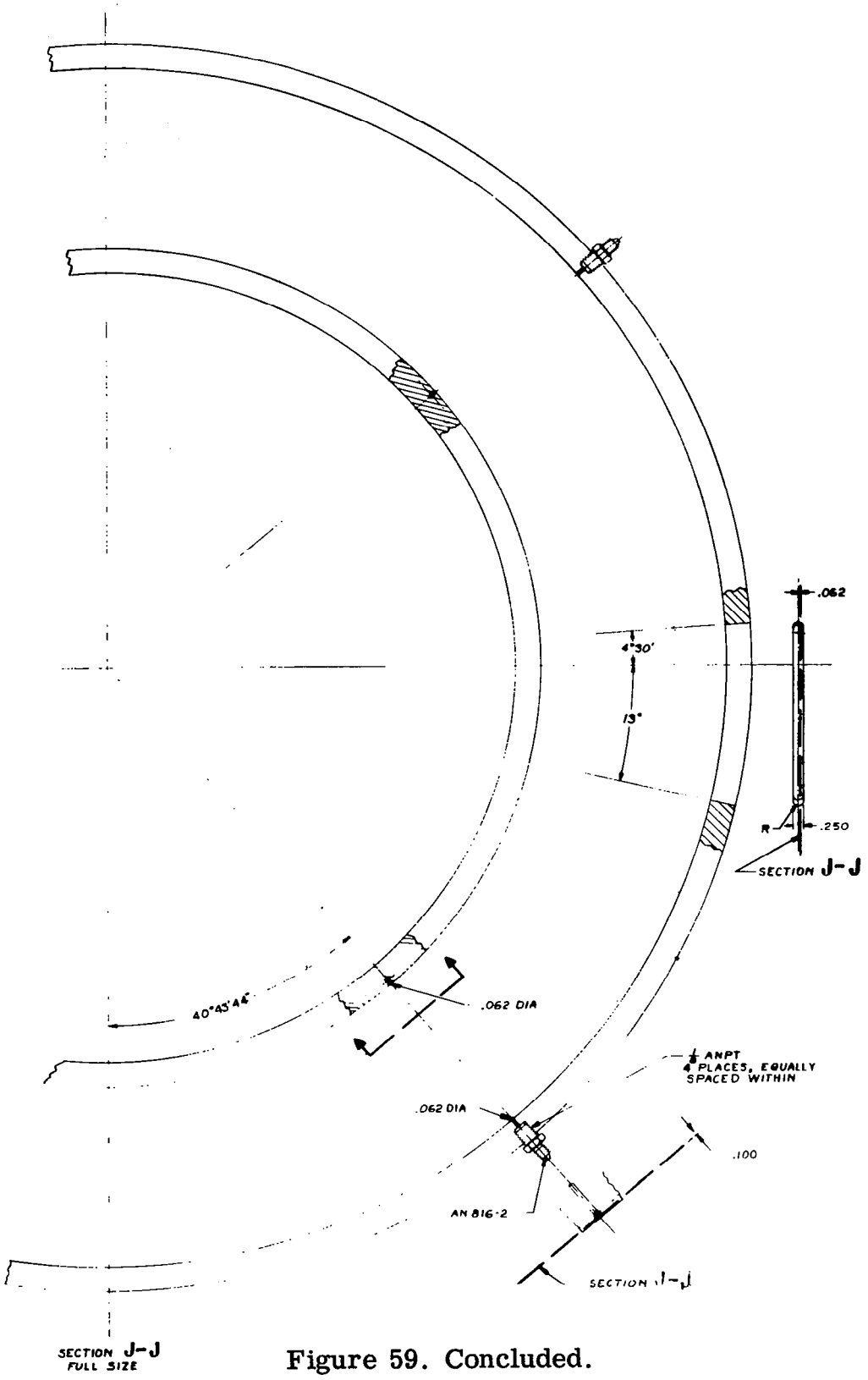

Figure 59. Concluded.

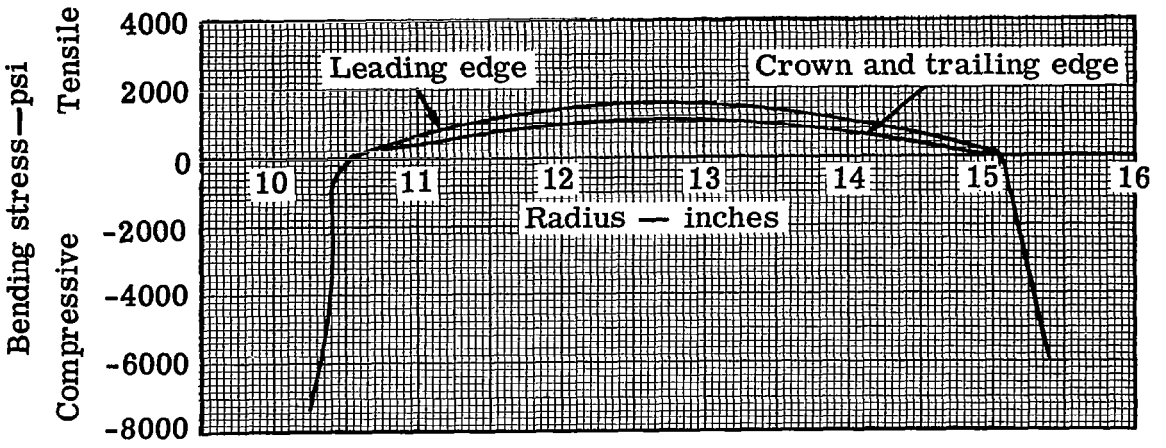

(a) Stator - blade bending stress

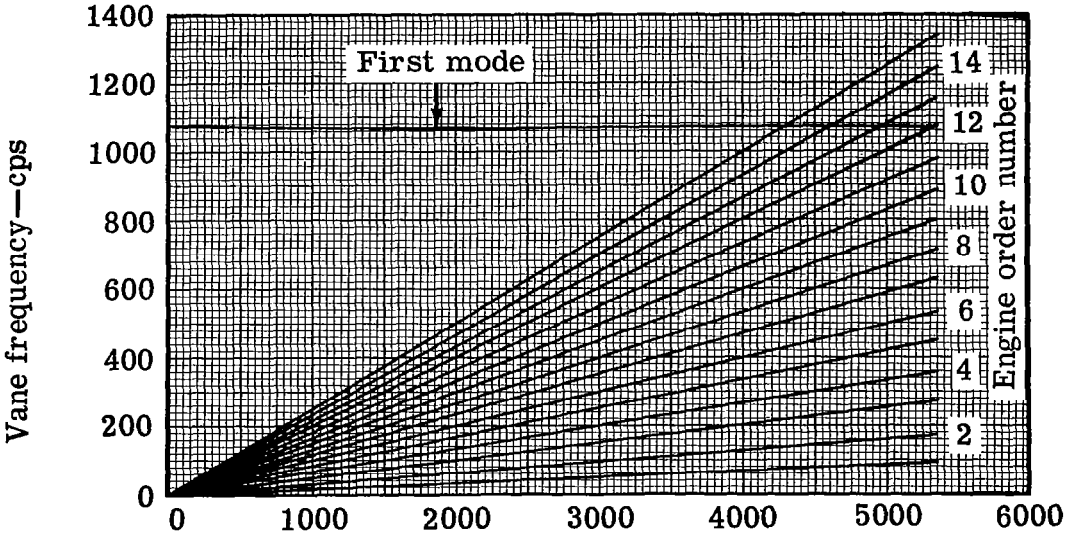

(b) Stator - blade natural frequency characteristics

Figure 60. Stator-blade bending stress and natural frequency characteristics.

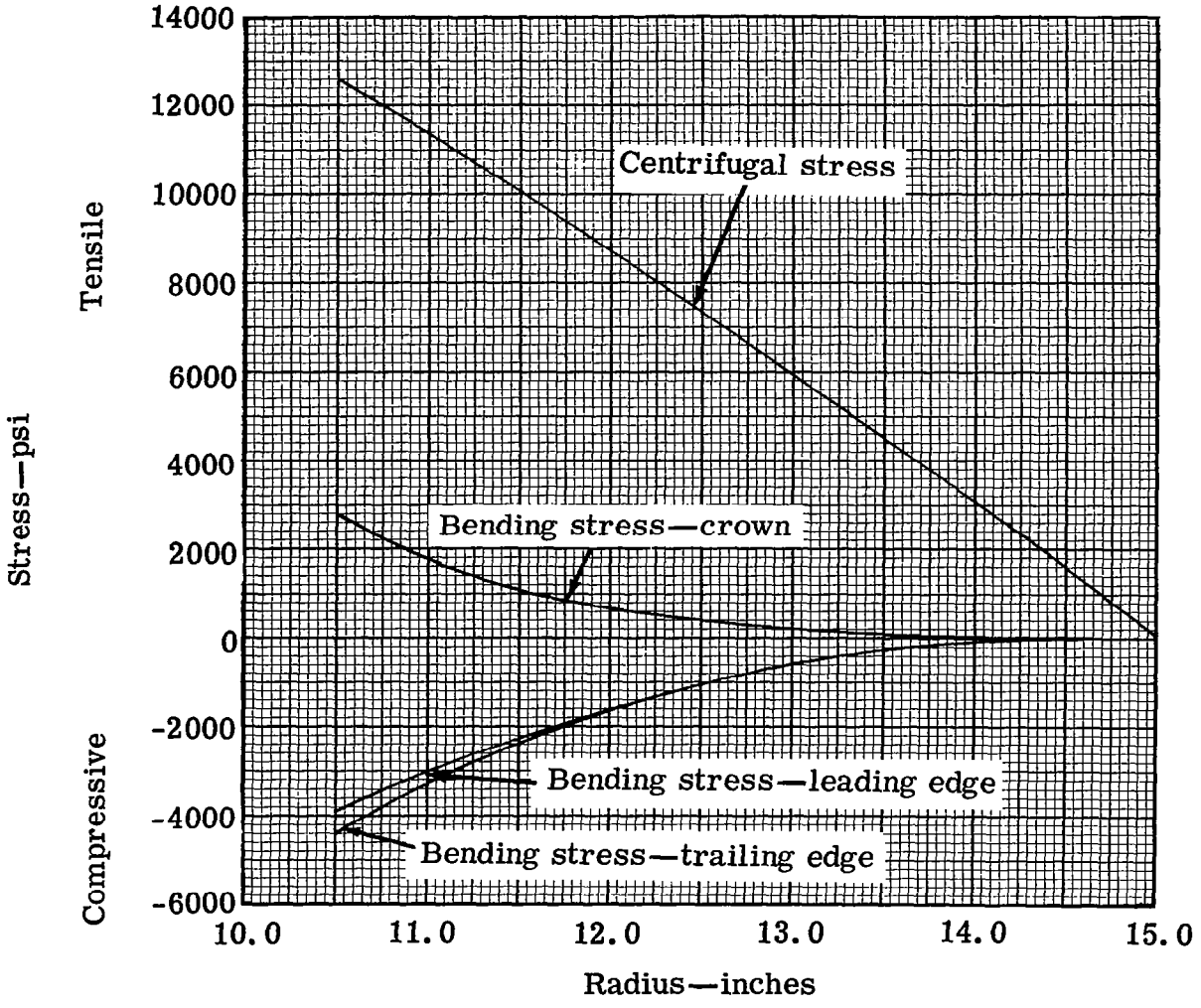

Figure 61. Plain rotor-blade bending and centrifugal stress characteristics, 100 percent design speed.

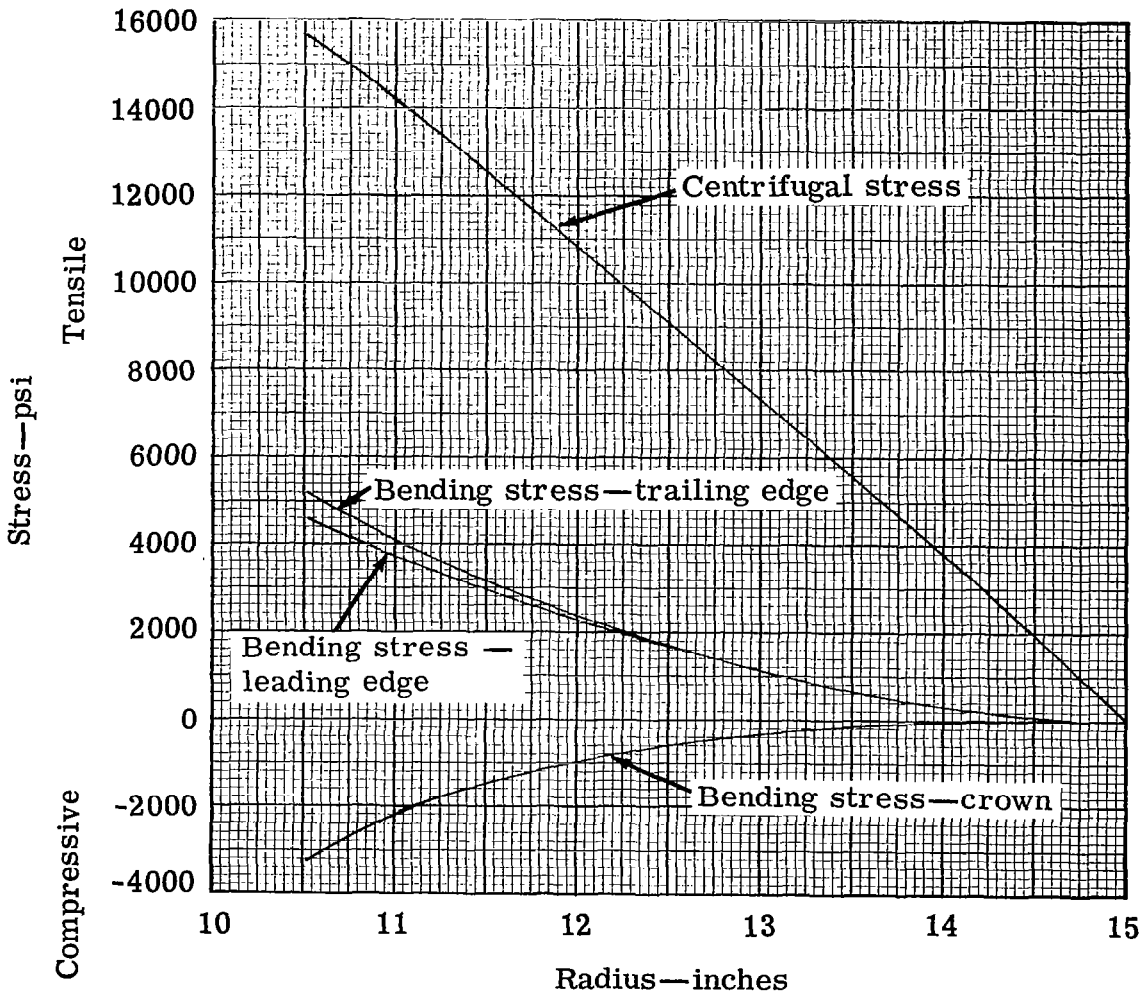

Figure 62. Plain rotor-blade bending and centrifugal stress characteristics, *110 percent design speed.*

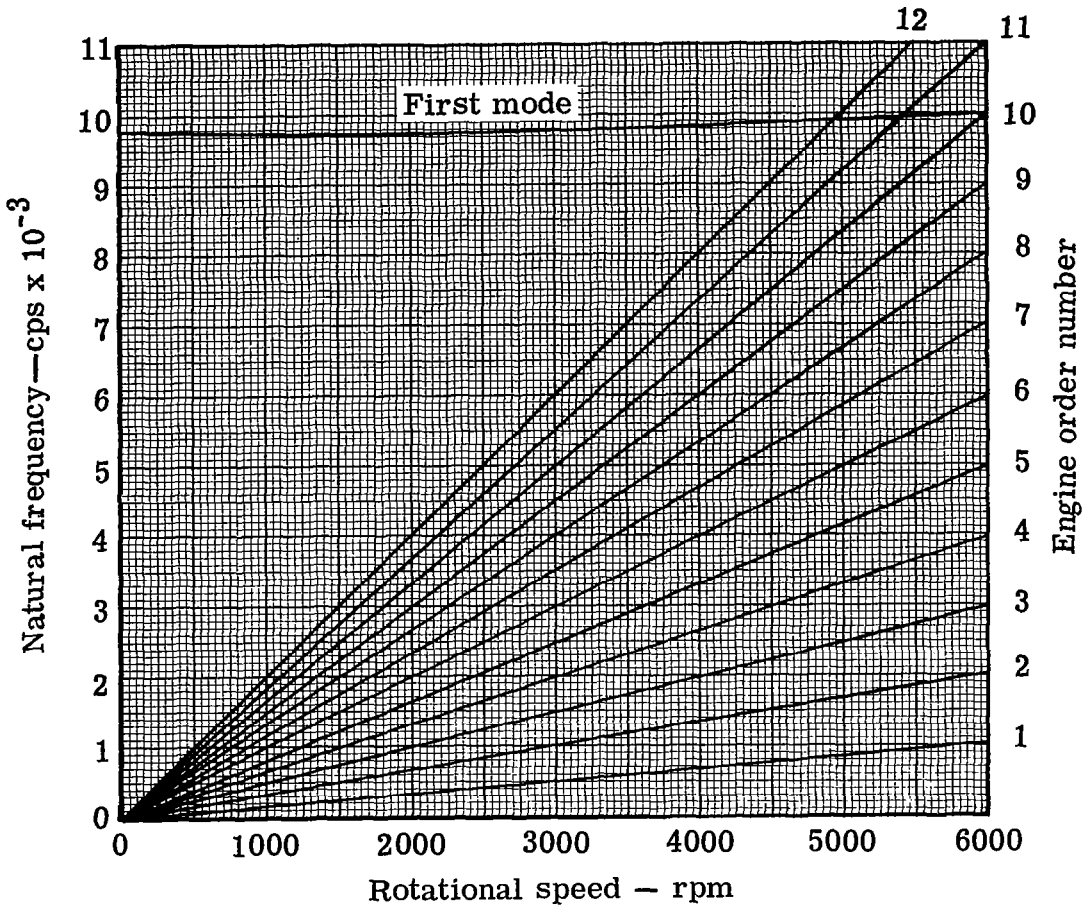

Figure 63. Plain rotor-blade natural frequency characteristics.

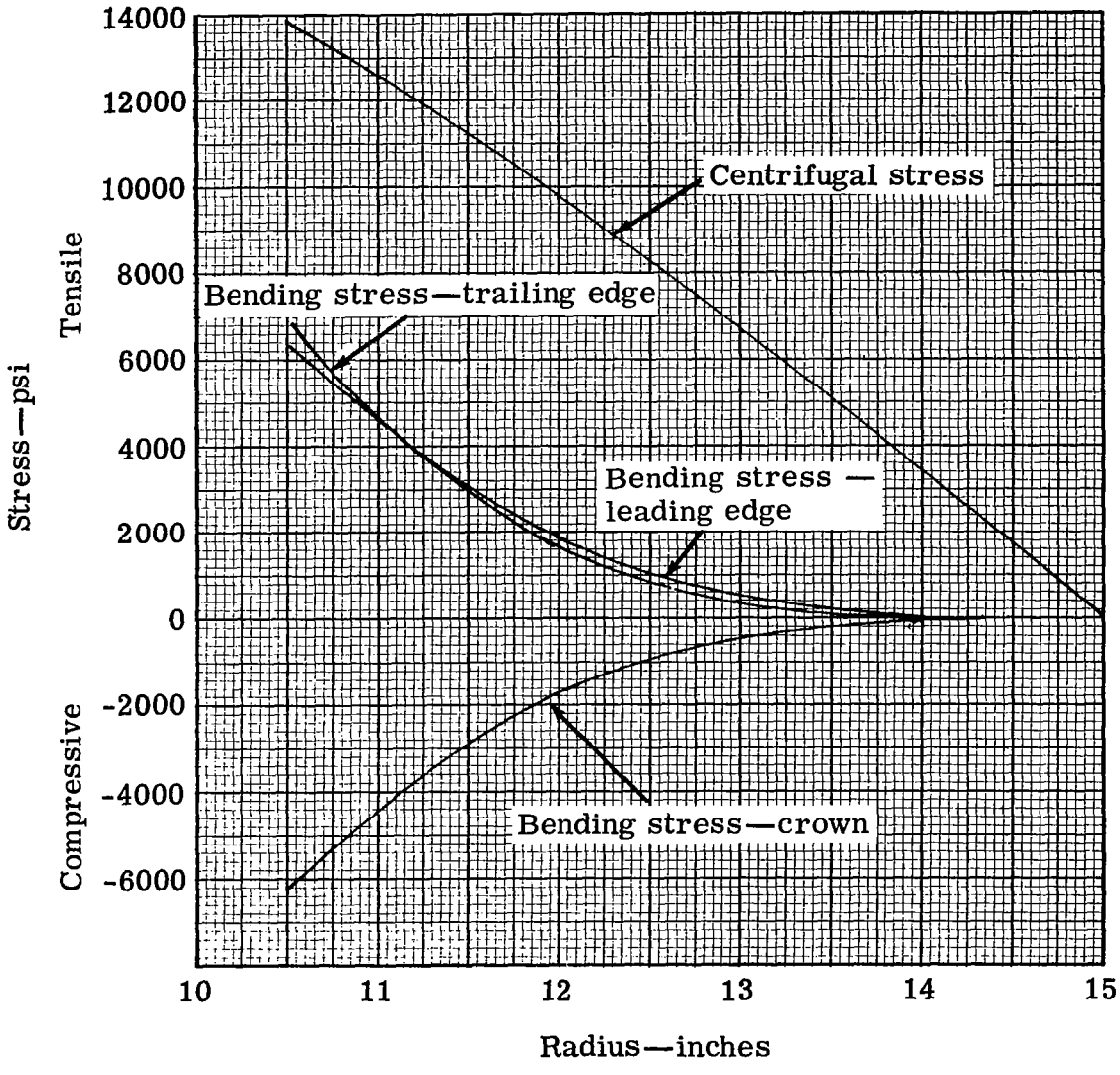

Figure 64. Tangential slot blowing blade centrifugal and bending stress characteristics, 100 percent design speed.

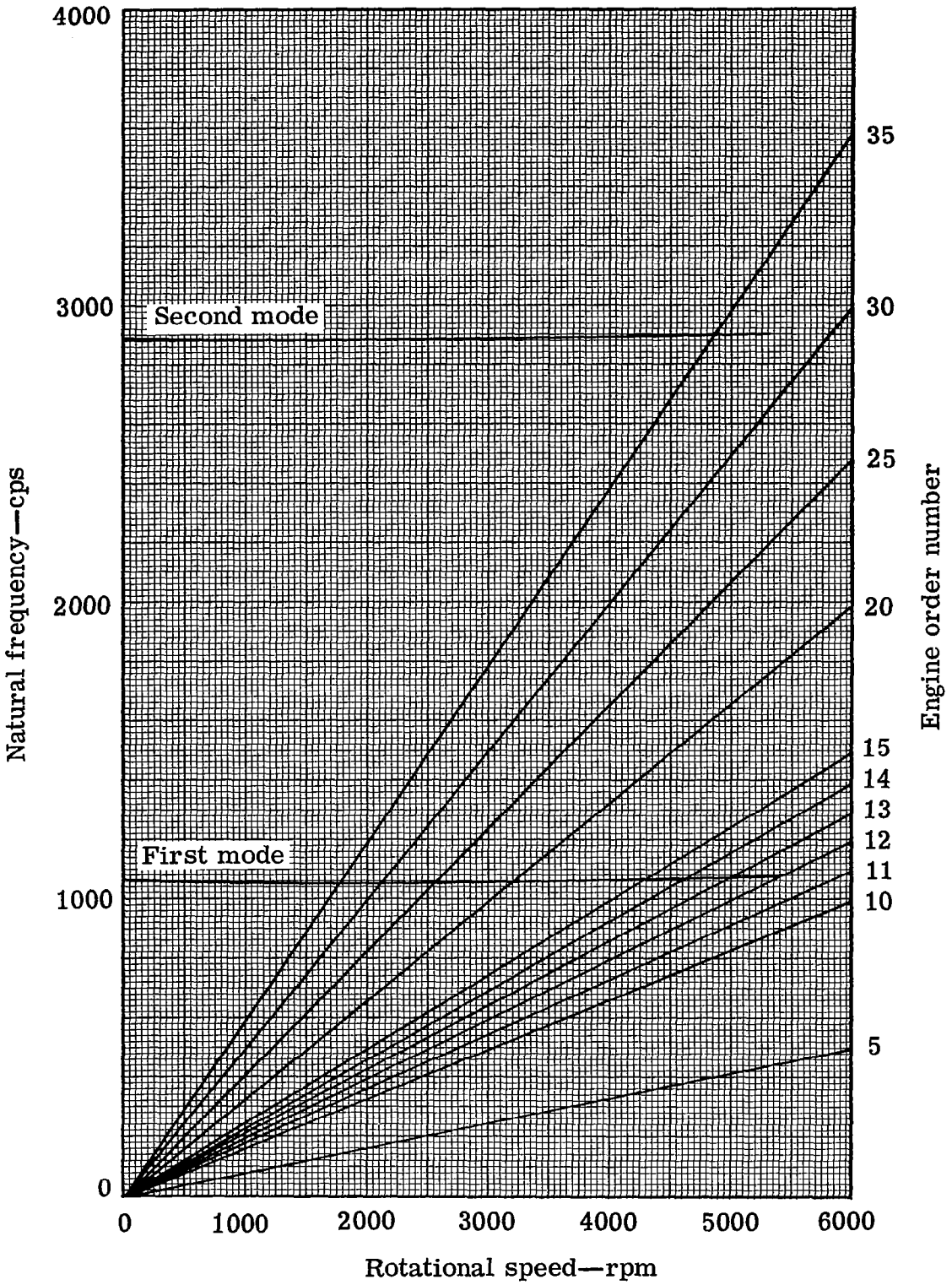

Figure 65. Tangential slot blowing rotor-blade natural frequency characteristics.

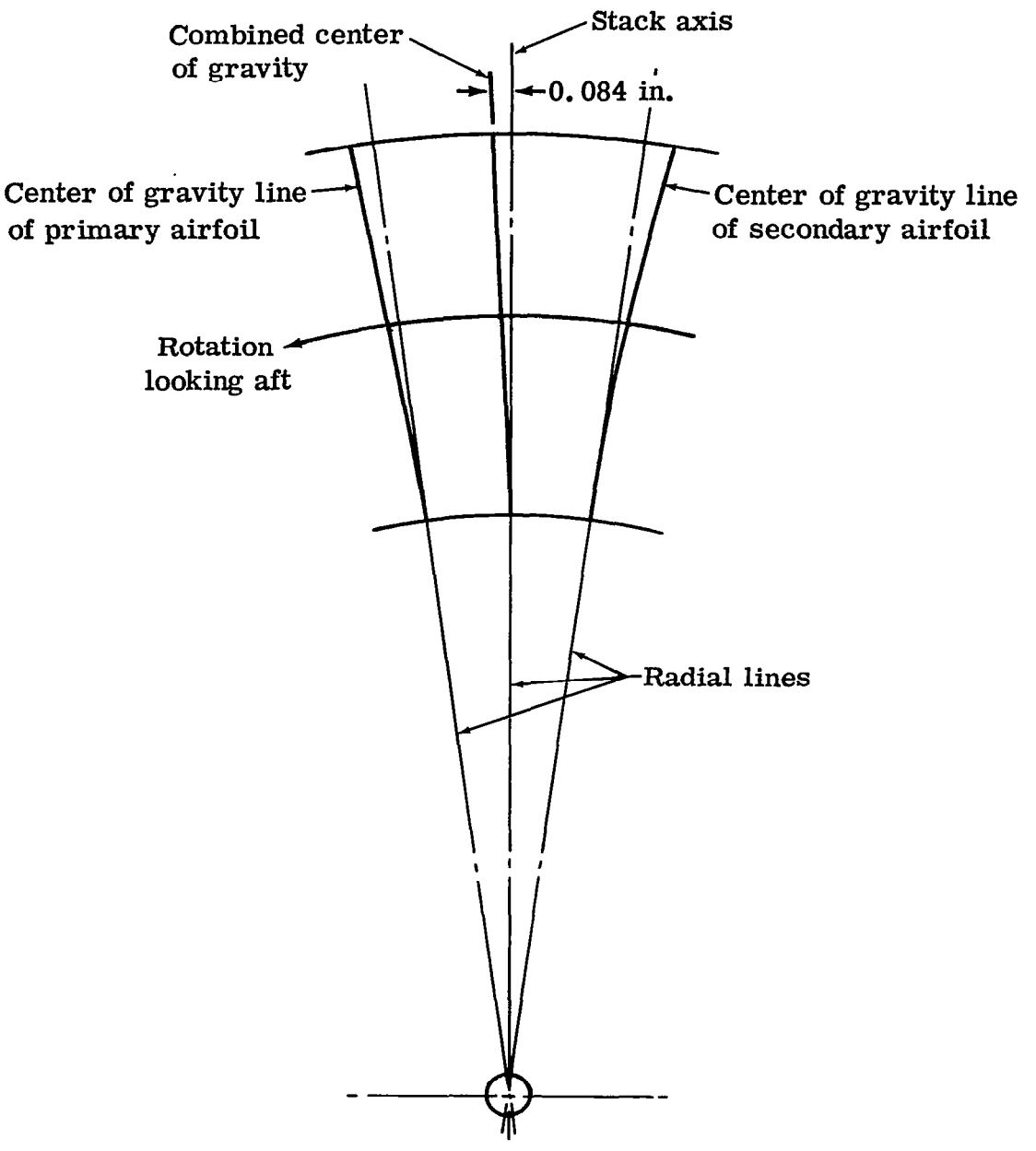

Figure 66. Schematic of tandem rotor-blade stacking arrangement.

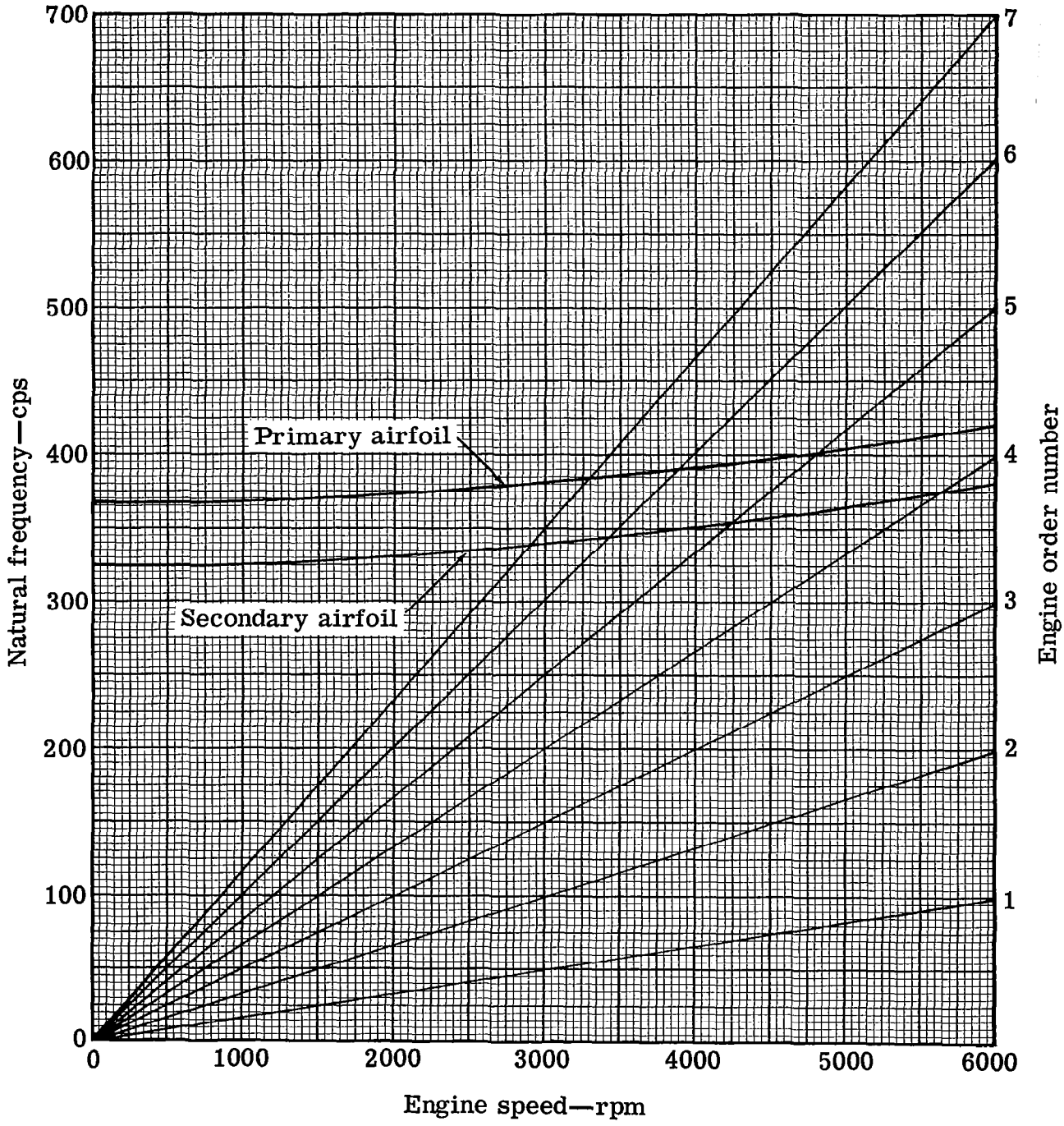

Figure 67. Tandem rotor-blade natural frequency characteristics.

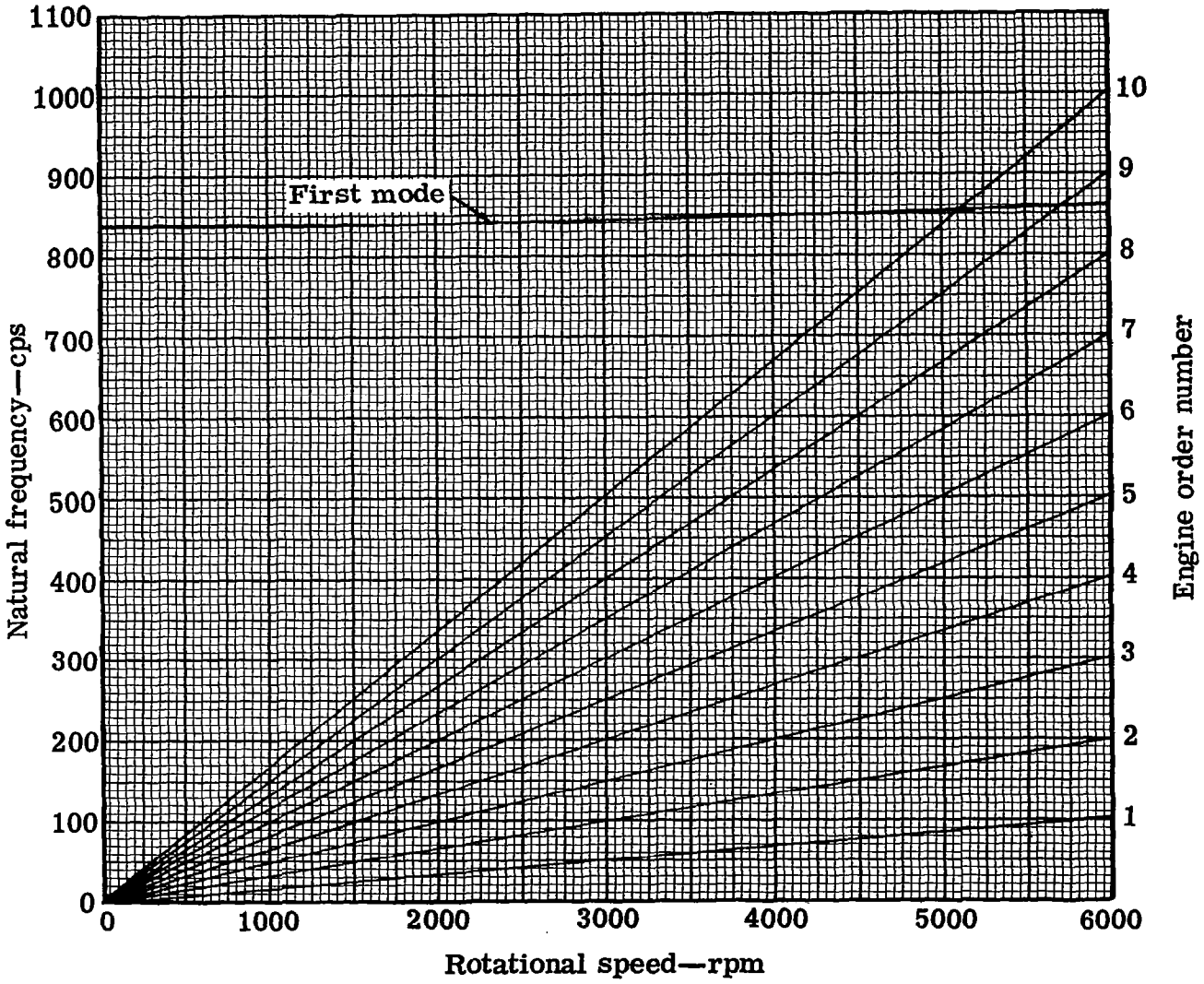

Figure 68. Jet-flap rotor-blade natural frequency characteristics.

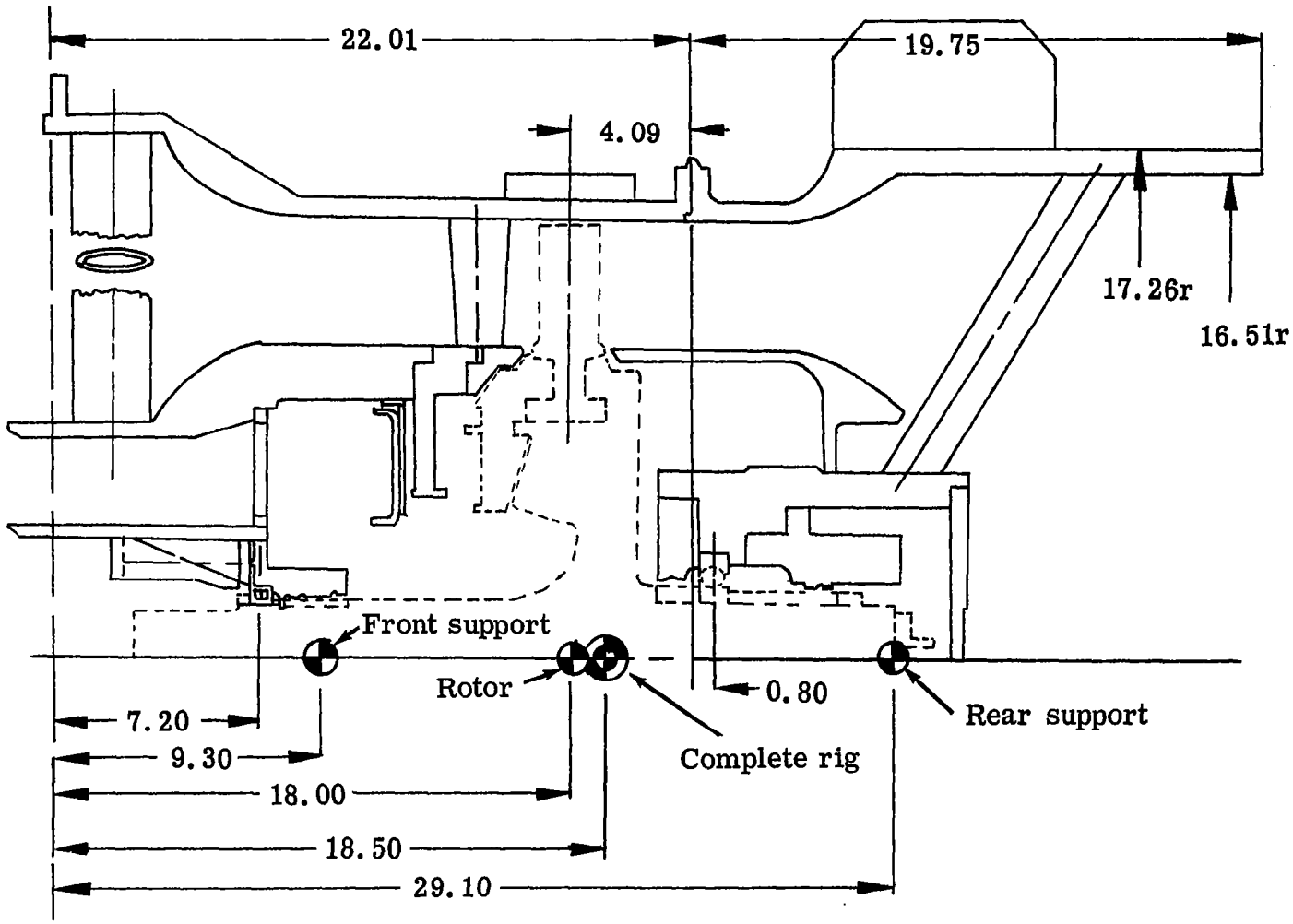

Figure 69. Location of turbine rig centers of gravity.

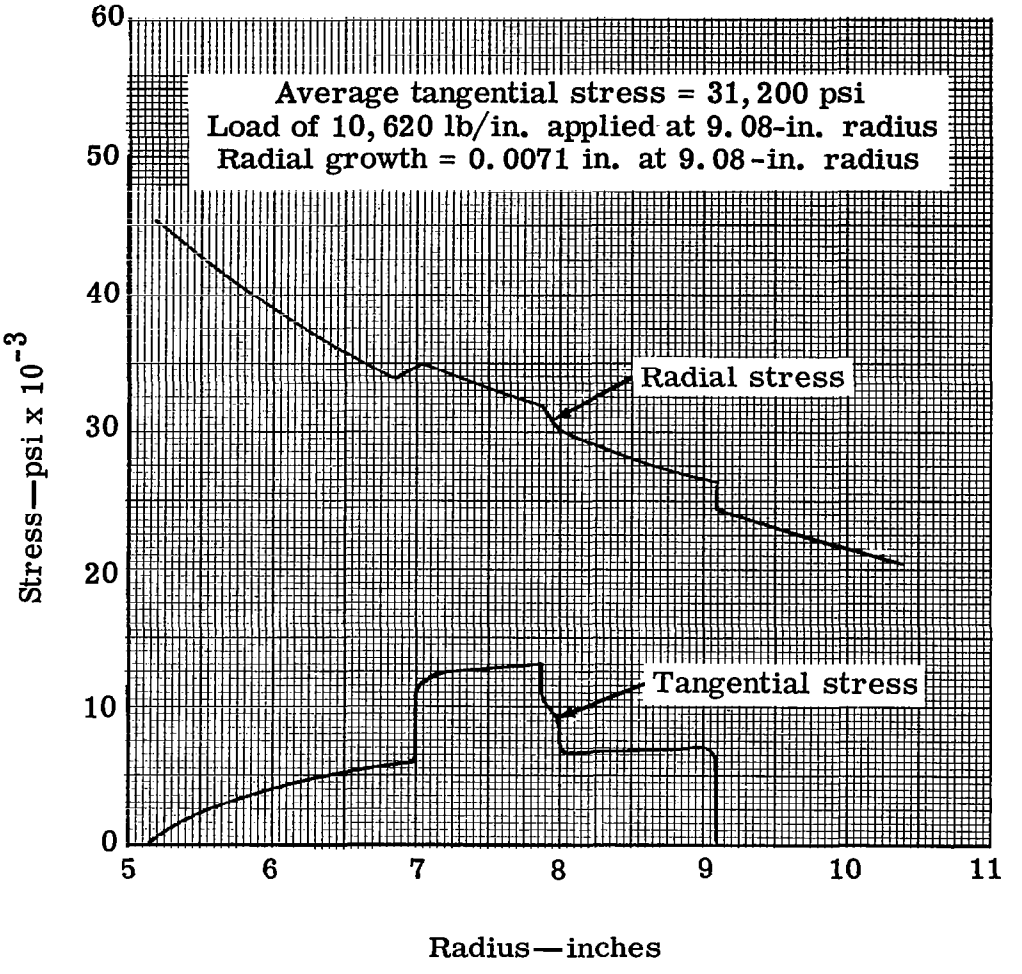

Figure 70. Radial variation in tangential and radial stress in blade retaining ring of design speed.

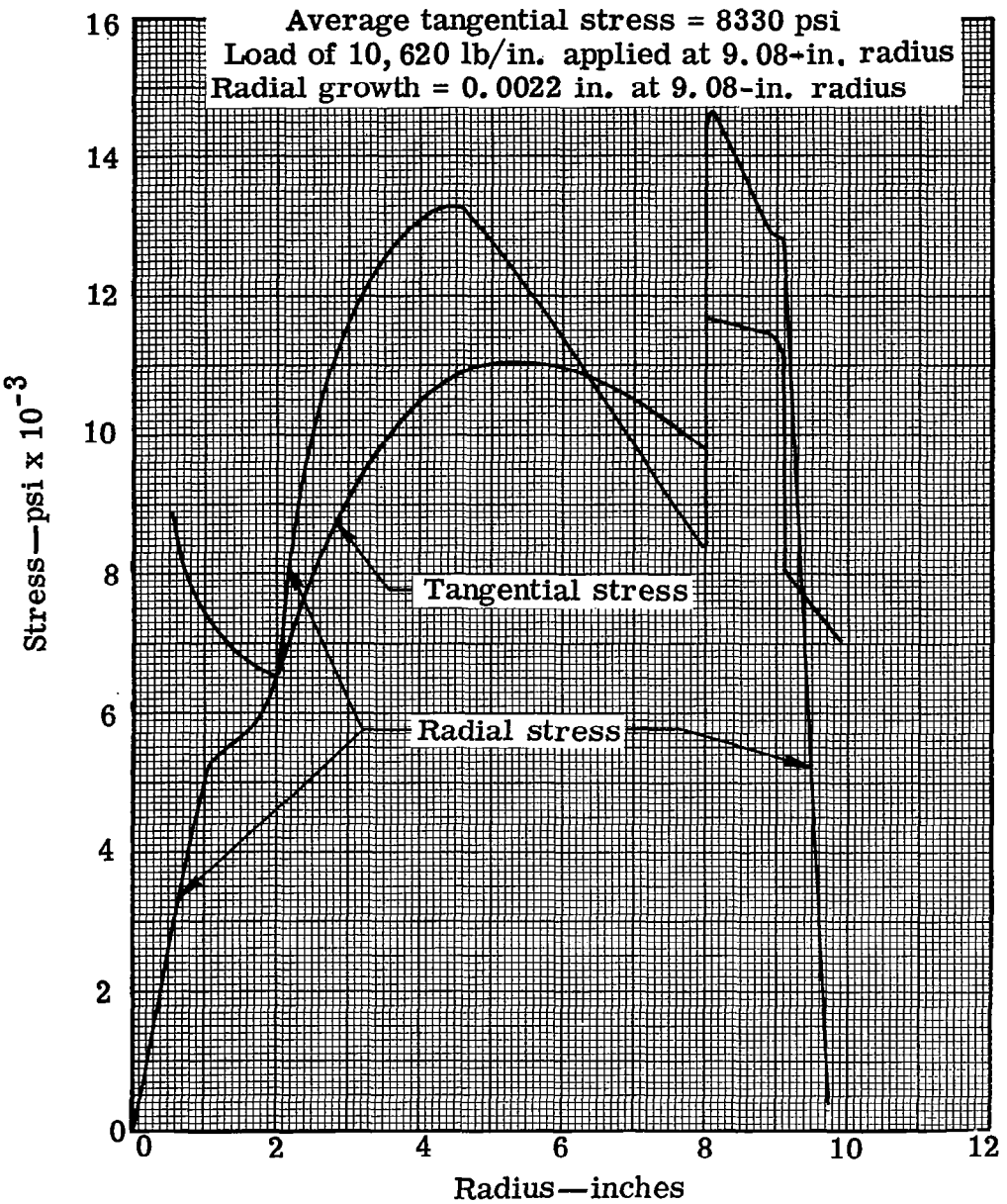

Figure 71. Radial variation of tangential and radial stress in wheel at design spee

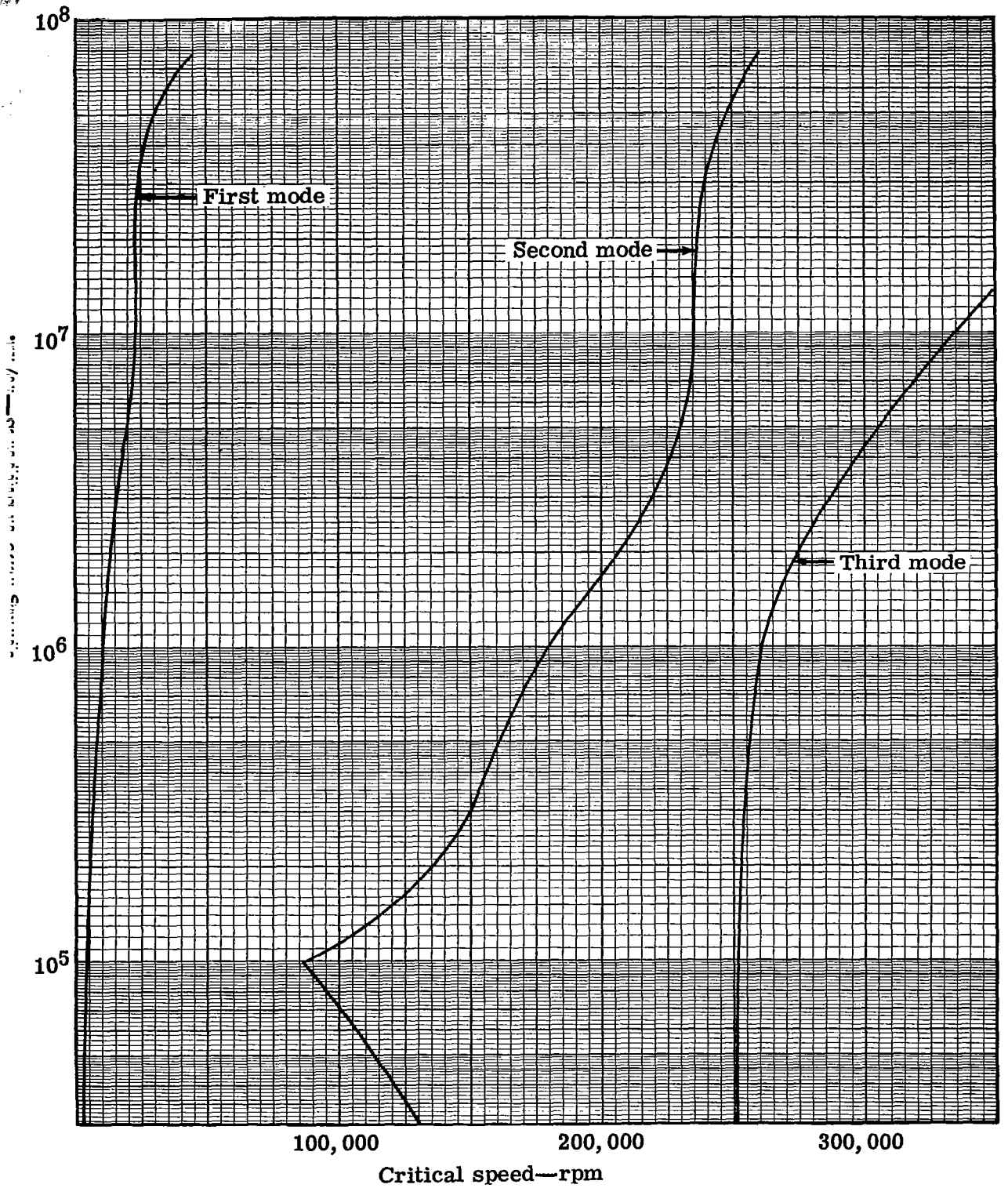

Figure 72. Rotor-assembly critical frequency characteristics.

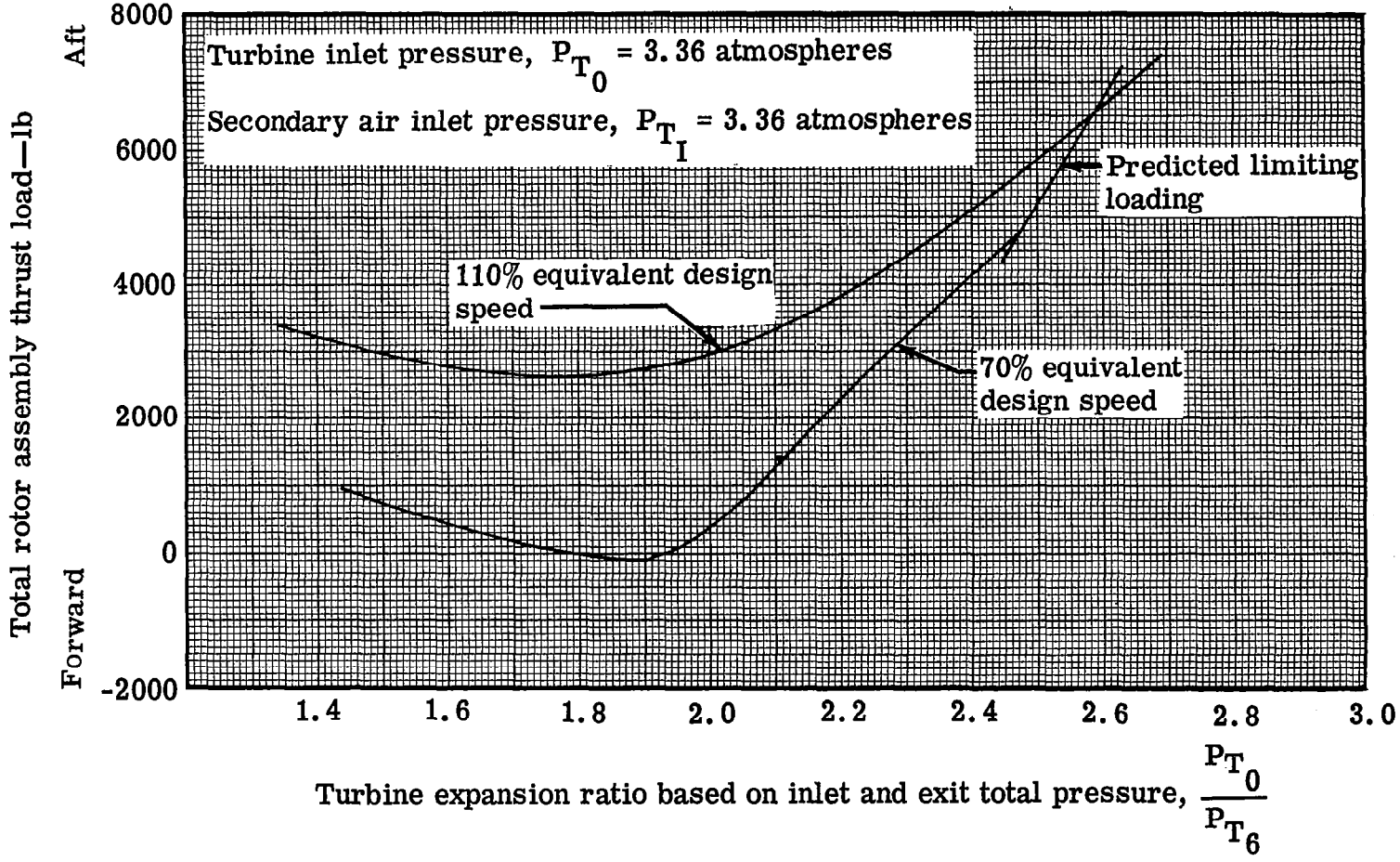

Figure 73. Rotor assembly thrust loads with secondary air pressure equal to turbine inlet pressure.

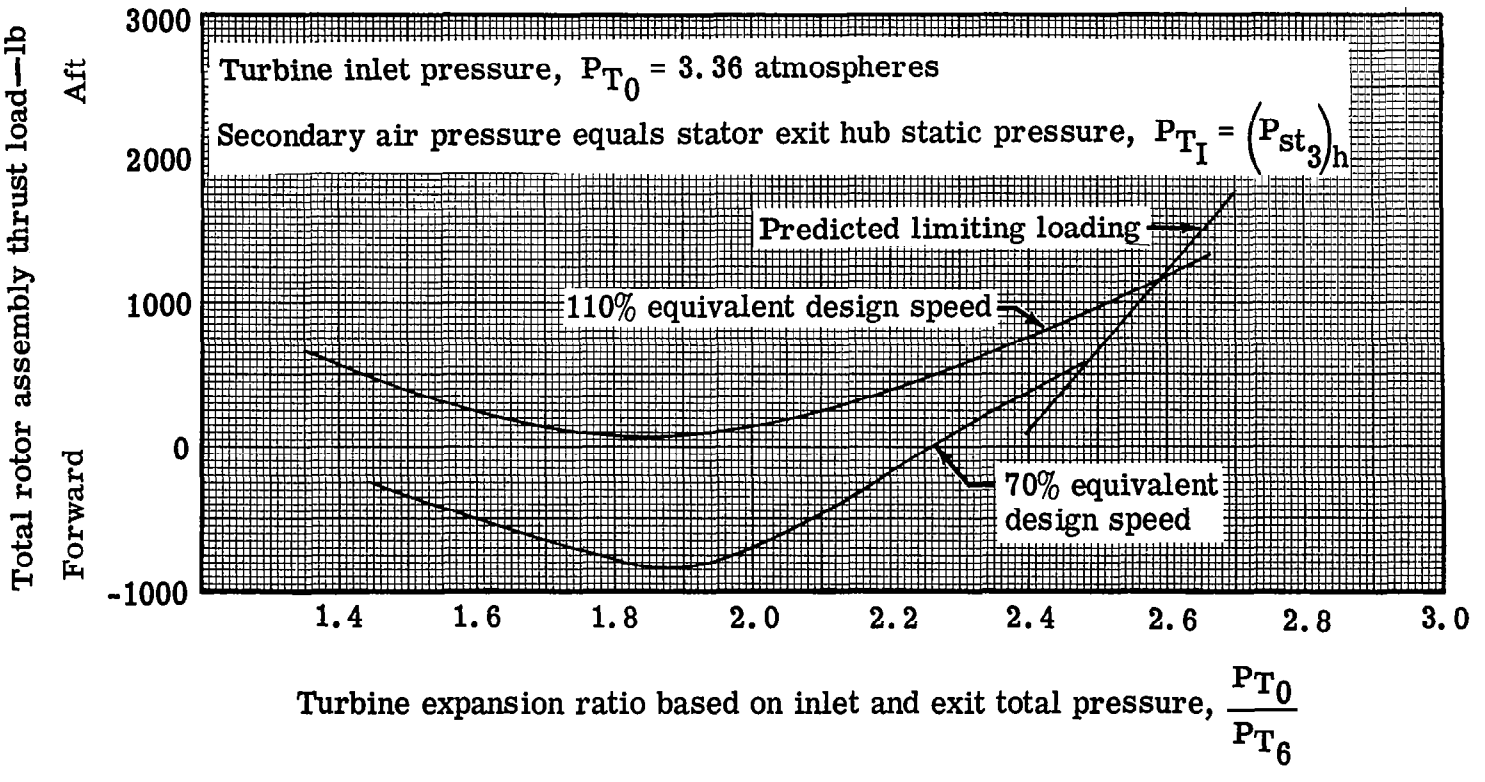

Figure 74. Rotor assembly thrust load characteristics with secondary air pressure equal to predicted rotor hub static pressure.

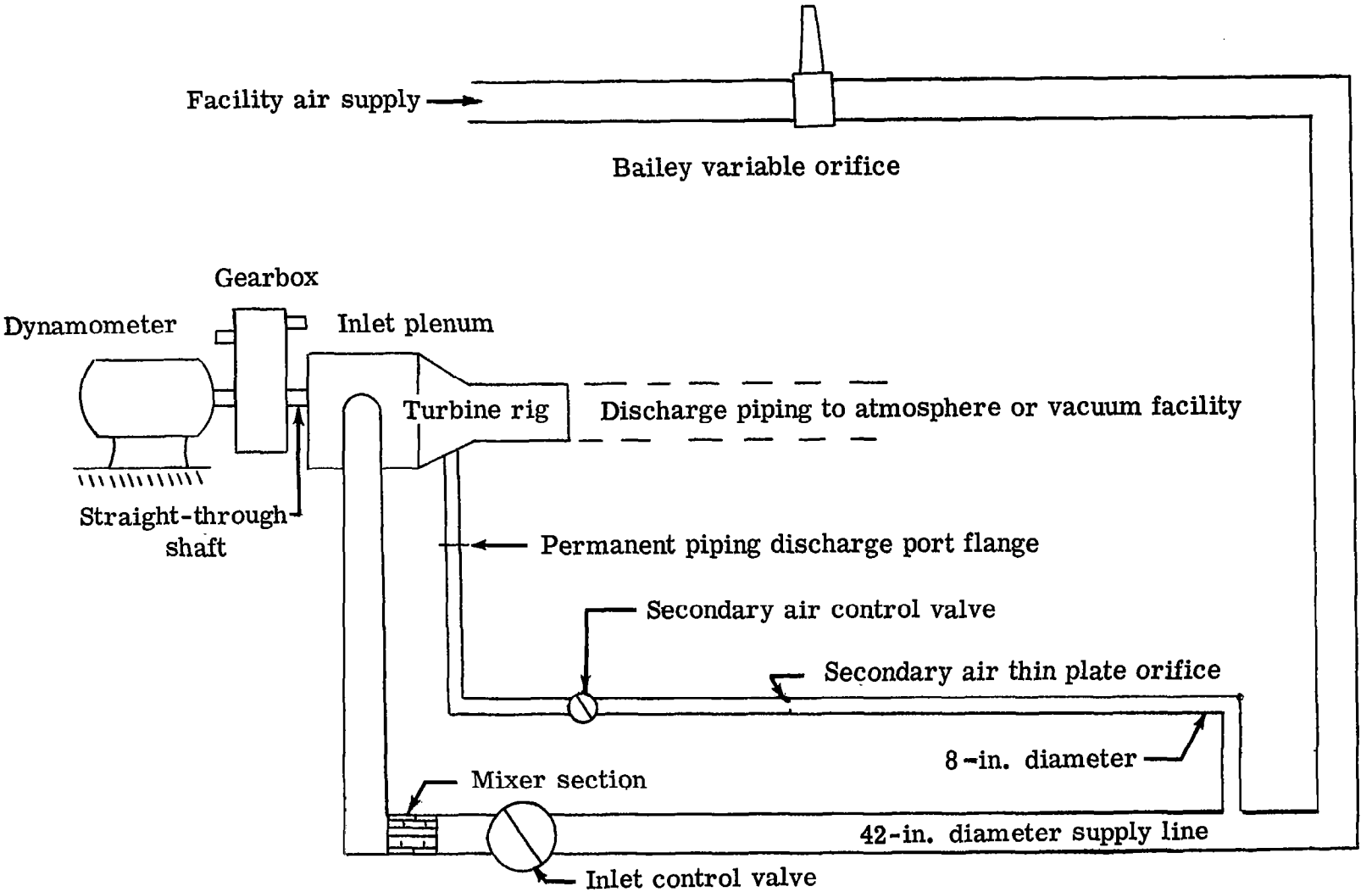

Figure 75. Schematic of test stand air supply system.

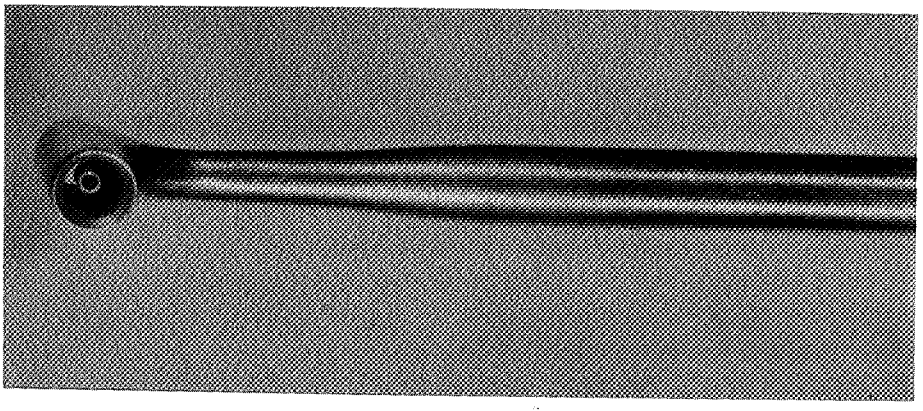

Figure 76. Primary flow inlet total pressure probe.

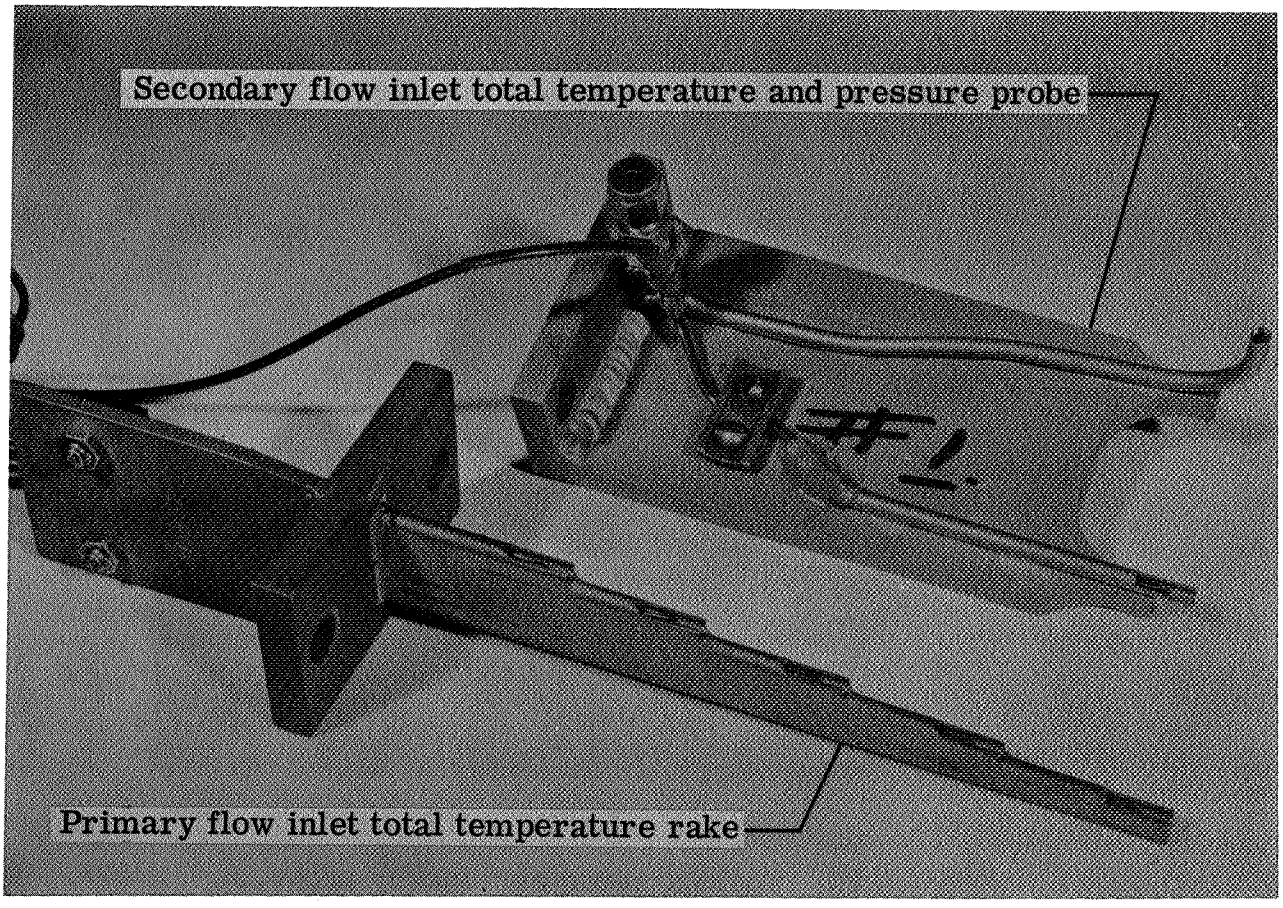

Figure 77. Primary flow inlet total temperature rake and secondary flow inlet total temperature and pressure probe.

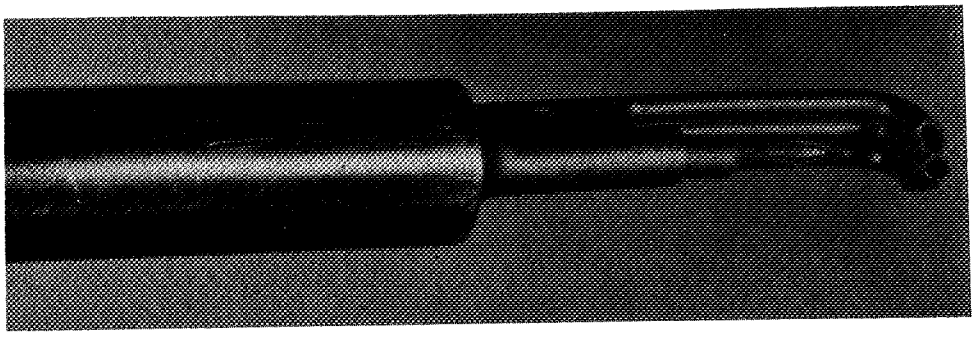

Figure 78. Turbine exit downstream combination total temperature, total pressure, and yaw angle probe.

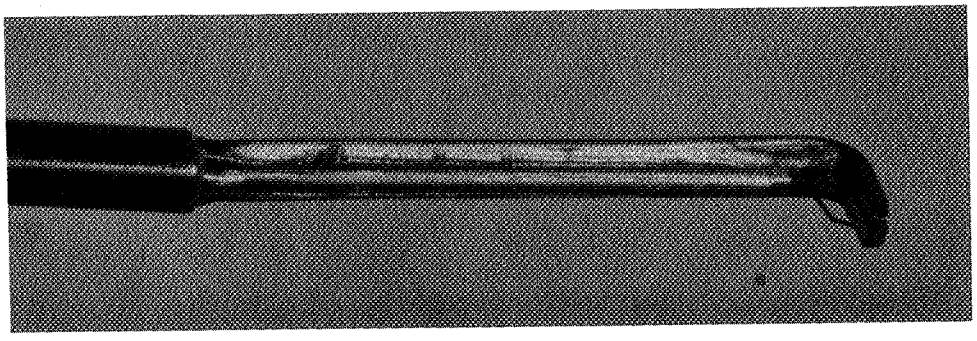

Figure 79. Turbine rotor exit survey probe.

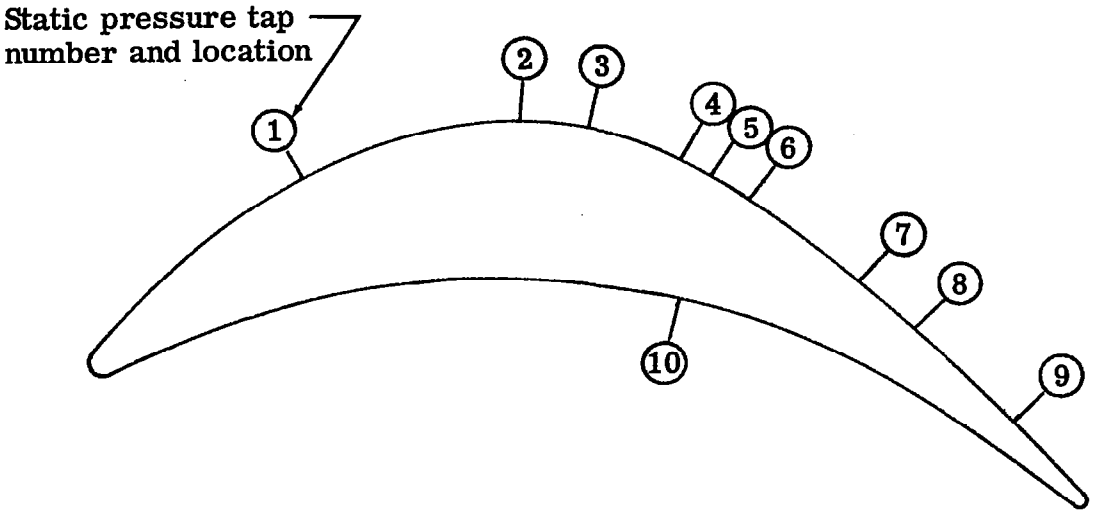

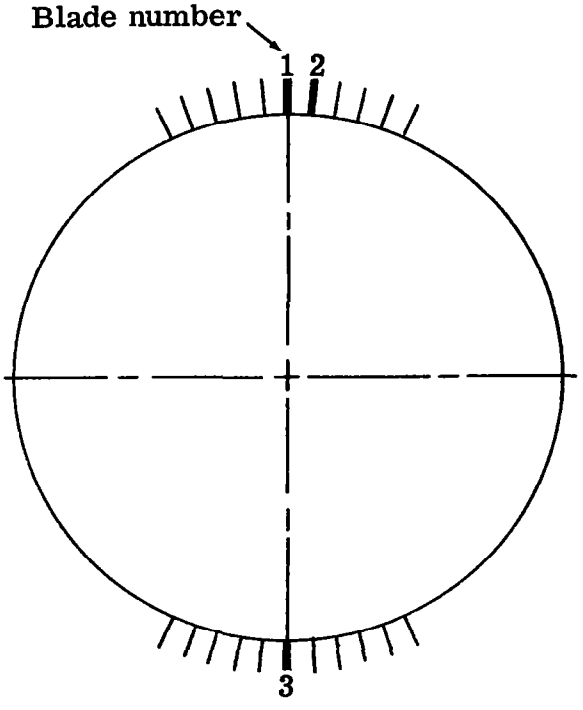

Blade number	Associated pressure tap number	Axial coordinate of tap
1	1	0.465
	2	0.950
	3	1.100
2	10	1.300
	8	1.810
	9	2.030
3	4	1.300
	5	1.370
	6	1.450
	7	1.692

Figure 80. Plain rotor-blade static pressure tap distribution and circumferential location.

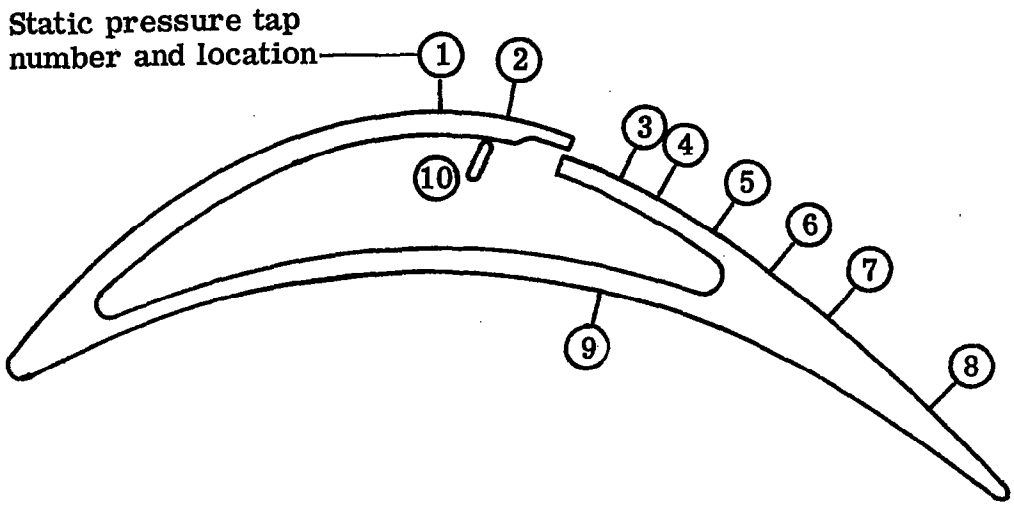

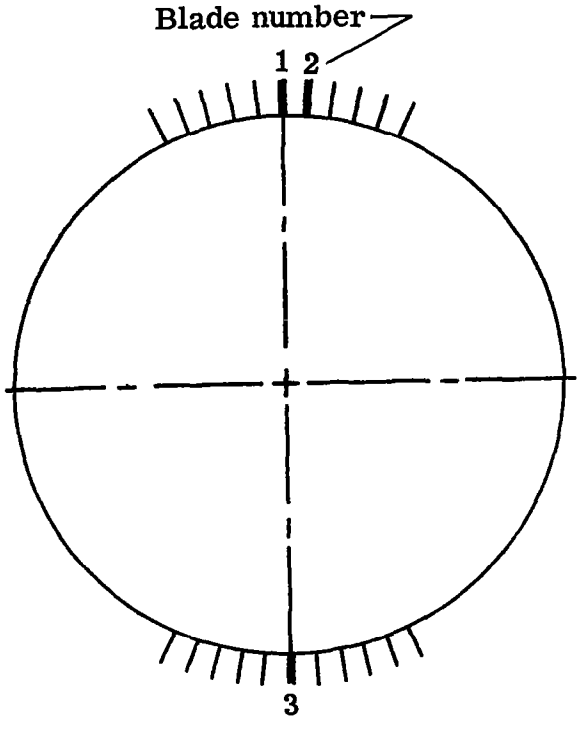

Blade number	Associated pressure tap number	Axial coordinate of tap
1	1 2 10	0.950 1.100 Internal
2	3 4 5	1.350 1.430 1.558
3	6 7 8 9	1.677 1.800 2.025 1.300

Figure 81. Tangential blowing rotor-blade static pressure tap distribution and circumferential location.

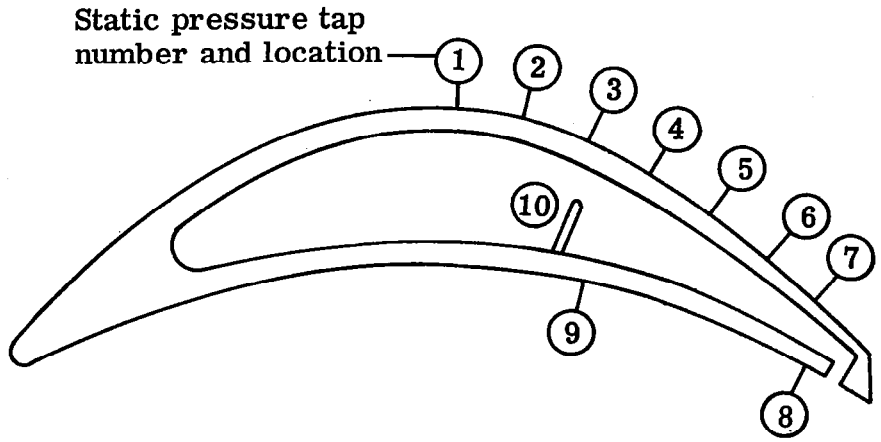

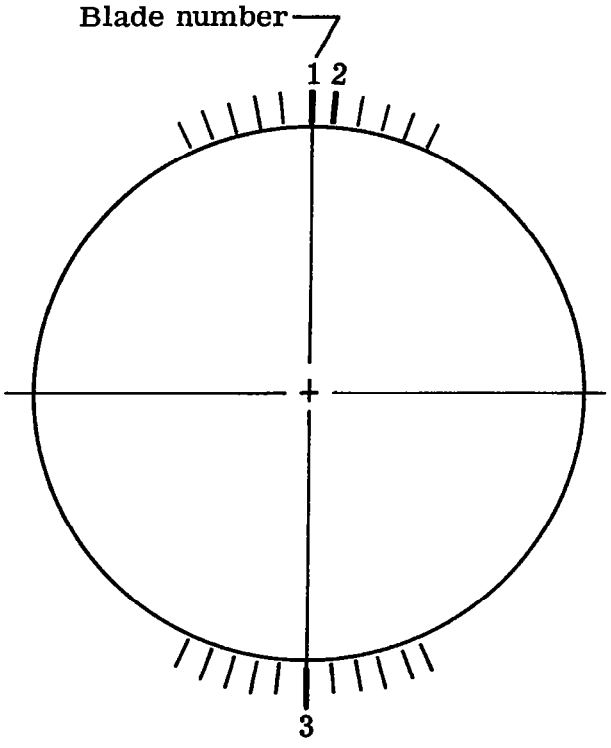

Blade number	Associated pressure tap number	Axial coordinate of tap
1	1 2 3	0.980 1.129 1.270
2	9 8 10	1.267 1.750 Internal
3	4 5 6 7	1.407 1.540 1.660 1.770

Figure 82. Jet-flap rotor-blade static pressure tap distribution and circumferential location.

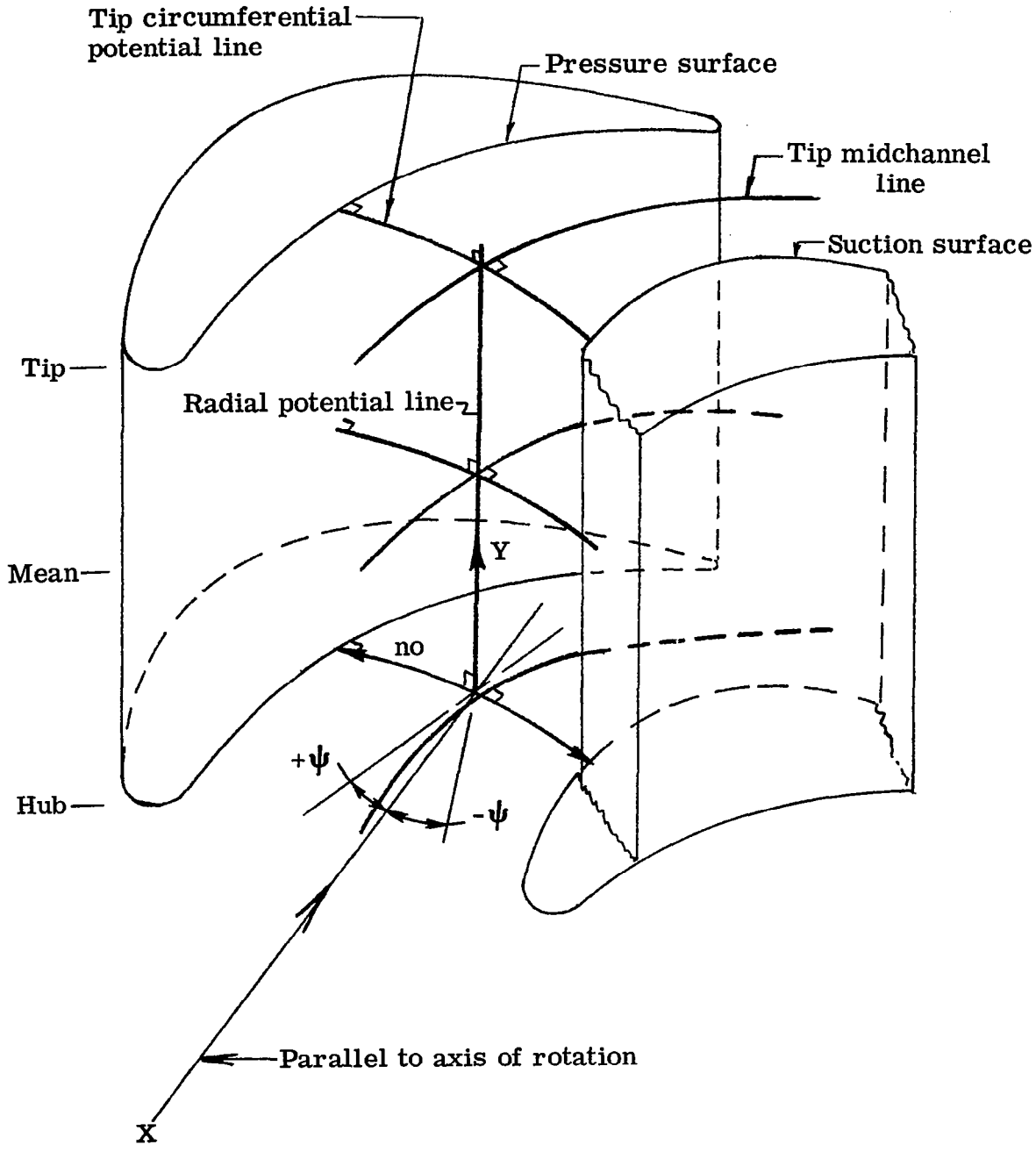

Figure 83. Schematic of flow analysis model.

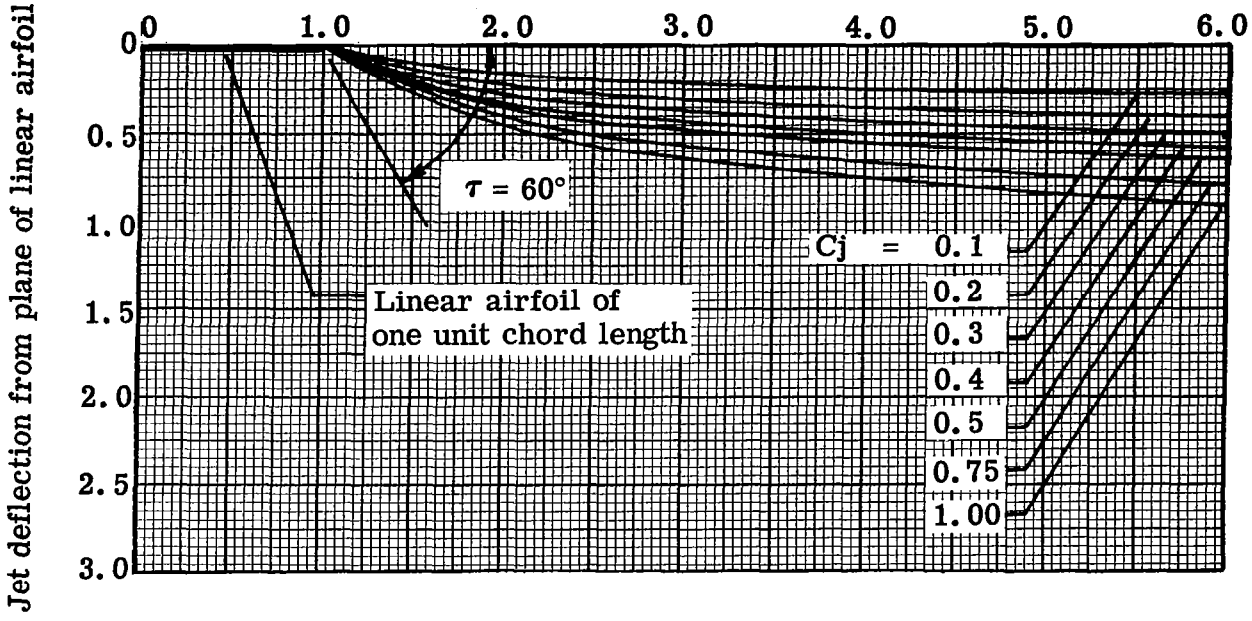

Figure 84. Jet-flap contours for efflux angle of 60° and various jet momentum coefficients.